Study on the Variability and Irregularity of the ENSO-like Behavior of the Pacific with Coupled General Circulation Models

A Dissertation Submitted to
the Graduate School of Life and Environmental Sciences,
the University of Tsukuba
in Partial Fulfillment of the Requirements
for the Degree of Doctor of Philosophy in Science

Seiji YUKIMOTO

Abstract

This dissertation describes interannual and interdecadal variabilities in the Pacific, which are simulated with two versions of the global coupled ocean-atmosphere general circulation model (CGCM) developed at Meteorological Research Institute, along with validations for the models.

The first version of the CGCM (MRI-CGCM1) simulates natural climate variability in the Pacific Ocean, which reveals features in various aspects similar to the observation. The simulated interannual variability in the tropical Pacific exhibits several typical characteristics shared with the observed El Niño and Southern Oscillation (ENSO). For the simulated ENSO, a basin-scale feature of the principal sea surface temperature (SST) variation shows negative correlation between the central North Pacific and the tropical Pacific, as in the observed ENSO. Associated variation of the model atmosphere indicates an intensification of the Aleutian Low and a PNA-like teleconnection pattern as a response to the tropical warm SST anomaly. The ENSO time scale variability in the midlatitude ocean consists of the westward propagation of the subsurface temperature signal and the temperature variation within the shallow mixed layer forced by the anomalous atmospheric heat fluxes.

Spatial and temporal structures of variability in the Pacific Ocean are investigated using a set of two experiments with the MRI-CGCM1. The standard experiment with dynamical ocean shows basin-wide spatial pattern of the principal SST variability similar to the observed one. Both interdecadal and interannual temporal structures of the SST variability agree well between the observation and the model. On the other hand, a slab ocean coupled to the same atmospheric model fails simulating the observed temporal structure. It is suggested, therefore, that the timescale of the coupled variability is associated with dynamical processes in the ocean.

A distinct interdecadal mode of the coupled atmosphere-upper ocean temperature variability is found in the standard experiment of the MRI-CGCM1, with spatio-temporal structure coherent to the SST variability. The mode accompanies an ENSO-like spatial pattern of SST and surface wind, and behaves like a delayed oscillator in ENSO. A wedge shaped anomaly pattern of the upper thermocline temperature is formed in the eastern Pacific, and its northern subtropical signal propagates westward with getting enhanced by a subtropical wind forcing at the central basin. Arrival of the subtropical signal at the western Pacific around 20°N switches anomaly of subsurface temperature in the equatorial region through

anomalous oceanic heat transport along the western boundary. Travel time of the trans-Pacific signal in the subtropics appears to be responsible for the timescale of this mode. The MRI-CGCM1 successfully simulated the second mode of SST with a major variation in the midlatitude North Pacific as in the observed SST. In the upper ocean heat content, we found another distinct mode, which is characterized by a midlatitude-subtropics dipole pattern rotating clockwise around the North Pacific subtropical gyre. However, the associated SST variation of this mode shows a poor correspondence in the dominant interdecadal modes for the observed SST.

The second version of the CGCM (MRI-CGCM2) is developed aiming at improving the defects in the MRI-CGCM1 and achieving higher accuracy and reliability. As a result of the development, the model is capable of making a stable integration longer than 400 years with realistic mean climate and variabilities.

The MRI-CGCM2 produces ENSO with peak SST anomalies ranging from –2.5°C to +4°C in the equatorial central-eastern Pacific. In the equatorial Pacific, the temporal phase relationship of the upper ocean heat content (OHC) anomaly relative to the SST, and wind stress anomalies can be explained by the “recharge oscillator” mechanism. A difference of the zonal mean OHC anomaly between the equator and the northern subtropics arises before the development of an equatorial SST anomaly. The model also reveals realistic irregularities of ENSO in amplitude, periodicity, and seasonal phase locking. It is implied that a larger ocean heat content anomaly is accumulated on the equator as a precursor of a stronger El Niño. The heat-budget analysis suggests that horizontal advection in the ocean interior is a major contributor to the build-up of the larger OHC anomaly during the recharge phase, which is associated with the zonal-mean wind-*curl* anomaly in the off-equatorial North Pacific. This also implies that the surface heating in the subtropics is a potential contributor through meridional heat transport. Besides the aspect of amplitude irregularity, the model El Niño shows irregularities in frequency and seasonal phase locking. Possible linkages between these irregularities are discussed.

Contents

List of Figures

List of Tables

1 Introduction

The observed variability in the Pacific Ocean has been studied from various aspects. In the tropical Pacific, El Niño and Southern Oscillation (ENSO) is one of the most dominant interannual natural variabilities of the air-sea coupled system, which has been intensively and extensively studied since Bjerknes (1969) proposed that the oceanographic phenomenon El Nino and the atmospheric phenomenon Southern Oscillation are the interannual variation with a linkage between them. The influence of ENSO to the midlatitude also captured great concern in many observational and GCM investigations.

1.1 Decadal to Interdecadal variability in the Pacific

In the midlatitude Pacific, it has been known that there are some decadal to interdecadal variabilities, since the marked climate shift was found in mid-1970's in the North Pacific (Venrick et al. 1987, Kashiwabara 1987, Nitta and Yamada 1989, Trenberth 1990). Nitta and Yamada (1989) suggested the linkage between the interdecadal sea surface temperature (SST) shift in the North Pacific and the tropical Pacific SST through an atmospheric teleconnection. A number of subsequent studies also noted the relationship in the interdecadal shift between the tropical and extratropical Pacific (Trenberth, 1990; Graham, 1994; Trenberth and Hurrell, 1994). Atmospheric general circulation models (GCMs) forced by the tropical SST variation successfully reproduced observed change in the midlatitude atmospheric circulation associated with the interdecadal SST shift in the North Pacific (Graham, 1994; Lau and Nath, 1994). It appears that the interdecadal variability in the tropical SST can explain the midlatitude atmosphere variability that affects the interdecadal SST variability in the North Pacific. Based on simulations with an ocean model forced by the observed surface heat flux, wind stress and mixing, Miller et al. (1994) suggested that the shift in the North Pacific Ocean is qualitatively explained by the changes in the atmospheric forcing, but feedback effects of the midlatitude SST to the midlatitude atmosphere should be considered for quantitative explanation.

Nitta and Yamada (1989) noted that the interdecadal shift of SST accompanies a basin-wide pattern similar to the first mode of the empirical orthogonal function (EOF) for unfiltered global SST (with a 38-year length record). Zhang et al. (1997) suggested that the interdecadal variability in the Pacific SST, from which ENSO related component was removed, has a spatial pattern similar to the ENSO-related pattern. Zhang et al. (1997) also examined the ENSO-like variability based on a centennial record of the SST observation, and found that SST shifts in the Pacific Ocean with similar pattern to that in mid-1970s

have been repeated in the past. Yukimoto et al. (1996) showed similarity between the spatial structures of dominant variabilities in ENSO timescale and decadal timescale, based on a simulation with their coupled GCM.

All these studies seem to indicate that an interdecadal oscillatory mechanism with the ENSO-like SST pattern (which implies a linkage between the tropics and the extratropics) is possible, however the cause of the interdecadal variability in the tropical Pacific have yet to be explained. A possible mechanism for interdecadal variability in the tropical Pacific is proposed by Gu and Philander (1997), based on the argument that anomalous ocean temperatures in the midlatitude, as a result of response to the tropical SST, change the thermocline property in the tropics through an oceanic advection. They demonstrated that the oceanic advection is attributed to a shallow wind-driven meridional circulation, which involves the subduction in the eastern regions of the subtropical gyre, and timescale of the variability primarily depends on the delay time with the advection from the subduction region to the equatorial upwelling region. Observations of decadal temperature anomalies that subducted from midlatitude surface into subtropical subsurface in the North Pacific are reported by Deser et al. (1996) and Schneider et al. (1998). However, Schneider et al. (1998) claimed that the subductions have no significant coupling to the decadal tropical variations.

Knutson and Manabe (1998) (hereafter referred to as KM98) suggested another plausible mechanism that links extratropical variation and equatorial variation based on the analysis of their CGCM simulation. Their leading mode for decadal timescale shows a triangular SST pattern and evolution of tropical winds and oceanic heat content, which share several features with ENSO but have broader meridional extent. They found westward propagation of the heat content anomaly in the far off-equator (~12°N), and claimed delayed oscillator mechanism similar to that in ENSO (Schopf and Suarez, 1988) can act in decadal timescale as well. However, they did not show how the far off-equatorial heat content anomaly is caused and how the propagated signal of far off-equator can affect the equatorial subsurface temperature variation.

On the other hand, it is known from the analysis of the observed SST (Kawamura, 1994; Deser and Blackmon, 1995), that there is another decadal SST variability confined in the midlatitude North Pacific. It is characterized with a zonally elongated elliptic pattern around the Kuroshio Extension region and with no (or very weak) signal in the tropical Pacific. Trenberth and Hurrell (1994) suggested importance of feedback mechanism that north-south shifts of storm track accompanied by the SST change in the central North Pacific reinforce or sustain the SST anomaly there. Latif and Barnett (1994, 1996) simulated oscillatory interdecadal variation in the North Pacific with a CGCM, and

explained it as an instability involving a positive feedback in the midlatitude ocean-atmosphere and a delayed negative feedback associated with dynamical spin-up (spin-down) of the subtropical ocean gyre. With a linearized coupled model, Jin (1997) showed that oscillatory coupled interdecadal modes can be interpreted as a delayed oscillator involving air-sea thermodynamical feedback and delayed feedback with a dynamic adjustment of ocean gyre circulation through baroclinic Rossby waves under wind forcing.

Summarizing for the arguments mentioned above, possible mechanisms for interdecadal variability in the Pacific are categorized roughly into two major concepts; 1) an atmosphere-ocean coupled variability with linkage between the tropics and the extratropics, and 2) atmosphere-ocean coupled variability primarily in the extratropics. Both concepts involve feedback processes acting between the atmosphere and the ocean, and mechanisms similar to the delayed oscillator theory providing timescales of the variability. The interdecadal variability in the Pacific may not be necessarily explained by a single mechanism. We explore whether proposed mechanisms as mentioned above can be applied to the variabilities in our model.

1.2 Irregularity of ENSO

Beside the decadal to interdecadal variability, there remains a major subject for the variabilities in the Pacific. The irregularity of El Niño and Southern Oscillation (ENSO) is currently a major issue in the ENSO theory (Neelin et al. 1998). There are several different aspects of ENSO irregularity. The first aspect is the irregularity of amplitude; the amplitude of the sea surface temperature (SST) anomaly in the equatorial Pacific differs from one event to another. The second aspect is the frequency modulation; the ENSO variability has a rather broad spectral peak from roughly 2 to 7 years in periods. Jiang et al (1995), for instance, found that ENSO variability can be divided into quasi-biennial and quasi-quadrennial periods. The third aspect of the ENSO irregularity is the phase-locking. Although ENSO tends to have its peak at the end of the calendar year, there is an interdecadal change of the seasonal phase-locking (Mitchell and Wallace 1996), or event-wise scattered phase locking (Neelin et al. 2000). Furthermore, the predictability of ENSO also exhibits decadal variability (Kirtman and Schopf 1998).

The origin of the observed ENSO irregularity has remained open to argument, and has been a matter of controversy among many researchers. There are three distinct hypotheses for the origin of ENSO irregularity. The first one is deterministic chaos associated with the nonlinear dynamics of ENSO (Munnich et al. 1991; Jin et al. 1994; Tziperman et al. 1994; Chang et al. 1994; Tzipernam et al. 1995), the second is stochastic

"weather noise" forcing (Kleeman and Power 1994; Chang et al. 1996; Flügel and Chang 1996; Blanke et al. 1997), and the third is decadal changes in the climatological background state (Kirtman and Schopf 1998; Fedorov and Philander 2000; An and Wang 2000). Recent studies suggest that the observed irregularity may be induced by combinations of the above causes, with the degree of contribution possibly varying with time. There is also a question as to whether or not there are any links between the different aspects of the irregularities mentioned above.

The 1997/98 El Niño was the strongest event in the twentieth century, and it occurred under the intensive, and extensive observation of buoys and satellite measurements, such as the TAO array and TOPEX/Poseidon. Even so, the reason why it was so strong has not been sufficiently answered.

For the ENSO dynamics, Jin (1997) proposed the “recharge oscillator” paradigm, in which oscillations are caused by recharge-discharge of the zonal-mean equatorial ocean heat content through the oceanic adjustment not only with the equatorial ocean waves, but also with the midlatitude Rossby waves. Extending the concept of this recharge oscillator theory, the strength of El Niño may be associated with its recharge stage in the mechanism. Meinen and McPhaden (2000) showed that the zonal mean warm water volume anomalies in the equatorial Pacific precede the SST anomalies by about seven months, based on subsurface ocean temperature data since 1980. They suggested that the magnitude of the SST anomalies is directly related to the magnitude of the warm water volume anomalies, hence heat content anomalies in the equatorial Pacific. For the build-up of the equatorial heat content anomaly, Li (1997) noted the importance of wind stress *curl* anomaly at the off-equator (though the subtropics), that is related to the atmospheric Hadley circulation. It is thought that influences of atmosphere-ocean coupling and/or “weather noise” forcing in the subtropics through midlatitudes might be an essential factor for the preconditioning of the strong El Niño.

In past studies on the mechanism of ENSO irregularity, simple coupled models, such as the “delayed oscillator” (Schopf and Suarez 1988; Battisti and Hirst 1989), the recharge oscillator (Jin 1997), and “reduced physics” models (Neelin et al. 1998), such as the Cane-Zebiak type coupled model (Cane and Zebiak 1985) were used rather than full physics GCMs. Those models were useful for investigating the dependence on parameters in the ENSO system. In those simplified models that commonly excluded the extratropics, the influence from the subtropics and midlatitude variability is treated as an uncorrelated stochastic forcing. However, there are many kinds of atmospheric variabilities outside the equatorial Pacific, (for instance, the interannual variation of the Asian monsoon) that possibly interact with ENSO, and that can be simulated by CGCMs. Recently, simulated

ENSO in full CGCMs has become sufficiently realistic in its temporal and spatial structure, and has been analyzed from the aspect of the recharge oscillator paradigm and shown to be consistent with it (e.g. Collins 2000; Yu and Mechoso 2001). We believe we will be able to get useful information about the irregularity of ENSO by analyzing realistic model ENSOs in such CGCMs.

Only the two extremely strong events in the Pacific in 1982/83 and 1997/98 happened under observation, with sufficient measurements of both the atmosphere and the subsurface ocean. Obviously, it is difficult to evaluate the differences of merely observed events with any statistical significance. Studying simulated ENSO in a multi-century integration of CGCMs, however, will lead to a better understanding of the relationships between the precursors and the magnitude of SST anomalies in the following event with a statistical confidence.

1.3 Ojectives

The mechanisms of the decadal to interdecadal variabilities or the ENSO irregularity have not yet fully explained in the past studies, partly because the observational data are not sufficient for studying such subjects, which requires extensive and long-term observation particularly in the ocean. With developing CGCMs which are capable of realistically reproducing the observed climate and its variability, analyzing results from their long-term simulations are quite useful for solving those questions. Furthermore, those analyses also contribute to improving the model's performance of reproducing the climate and variability.

Along with increasing concern to global warming due to anthropogenic greenhouse gases, it has been recognized that comprehension of natural variability of the climate system is the most essential for quantitative detection of the warming and for reduction of uncertainties in the prediction of future climate. Increasing number of experiments with coupled atmosphere-ocean GCMs have been conducted in order to investigate transient responses of climate system to the growth of atmospheric greenhouse gases (IPCC 1995, 2001). It is pointed out that quantitative detection of greenhouse effect is difficult due to the existence of natural variability of interdecadal time scale with comparable amplitude (IPCC 1990, IPCC 1995, IPCC 2001). It is required, therefore, that the models have performance to reproduce realistically natural variability for the climate sensitivity experiments.

At the Meteorological Research Institute (MRI), an experiment of global warming with transient CO_2 increase was performed (Tokioka et al. 1995) with the first version of the CGCM at MRI (MRI-CGCM1). In several transient experiments in the past, though interdecadal natural variabilities were simulated in their coupled models (Manabe et al.,

1991, Cubash et al., 1992), where resolutions of the ocean models were too low to simulate realistic El Niño. The MRI-CGCM1 has enough resolution in the OGCM in the low latitude to show ENSO-like variation and interdecadal variation in the Pacific both in the control run and CO_2 increase run.

The second version of the CGCM is developed at MRI. The model is aimed at overcoming defects in the MRI-CGCM1, and improving the reproducibility of climate variabilities.

In order to validate the performance of the models, the present paper demonstrates the simulated mean climate in Section 2. In Section 3, the temporal and spatial structures of the simulated variability are presented, then they are compared with the observed variability. The present paper, furthermore, tries to pursue mechanisms of the interdecadal variability in the Pacific with emphasis on its ENSO-like behavior in Section 4.

From the different point of view for the variability in the Pacific, irregularity of ENSO is investigated (Section 5). After verifying the oscillation mechanism for the simulated ENSO in a MRI-CGCM2, we will pursue solving questions about irregularities in the observed ENSO by identifying the simulated precursors for irregular El Niños.

Conclusions and discussion are given in Section 6.

2 Development of Coupled General Circulation Models at MRI

Two versions of the global coupled ocean-atmosphere general circulation model are developed at MRI. The first version has contributed to the projection of climate change (IPCC, 1996) with its experiments of transient response to a greenhouse gas increase (Tokioka et al, 1995). The second version of the CGCM has been developed aiming at making more accurate and reliable projection of the climate change, and the results from the experiments for transient response to more detailed scenario of greenhouse gases and sulfate aerosol contributed to IPCC (2001). In this section, we overview the two models and demonstrate their performance how they reproduce the mean climate.

2.1 MRI-CGCM1

The first version of the global coupled ocean-atmosphere general circulation model is developed at MRI (Tokioka et al, 1996). It consists of a world ocean general circulation model (OGCM) with an active sea-ice model and an atmospheric general circulation model (AGCM).

The atmospheric component of the model is a version of the MRI-AGCM (Tokioka et al. 1984). The horizontal resolution of the AGCM is 4 degrees in latitude and 5 degrees in longitude. There are 15 vertical layers with the model top at 1 *hPa*. Calculation of shortwave radiation is based on Lacis and Hansen (1974). Calculation of longwave radiation is based on the multi-parameter random model by Shibata and Aoki (1989), being applied in four spectral regions (20-550, 550-800, 800-1200, 1200-2200 cm^{-1}), and treats absorption due to H_2O, CO_2 and O_3. Parameterization of penetrative convection is based on the scheme of Arakawa and Schubert (1974). Planetary boundary layer (PBL) is parameterized as a well-mixed layer with variable depth following the model of Randall (1976). Five types of clouds are considered: penetrative cumulus cloud, mid-level convective cloud, stratus cloud in PBL, cloud due to large-scale condensation and cirrus anvil cloud. Partial cloudiness is allowed for the convective clouds. Orographic gravity-wave drag is parameterized following Palmer et al. (1986) with quantitative adjustments by Yagai and Yamazaki (1988). Thermodynamic and hydrological treatment of the land surface are based on a multi-layer soil model which has four layers with the bottom at 10 *m* depth. Effect of the vegetation canopy is not explicitly modeled. In order to allow different horizontal resolutions between the AGCM and the OGCM, mixture of different types of surface characteristics (ocean, land, sea ice and ice sheet) is considered in

a single AGCM grid box. Kitoh et al. (1995) demonstrated the performance of the AGCM in reproducing the climate for 1979 through 1988 with the prescribed SST and sea ice distribution based on the observation. The model shows realistic interannual variations in the midlatitude responding to the tropical SST forcing, as well as the model climatology.

The oceanic component of the model is a world ocean general circulation model, which is developed at MRI based on the Pacific Ocean model (see Nagai et al., 1992). The model has now realistic bottom topography and 2.5° (longitude) × 2.0° (latitude) horizontal resolution, though the former Pacific model had a flat bottom. For latitudes lower than 12 degrees, non-uniform latitudinal grid spacing ranges from 0.5 degrees (4˚S - 4˚N) to 2 degrees (further poleward from 12˚N and 12˚S). There are 21 vertical levels, 11 of which are located in the upper 300 *m* depth. To resolve the oceanic mixed layer, a turbulence closure scheme based on Mellor-Yamada level-2 is introduced. Coefficients of the horizontal viscosity and diffusivity are set to 2.0×10^{9} cm^2s^{-1} and 5.0×10^{7} cm^2s^{-1}, respectively. The vertical eddy viscosity and diffusivity are calculated following the turbulence closure scheme (Mellor and Yamada, 1974, 1982 and Mellor and Durbin, 1975).

An active sea ice is modeled. The model predicts compactness (fractional coverage in a grid) and thickness of sea ice following Mellor and Kantha (1989). Advection of sea ice is taken into considerations with a simple relation to the ocean surface current.

Before coupling with the OGCM, the AGCM was integrated for 3 years, forced by the observed SST. The OGCM was spun up for 1500 years from an initial state with motionless and homogeneous potential temperature and salinity. Then, preliminary coupling 30-year-integration was made, during which flux adjustments of heat and freshwater were obtained through the relaxation of sea surface temperature and salinity to Levitus (1982) climatology. Finally, 150 years integration was made as a control run. During this integration, the flux adjustments obtained above were imposed to insure realistic climate of SST and surface salinity. The model results analyzed for illustrating the model climate covers a 70-years control run as the counter part of the transient CO_2 experiment. Its atmospheric CO_2 concentration is fixed at the present level of 345 ppm_v.

The model is modified to make simulations for examining equilibrium in response to a forcing (such as doubled CO_2 concentration) by replacing the oceanic component by an ocean mixed layer model with 50 m slab. This type of model is referred to as SGCM, and the SGCM for the MRI-CGCM1 is referred to as MRI-SGCM1 hereafter for convenience. The SGCM enables us to make experiments without ocean dynamics, which allows us to quantify the effects of ocean dynamics in the climate variability by comparing the results with those with full-dynamical CGCM.

2.2 Climatology of the MRI-CGCM1

In order to validate the model performance, the present section overviews the model climatology of the MRI-CGCM1 for the simulated SST, wind stress, and ocean subsurface thermal structure, compared with observational data.

Annual mean SST climatology for 70 years integration of the model is shown in Fig. 2-1. Flux adjustments are effectively working to maintain the SST close to the observed (Levitus, 1982) climatology in the mid-high latitudes as well as in the tropical region. During the 70 years time integration, however, the model has some climatic drift in the subsurface ocean at the high latitude especially at the Antarctic sea and the North Atlantic. An overall feature of the SST pattern is reasonably reproduced. Some discrepancies from the observation, however, are seen. The temperature of the warm water in the western equatorial Pacific is slightly higher than 30°C while the observed one is less than 30°C. The model SST has generally warm bias in the warm water regions in the tropics.

Figure 2-2 shows the model climatology of the sea surface wind stress field for (a) January and (b) July. Overall features of the observed wind stress (Hellermann and Rosenstein, 1983) are well reproduced. The westerly winds associated with storm tracks in the northern midlatitude and the northeasterly trade winds are realistic not only in direction but also in amplitude. Since the model Aleutian low is slightly shifted westward, the wind stress in the central north Pacific has larger northward component compared to that of the observations. The southeasterly trades of the model are less extending to the equator especially in the west off Peru and off Brazil. Generally, the meridional component of the model wind stress in the tropics is small compared to the observed one. In July (Fig. 2-2b), the strong southwesterly wind stress which is related to the Indian summer monsoon is reasonably simulated.

In order to simulate realistic El Niño, it is crucial that the thermocline along the equator is adequately reproduced. Both annual mean field and seasonal variation of wind stress along the equator are closely linked to the thermocline structure along the equator. Figure 2-3 shows the seasonal variation of (a) the zonal wind stress and (b) the meridional wind stress both along the equator. These are compared with the observational wind stress of Hellermann and Rosenstein (1983). In the comparison, the observational wind stress of Hellermann and Rosenstein (1983) is multiplied by 0.75, because it is considered to be overestimated (Stockdale et al., 1993). In January, zonal wind stress in the model shows good agreement with the observation. In April, the observed easterly wind stress is weakened in the central Pacific, although the model keeps easterly wind stress as large as that in January. The model simulates the easterly wind stress in the central equatorial Pacific about 50% larger than that of the observed one during April through July. The zonal wind stress in the eastern coast of the Pacific in the model has relatively large westerly

component compared to the observation. The northward winds play an significant role in establishing the equatorial asymmetric SST distribution through atmosphere-ocean feedbacks (Xie, 1997) associated with wind-evaporation, coastal upwelling and cold currents along the eastern coast of the Pacific and the Atlantic. Southerly wind stress in the model is weak compared to the observation in the equatorial east-central Pacific and Atlantic especially during July to October.

Figure 2-4 shows the vertical cross section of annual mean temperature along the equator for (a) the model and for (b) the observation (Levitus, 1982). The model succeeded in representing the Pacific equatorial thermocline structure. In the most part of the Pacific sector, the model simulates the depth of the 20°C isotherm with good agreement with the observation. At the eastern coast, however, the 20°C isotherm decline toward east, which is not seen in the observation. This is caused by a downwelling due to the unrealistic westerly wind stress in the eastern coast (Fig. 2-3a), probably related to insufficient atmospheric resolution, and weak advection of cold water due to weak southerly wind stress along the west coast of South America (Fig. 2-3b). At all the longitudes, the model thermocline is diffuse compared to that of observation. The model fails to reproduce the eastward gradient of the thermocline in the Indian Ocean. This is related to discrepancy of the wind direction at the equator, which is associated with difference of southward extent of the westerly Indian summer monsoon between the model and the observation.

The structure of the subsurface basin-scale gyre is mainly controlled by the vorticity input of the large scale wind stress. Figure 2-5 depicts the climatology of the annual mean ocean temperature of the subsurface (275 m depth) for (a) the model and (b) the observation (Levitus, 1982). An overall pattern of the principal subtropical gyres is reproduced in the model. It is recognized, however, that the model shows a weaker temperature gradient in the strong current regions compared with the observed field. Since horizontal resolution ($2.5^\circ \times 2^\circ$) is not enough, the model simulates the Kuroshio transport only 38 *Sv* ($\times 10^6\ m^3\ s^{-1}$) at maximum. The Kuroshio Extension is shifted north (around 40°N). The subpolar gyre of the northern North Pacific is not sufficiently reproduced in the model.

A series of experiments on the global warming projection was performed with the MRI-CGCM1 (Tokioka *et al.*, 1996). The model simulated an increase in global mean surface air temperature of 1.6°C in 70 years in the experiment with atmospheric CO_2 increasing by 1% per year compound. The result was comparable with an average of results from other modeling groups (IPCC, 1996). The model reveals a good performance in simulating the Asian summer monsoon as well as ENSO. The ENSO-monsoon relationship in the interannual variability is consistent with observation, where a good monsoon is associated with La Niña (Kitoh et al., 1999). Using this strength, changes in the Asian summer

monsoon in the global warming experiment were investigated (Kitoh et al., 1997).

2.3 MRI-CGCM2

The new version of the global coupled ocean-atmosphere general circulation model (MRI-CGCM2) is developed at the MRI, intending to enable climate change simulations with higher accuracy and reliability. Although the MRI-CGCM1 showed a fairly good performance in many aspects, it had several serious drawbacks. Firstly, the model showed a large climatological drift, which made it difficult to run beyond 150 years. Secondly, the model failed to simulate the thermohaline circulation in the Atlantic Ocean. Associated with this defect, there was no simulation of an increase minimum of surface temperature in the North Atlantic with the CO_2 increase experiment, while an increase minimum is seen in results from many other models. The third problem was poor representation of sea ice. For the Norwegian Sea, the model simulated unrealistic sea ice cover that is not observed, resulting in a spurious large temperature increase by melting in the CO_2 increase experiment. The Antarctic sea ice showed a trend of gradual decrease even in the control run, which caused difficulties in interpreting the Antarctic sea ice change in the warmer climate with the model experiment. The fourth problem was associated with the ENSO simulation, in which MRI-CGCM1 showed the equatorial SST anomaly maximum west of the date line. This location is further westward than observed.

In developing the MRI-CGCM2, we aimed at eliminating the above drawbacks and achieving a better performance in reproducing the mean climate and the climate variability than MRI-CGCM1. The differences of the model specification between MRI-CGCM1 and MRI-CGCM2 are summarized in Table 2-1.

2.3.1 Atmospheric Model

The atmospheric component of the model is a version of the new spectral AGCM (MRI/JMA98). This AGCM has been developed based on a version of the operational weather forecasting model of the Japan Meteorological Agency (JMA). Some physical process components are replaced with those of the original JMA version. Details of the AGCM are described in Shibata *et al.* (1999), so only an outline is given here.

The dynamic framework is completely replaced by a spectral transform method, while the AGCM in the MRI-CGCM1 was a grid model (5° × 4°, 15 levels). The horizontal resolution is T42 in wave truncation and 128 × 64 in a transformed Gaussian grid (grid spacing approximately 2.8° × 2.8° in longitude and latitude). The vertical configuration consists of a 30-layer sigma-pressure hybrid coordinate with the top at 0.4 *hPa*.

As in the MRI-CGCM1, a multi-parameter random model based on Shibata and Aoki

(1989) is used for terrestrial radiation. In the present version, absorption due to CH_4 and N_2O is treated in addition to H_2O, CO_2 and O_3. The model calculates solar radiation formulated by Shibata and Uchiyama (1992) with delta-two-stream approximation. An explicit treatment of the direct effect of sulfate aerosols is possible in this scheme. The optical properties (diffusivity, single scattering albedo and asymmetry parameters) of sulfate aerosol are substituted by those for the LOWTRAN rural aerosol, which is composed of a mixture of 70% water-soluble substance (ammonium and calcium sulfate and organic compounds) and 30% dust-like particles. Since complex refractive indices for water-soluble and dust-like aerosols are very similar, particularly in the solar wavelength region, and can be regarded as identical in a first-order approximation, those parameters are applicable for sulfate aerosols as a whole. The effects of relative humidity on solution concentration and radius distribution of aerosols are incorporated.

For deep moist convection, the Arakawa-Schubert scheme with prognostic closure similar to Randall and Pan (1993) is used. For other physical parameterizations, mid-level convection that is moist convection rooted in a free atmosphere, large-scale condensation, vertical diffusion with a level-2 turbulence closure scheme based on Mellor and Yamada (1974), orographic gravity wave drag scheme developed by Iwasaki *et al.* (1989) and Reyleigh friction as a non-orographic gravity wave drag are used.

2.3.2 Ocean Model

The oceanic component of the model is a Bryan-Cox type OGCM with a global domain, and its basic dynamic configuration is the same as in the MRI-CGCM1. The horizontal grid spacing is 2.5 degrees in longitude and 2 degrees in latitude poleward of 12 degrees in both hemispheres. Near the equator, between 4°S and 4°N, the meridional grid spacing is set 0.5 degrees in order to provide good resolution of equatorial oceanic waves. The grid spacing gradually increases from 0.5 degrees to 2 degrees for latitudes of 4 to 12 degrees. The vertical level spacing is given in Table 2-2. The uppermost layer has 5.2 *m* thickness and the deepest bottom is set to 5000 *m*. There are two more levels for the upper thermocline than in the MRI-CGCM1, aiming at a better representation of oceanic waves playing an important role in decadal to interdecadal climate variability.

The Denmark Strait is made slightly deeper and broader than the real topography to represent sub-grid scale overflow of waters formed in the Nordic Seas. This modification contributes somewhat to the improvement of thermohaline circulation in the North Atlantic, which will be shown later.

Parameterized sub-grid mixing processes using viscosities and diffusivities are specified as follows: the horizontal viscosity coefficient is $1.6 \times 10^5\ m^2\,s^{-1}$ and the vertical viscosity coefficient is $1 \times 10^{-4}\ m^2\,s^{-1}$. A new feature of the OGCM is the introduction of eddy

mixing parameterization based on Gent and McWilliams (1990). Its isopycnal mixing coefficient is $2 \times 10^3\ m^2 s^{-1}$ and diapycnal mixing coefficient is $1 \times 10^{-5}\ m^2 s^{-1}$. The horizontal and vertical diffusivity coefficients of the MRI-CGCM1were 2.5 times and five times larger than the isopycnal and diapycnal coefficients of the MRI-CGCM2. With these diffusivity coefficients, the temperature gradient across the oceanic fronts becomes sharper, leading to stronger oceanic circulations and meridional overturnings than in the MRI-CGCM1. To simulate the surface mixed layer, vertical turbulence viscosity and diffusivity following Mellor and Yamada (1974, 1982) and Mellor and Durbin (1975) are modeled in addition to isopycnal mixing. When vertical stratification becomes unstable, a convective adjustment is applied by mixing the whole vertical column. Solar radiation penetrating seawater is absorbed with an e-folding of 10 *m*-depth, heating the surface seawater to several dozen meters.

2.3.3 Sea Ice Model

The sea ice model is basically the same as in the MRI-CGCM1, that is, similar to the model by Mellor and Kantha (1989). Compactness and thickness are predicted based on thermodynamics and advection. The freezing (melting) rate of sea ice is calculated with balances of heat and freshwater at the sea ice bottom, the open sea surface and within seawater (creation of frazil ice).

Compactness is calculated using empirical constants (these are tuning parameters). The sea ice is advected by the surface ocean current multiplied by an empirical constant (set to 1/3 at present). Compactness is also advected by the surface ocean current, though it is limited to a maximum value of 0.997 in the Northern Hemisphere (NH) and to 0.98 in the Southern Hemisphere (SH). If the sea ice becomes very thick, gaps in sea ice (leads) are difficult to be filled by freezing at the sea surface, which results in the unlimited increase of sea ice by freezing at leads. In order to avoid this problem, we set compactness to the maximum values quoted above for sea ice thicker than 3 m for the NH and 1 m for the SH.

2.3.4 Coupling Scheme

The atmosphere and the ocean interact with each other by exchanging fluxes of heat, freshwater and momentum at the sea surface. The contents of the fluxes are sensible and latent heat fluxes, and net shortwave and longwave radiation, precipitation and evaporation, river discharge and melt-water from snow and ice over sea ice, and zonal and meridional components of the surface wind stress. The fluxes are exchanged every 24 hours in the model. The AGCM (including land model) is integrated for 24 hours and outputs averaged fluxes at the sea surface. The fluxes are transferred to the OGCM grid, with the budgets preserved. The OGCM (including sea ice model) is then integrated for 24 hours,

and outputs the resulting SST and sea ice compactness and thickness for updating the lower boundary for the AGCM. The time integration of the CGCM proceeds by repeating these procedures.

Since the grid boundary of the AGCM does not match that of the OGCM, the AGCM calculates fluxes independently for three surface conditions (land, sea and sea ice), considering fractional coverage in a single grid box. The AGCM treats averaged flux with area weighting as a flux at the atmosphere bottom. In this coupling process, heat and freshwater are transferred, preserving rigorous budgets.

2.3.5 Spin-up and Flux Adjustment

It is a difficult and important task to obtaining a quasi-equilibrium state of coupled atmosphere and ocean as an initial condition for experiments with the CGCM. The time scale of the ocean response to forcing ranges from several years to several decades even for the upper ocean, (depending, for example, on the latitudes of the variation), and more than a thousand years for the deep ocean. Therefore, the coupled model generally needs long-term spin-up, though it depends on the objective time scale of the experiment. We made a spin-up of the model, preparing for 200-year climate change experiments as shown in Table. 2-3.

As the response time of the ocean is much longer than that of the atmosphere, we made a spin-up of the ocean with an asynchronously coupled run (SPIN-UPs 1–5, 209-year) in order to save computational time. We ran the OGCM and the AGCM by turns of different length. A synchronously coupled spin-up of a further 111 years was then applied (SPIN-Ups 6-8). The forcing data and the boundary conditions vary at each stage of the spin-up as shown in Table.2-3, because we tried to avoid any abrupt shock to the coupled system from changing numerous conditions simultaneously.

In order to keep the model climatology of the control run close to the observed one, we used flux adjustments for heat and freshwater obtained from the spin-up run. Figure 2-6 shows geographical distribution of annual mean flux adjustments for heat and freshwater together with those in the MRI-CGCM1 for comparison. The flux adjustments for heat and freshwater in the new model are generally smaller than in MRI-CGCM1. Major features of the adjustments, such as heating in the equatorial Pacific and cooling around Japan and Newfoundland, are common to both models, in spite of completely different AGCMs. It is supposed that these large heat adjustments arise from insufficient representation of small-scale ocean dynamic effects such as equatorial waves, western boundary currents and coastal upwelling. Most other regions (where effects of such ocean dynamics are small) show smaller adjustments of less than 25 Wm^{-2} in the MRI-CGCM2, whereas a relatively large proportion of regions have adjustments greater than 25 Wm^{-2} in

the MRI-CGCM1. Cooling in most coastal regions is notable in the new model. This is related to the lack of clouds, because the spectral atmospheric model cannot represent as sharp a land-sea humidity contrast as a grid model. The freshwater flux adjustment is generally large at river mouth points. In the Arctic Sea, there are large, patchy adjustment regions both positive and negative in value. Most other regions show relatively smaller adjustments of less than 5 mm/day. Compared to the former model, the negative freshening (salting) adjustment in the Norwegian Sea is much smaller. It is considered that the stronger North Atlantic thermohaline circulation contributes to the reduction of the freshwater adjustment.

Figure 2-7 shows the meridional distribution of the zonal mean fluxes and flux adjustments for heat and freshwater, for December to February (DJF) and June to August (JJA). Fluxes based on observational estimation are also shown for comparison. The observational heat flux is from Da Silva et al. (1994), and the observational freshwater flux is the evaporation by Da Silva et al. (1994), subtracting the precipitation by Xie and Arkin (1996). Observational data are poor poleward of 45°S and 60°N.

The model's heat fluxes agree with observations in most latitudes, though there is overestimation of heating in summer at latitudes higher than 30 degrees in both hemispheres. Some of these biases are compensated for by the flux adjustment. However, at some latitudes (e.g. near the equator), the adjusted flux shows a larger bias than the original flux. The flux adjustments try to compensate for biases of the oceanic transports, as well as for biases of the atmospheric fluxes. For example, the strong heating adjustment near the equator implies compensation for cooling by too strong equatorial upwelling.

The freshwater fluxes agree with the observational estimation except for the equatorial region and the midlatitudes in boreal winter. However, large freshwater adjustments are seen, especially in the high latitudes. It is difficult for coupled models to successfully simulate the observed salinity distribution, since there is no explicit damping effect by the atmosphere on salinity anomalies, unlike with temperature.

Adjustments are made for wind stress only in the equatorial region to accurately represent the climatological thermocline structure along the equator, which plays a crucial role in model performance when simulating ENSO. On the equator (4°S to 4°N), the differences of climatology between the model and the observation (Hellerman and Rosenstein, 1983) are added to the model's wind stress. A nine-point smoothing in zonal direction is applied to the adjustments. Off the equator (12°S to 4°S, 4°N to 12°N), the adjustment decreases with latitude and is set to zero poleward of 12°S and 12°N. The climatological wind stresses (zonal and meridional components) together with their

adjustments for January and July are shown in Fig. 2-8. The adjustment of the zonal component is small except in the western Indian Ocean (January and July) and the western Pacific (July). The meridional component is generally enhanced by the adjustment, particularly in the eastern Pacific and the eastern Atlantic (January and July).

2.4 Climatology of the MRI-CGCM2

We made a 400-year control run of the model. This run is used as a reference for the experimental projections of the global warming. Concentrations of the greenhouse gases are set constant at 348 *ppmv* for CO_2, 1.650 *ppmv* for CH_4 and 0.306 *ppmv* for N_2O. The seasonally varying ozone profile is prescribed to climatological data taken from Wang *et al*. (1995).

The climate of the three-dimensional structure of the simulated atmosphere is similar to that of the L30 version of MRI/JMA98 by Shibata *et al*. (1999). There are many changes in the AGCM from the MRI-CGCM1. It is difficult to interpret the differences of the model results because many processes with different schemes are interacting in the simulations. We now focus on the climate of near surface fields that directly affect the ocean and the coupled system.

We used the last 30-year average of the 200-year run as the model climatology. We tested the model evaluation with different 30-year averages and confirmed that the interdecadal variations do not affect the essential features of the differences between observation and model.

Figure 2-9 shows climatological SST (JFM; January-March, JAS; July-September) for the model and the observation (Levitus and Boyer, 1994). The heat flux adjustment works effectively, so the model SST is sufficiently close to the observed climatology. Differences are less than 1°C in most regions in each season. As an exception, deviation around Japan in winter (JFM) is a few degrees higher. The Kuroshio and its extension are simulated north of the observed location and, therefore, an excessively large amount of oceanic heat is transported from the lower latitudes, which cannot be compensated for with atmospheric cooling and flux adjustment. The SST in sea ice edge regions tends to be colder (1 - 2°C) than observed. In these regions, small differences in sea ice distribution lead to a large temperature difference. Since relatively large interannual and interdecadal variations of sea ice edge distribution are known though observations are scarce, there might be some problem in the reliability of the observed SST in these regions.

The thermocline structure along the equator, which is closely related to the behavior of ENSO in the model, is shown in Fig. 2-10. In the Pacific Ocean, the thermocline is more vertically diffuse than the observed one, but it is sharper than that in the MRI-CGCM1.

Associated with these vertical temperature gradients, the MRI-CGCM2 simulates the equatorial undercurrent with a maximum of 0.35 $m\,s^{-1}$ for the annual mean. This is stronger than the MRI-CGCM1 by 50%. The model adequately reproduces the eastward slanted thermocline in the Indian Ocean, along with upwelling at the western boundary, which is much improved compared to MRI-CGCM1. At the eastern edge of the Pacific and Atlantic Oceans, the model's thermocline tends to be deeper than observed.

The improved performance of the MRI-CGCM2 in reproducing climate of other fundamental values, such as meridional energy transport, geographical distributions of surface heat flux, precipitation and ocean Sverdrup flow, and meridional overturning and seasonal distributions of sea ice, is described in Appendix. These are not directly linked with the present study but are important as the basic state on which various (both direct and indirect) interactions take place.

2.5 Summary

Two versions of the global coupled ocean-atmosphere general circulation model are developed at MRI. The MRI-CGCM1 reproduced the annual mean state and seasonal variation both in the atmosphere and the oceans, reasonably comparable with the observation. The MRI-CGCM2 is developed, with reducing the shortcomings of the MRI-CGCM1, for achieving more realistic climatic mean and variability to predict climate changes with greater accuracy and reliability. The model shows generally good performance, reproducing representative aspects of the mean climate and seasonal variation including wind stress, sea surface temperature and upper ocean temperature.

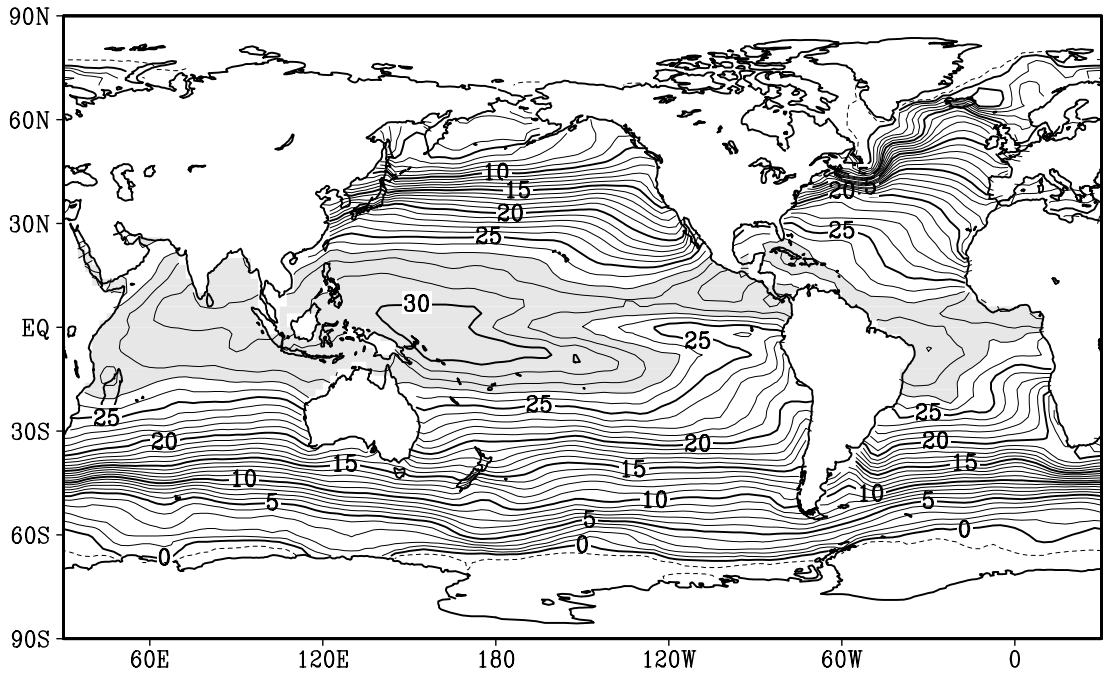

Figure 2-1 Climatology of the annual averaged SST in the MRI-CGCM1. Contour interval is 1 °C. Regions higher than 27 °C are shaded.

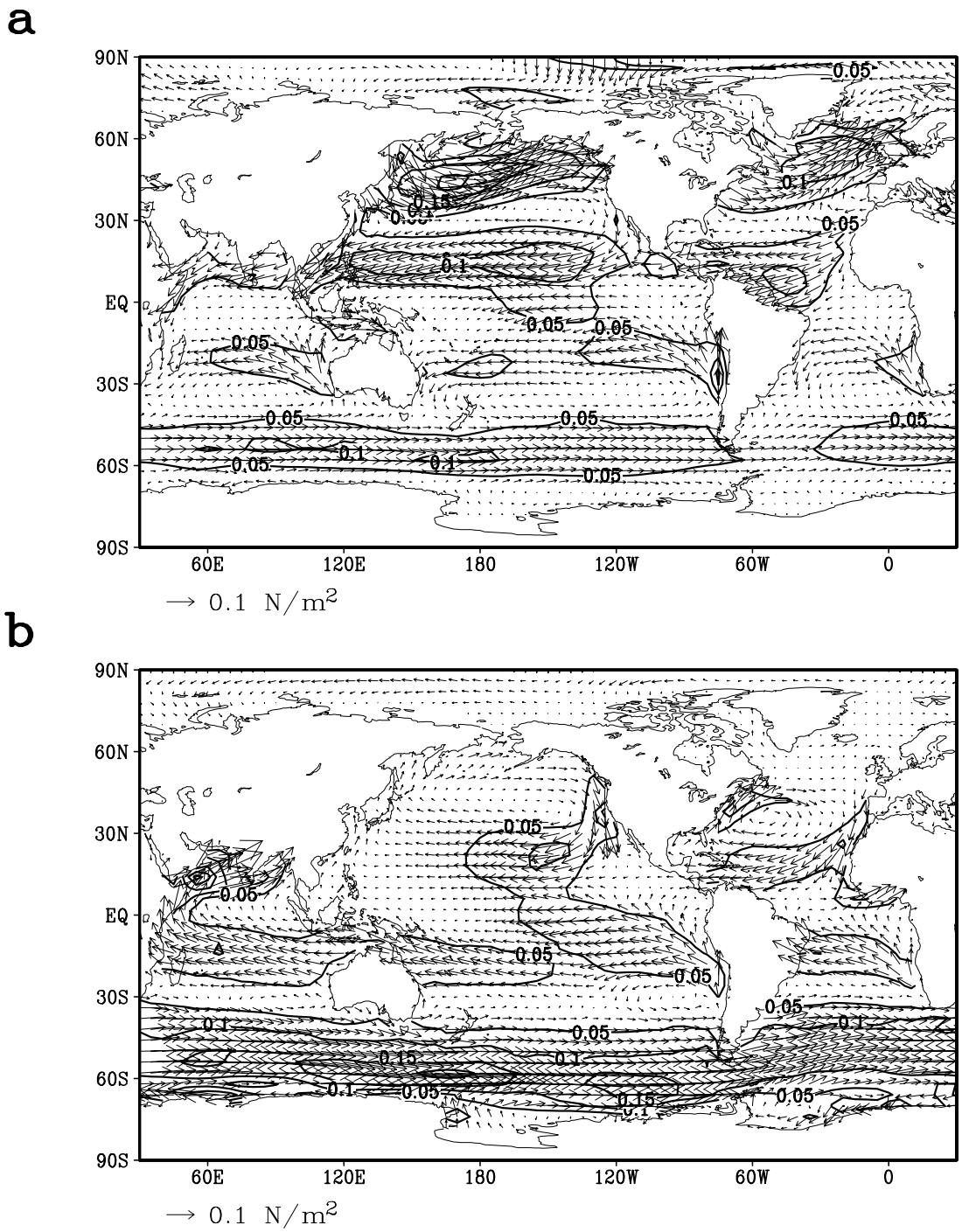

Figure 2-2 Model climatology of the wind stress at the ocean surface for (a) January and (b) July. Reference arrow denotes 0.1 Nm^{-2}. Contour plot shows magnitude of wind stress with interval of 0.05 Nm^{-2}.

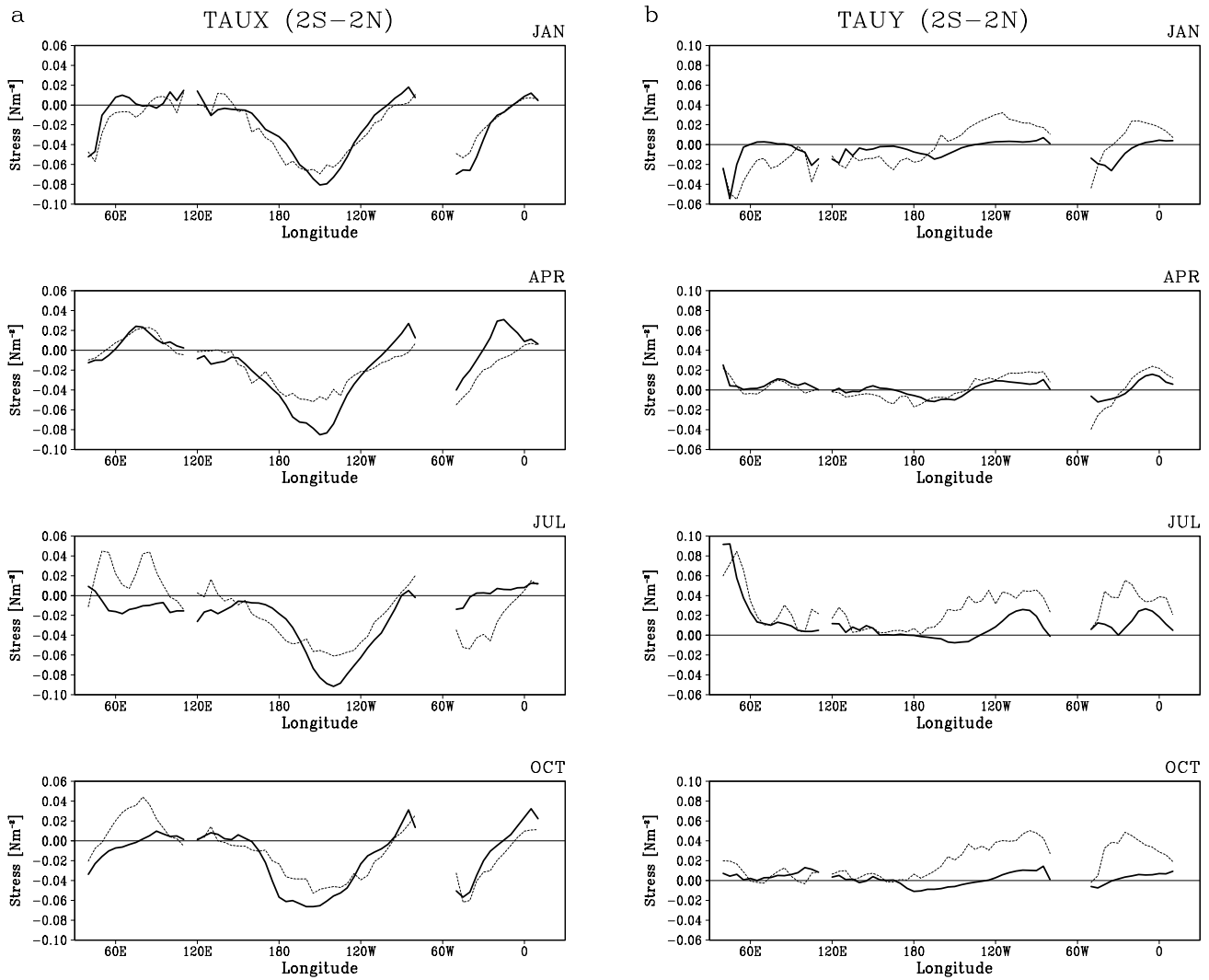

Figure 2-3 Seasonal variation of (a) zonal wind stress and (b) meridional wind stress along the equator (average between 2S and 2N) for the model climatology (solid line) and the observed climatology (Hellermann and Rosenstein, 1983) multiplied by 0.75 (dashed line), respectively.

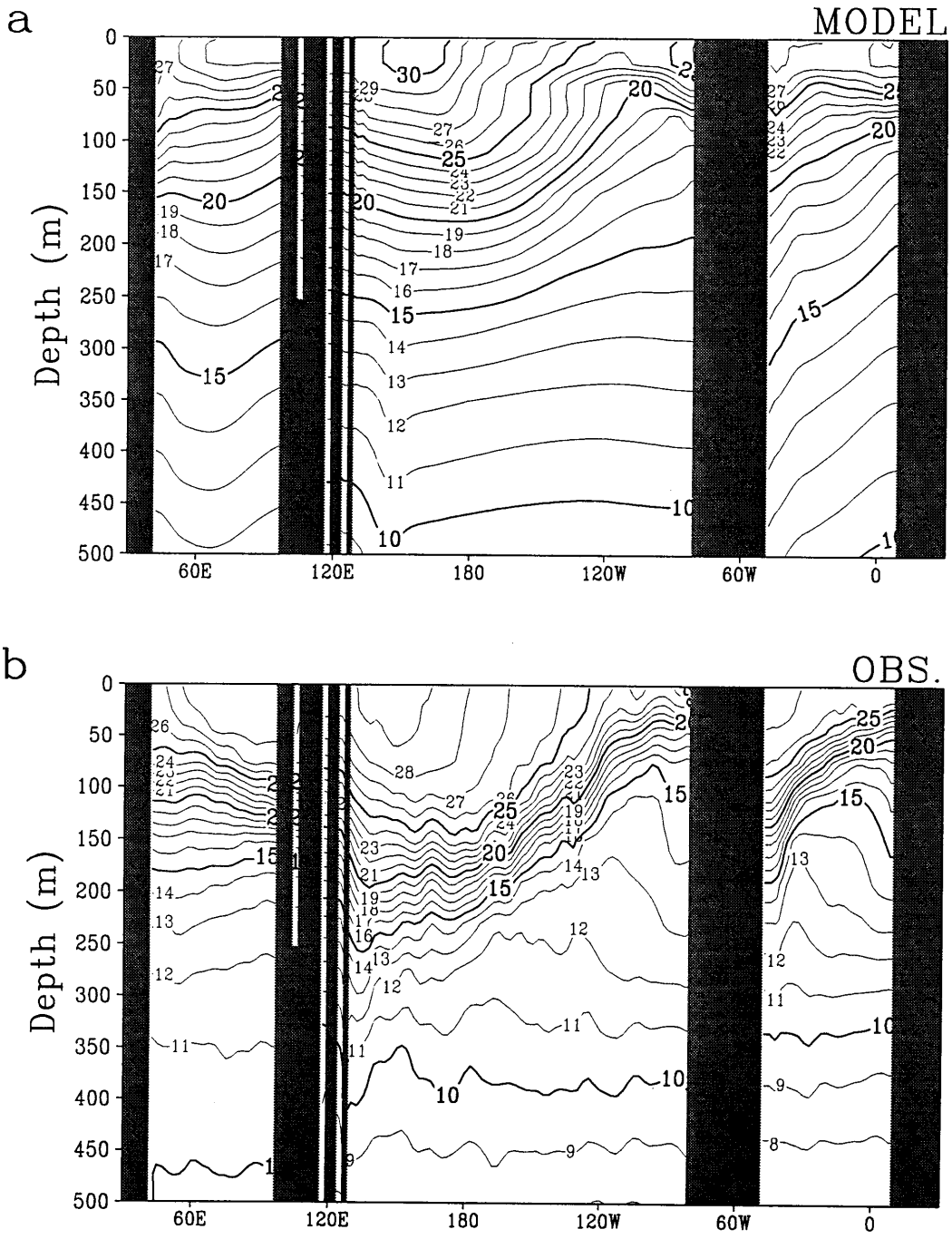

Figure 2-4 Longitude-depth cross-section of the annual mean ocean temperature along the equator for (a) the model climatology and (b) the observed climatology (Levitus, 1982). Contour interval is 1 °C.

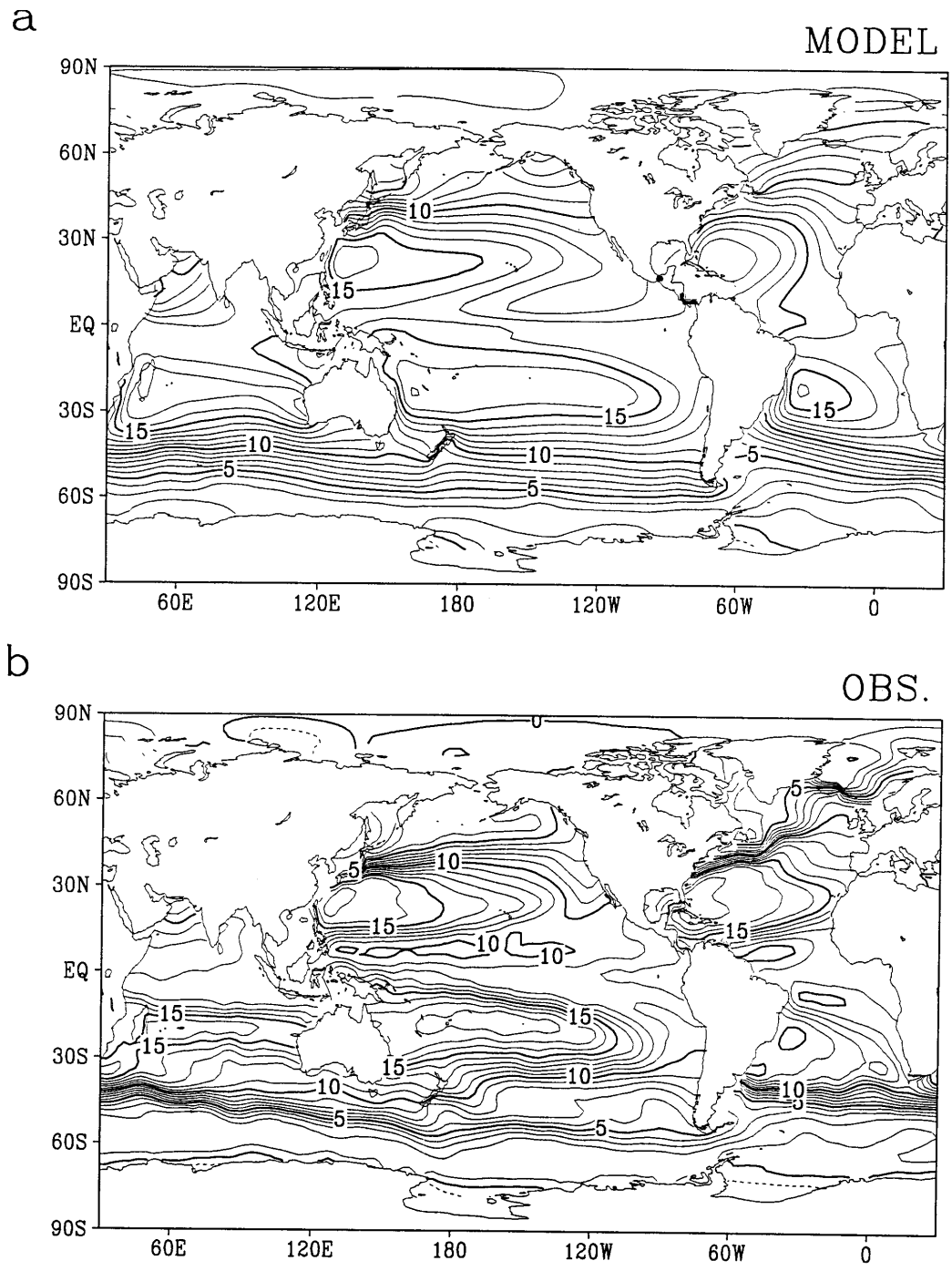

Figure 2-5 Annual mean ocean temperature at 275m depth for (a) the model climatology and (b) the observed climatology (Levitus, 1982). Contour interval is 1 °C.

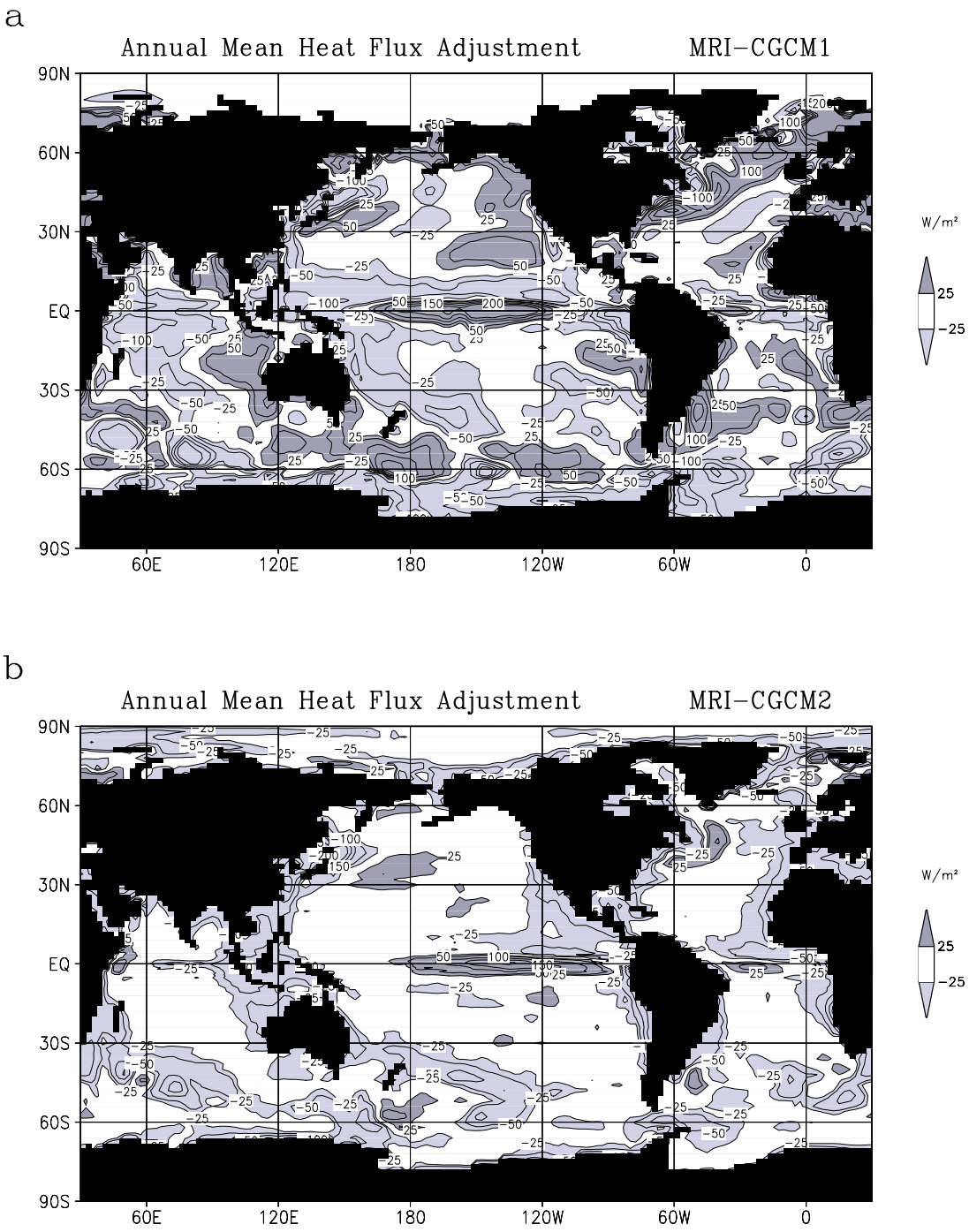

Figure 2-6 Climatological annual mean heat flux adjustments (Wm^{-2}) in (a) the MRI-CGCM2 and (b) the MRI-CGCM1, and freshwater flux adjustments (mm/day) in (c) the MRI- CGCM2 and (d) the MRI-CGCM1.

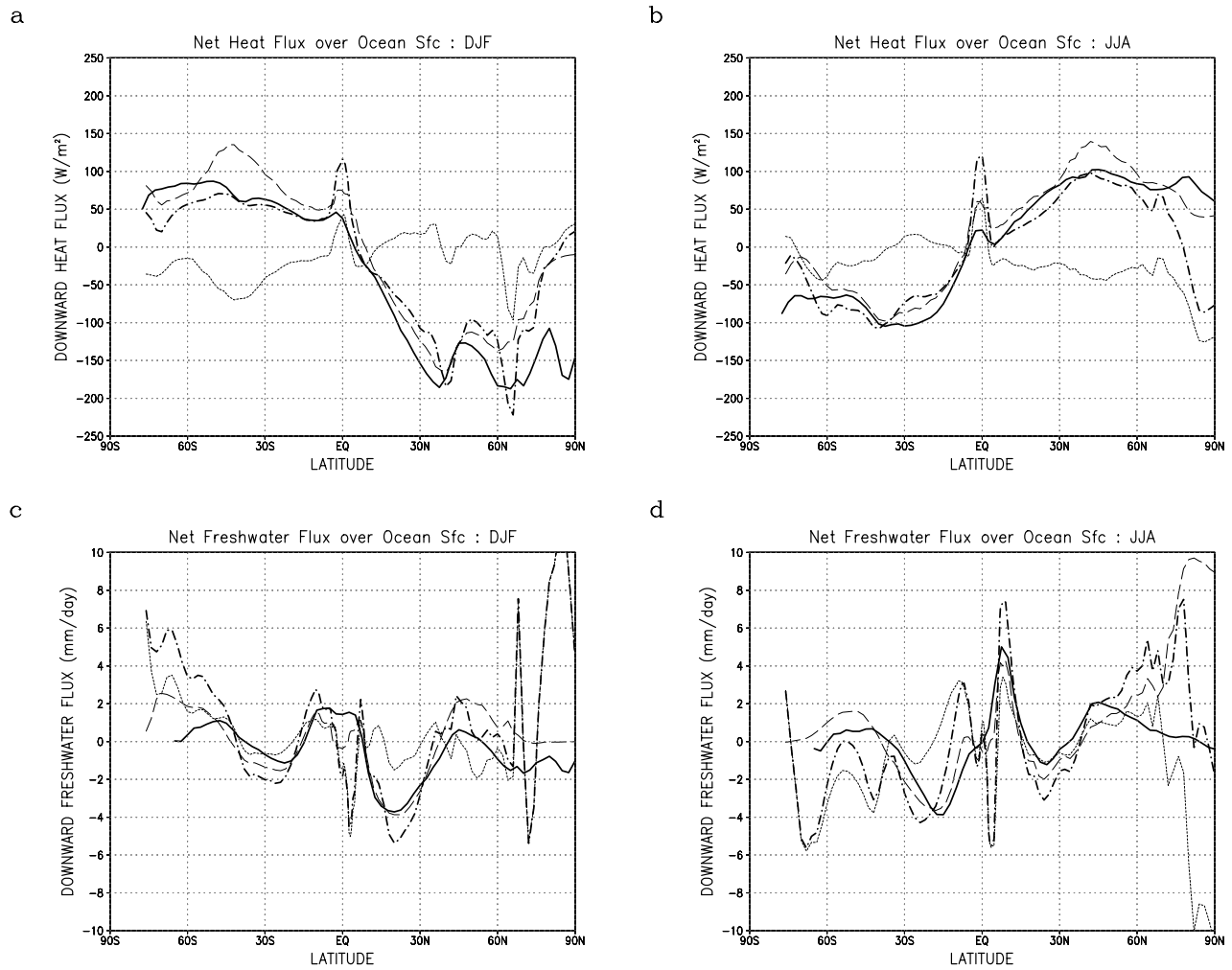

Figure 2-7 Zonally averaged net surface heat flux for (a) December-February (DJF) mean and (b) June-August (JJA) mean, and freshwater flux for (c) DJF and (d) JJA. (solid: observation, long-dash: atmospheric model, short-dash: flux adjustment, dot-dash: model adjusted). The observed heat flux is from Da Silva et al. (1994), and freshwater flux for the observation is estimated by precipitation (Xie and Arkin, 1996) minus evaporation (Da Silva et al., 1994).

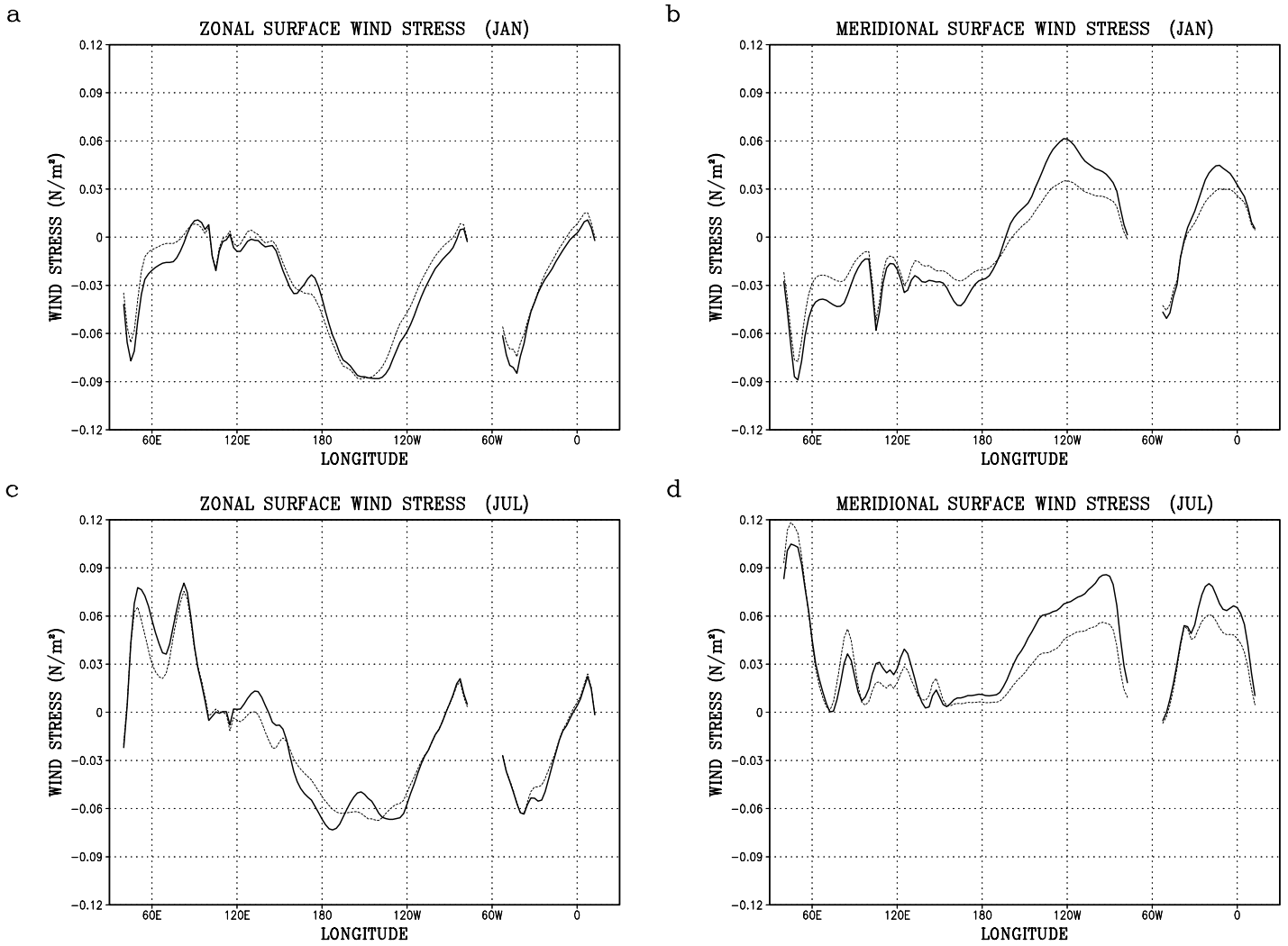

Figure 2-8 Zonal distribution of the wind stress along the equator (averaged in the 4°S-4°N band), calculated by the atmospheric model (dashed curve) and adjusted (solid curve) for January (a, zonal component; b, meridional component) and July. (c, zonal component; d, meridional component). Unit is Nm^{-2}.

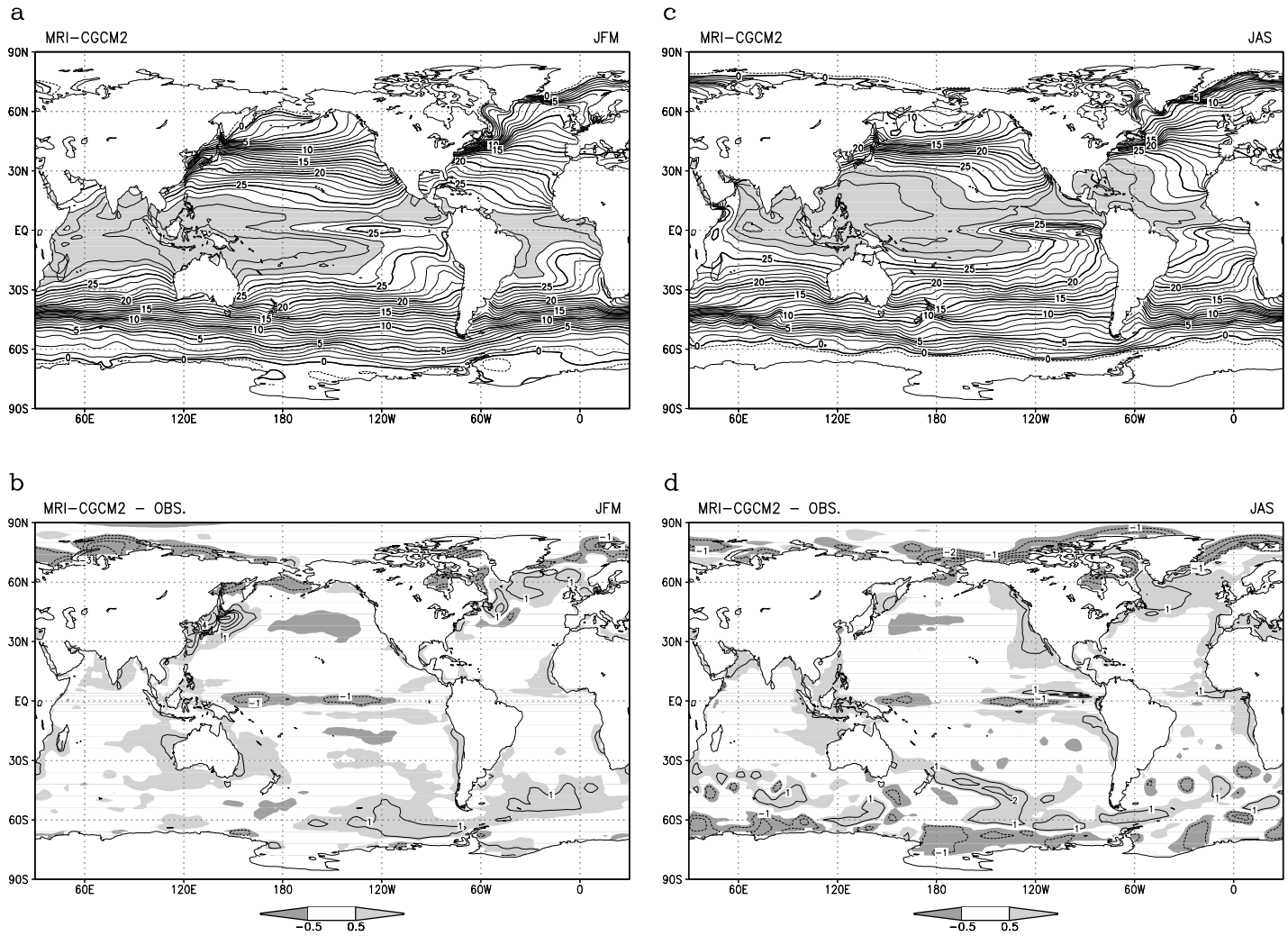

Figure 2-9 Geographical distribution of the climatological sea surface temperature for January-March (JFM) mean (a, MRI-CGCM2; b: difference from the observation) and July-September (JAS) mean (c, MRI-CGCM2; d, difference from the observation). The observation is from Levitus and Boyer (1994).

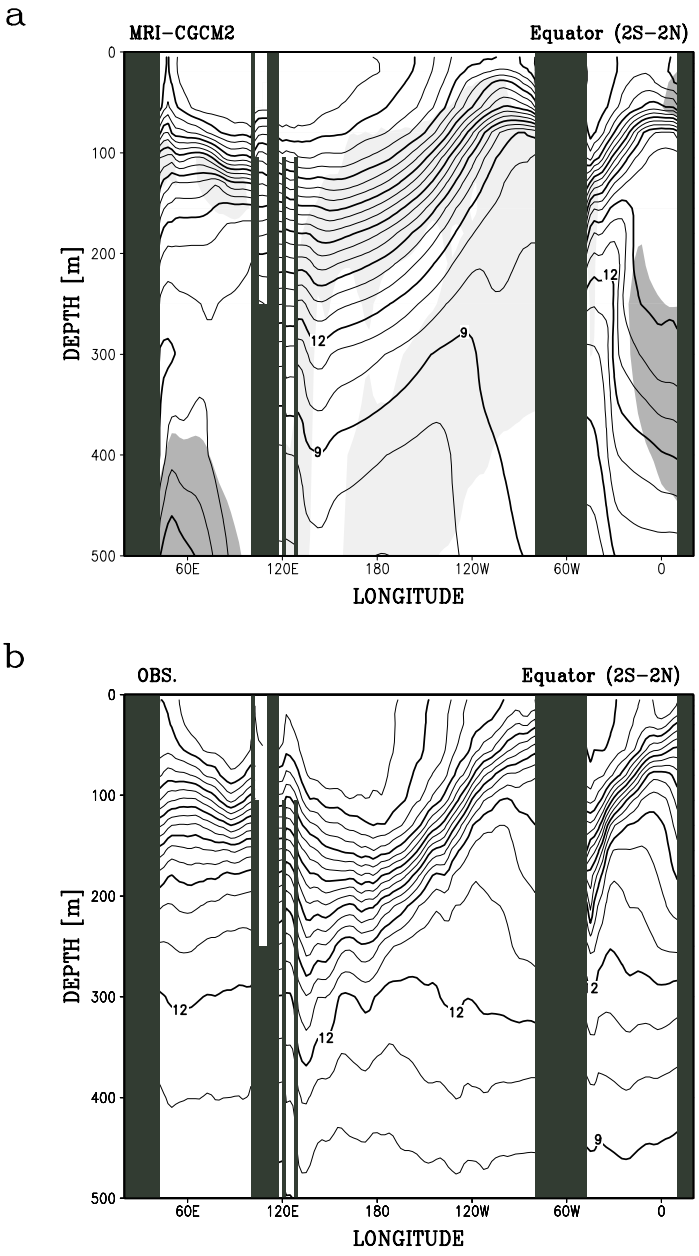

Figure 2-10 The annual mean potential temperature along the equator (averaged 2°S to 2°N) for (a) MRI-CGCM2 and (b) observation (Levitus and Boyer, 1994). The differences from the observations larger than 1°C are shown with shading (positive, dark shading; negative, light shading) in plot (a).

Table 2-1. Specifications of the MRI-CGCM1 and the MRI-CGCM2

Aspect	MRI- CGCM1	MRI-CGCM2
Atmospheric component		
Horizontal resolution	5°(long.) × 4°(lat.)	T42 (~2.8° × 2.8°)
Layer (top)	15 (1hPa)	30 (0.4hPa)
Solar radiation (SW)	Lacis and Hansen (1974) H_2O, O_3	Shibata and Uchiyama (1992) H_2O, O_3, aerosol
Long-wave radiation (LW)	Shibata and Aoki (1989) H_2O, CO_2, O_3	Shibata and Aoki (1989) H_2O, CO_2, O_3, CH_4, N_2O
Convection	Arakawa and Schubert (1974)	Prognostic Arakawa-Schubert Randall and Pan (1993)
Planetary Boundary Layer (PBL)	Bulk layer (Tokioka et al., 1988)	Mellor and Yamada (1974)
Gravity wave drag	Palmer et al. (1986) Rayleigh friction	Iwasaki et al. (1989) Rayleigh friction
Cloud type	Penetrative convection, Middle-level convection, Large-scale condensation, Stratus in PBL	Penetrative convection Large-scale condensation
Cloudiness	Saturation	function of relative humidity
Cloud overlap	random for non-convective clouds 0.3 for convective clouds	random + correlation
Cloud water content	function of pressure and temperature	function of temperature
Land process	4-layer diffusion model	3-layer SiB
Oceanic component		
Horizontal resolution	2.5° (lon.) × 2°-0.5° (lat.)	
Layer (min. thickness)	21 (5.2m)	23 (5.2m)
Eddy viscosity	Horiz. visc. 2.0×10^{5} m^2s^{-1} Vert. visc. 1×10^{-4} m^2s^{-1}	Horiz. visc. 1.6×10^{5} m^2s^{-1} Vert. visc. 1×10^{-4} m^2s^{-1}
Eddy mixing	Horizontal-vertical mixing Horiz. diff. 5.0×10^{3} m^2s^{-1} Vert. diff. $5.0\times10^{-5}m^2s^{-1}$	Isopicnal mixing + Gent and McWilliams (1990) Isopycnal 2.0×10^{3} m^2s^{-1} Diapycnal 1.0×10^{-5} m^2s^{-1}
Vertical viscosity and diffusivity	Mellor and Yamada (1974, 1982)	
Sea ice	Mellor and Kantha (1989)	
Atmosphere-ocean coupling		
Coupling interval	6 hours	24 hours
Flux adjustment	heat, salinity	heat, salinity + wind stress (12°S-12°N)

Table 2-2. Vertical level spacing in the ocean model of the MRI-CGCM2

Level	Level spacing (m)	Depth of level center (m)	Depth of level bottom (m)
1	5.2	2.8	5.2
2	6.2	8.3	11.4
3	7.9	15.35	19.3
4	10.7	24.65	30.0
5	25.0	42.5	55.0
6	25.0	67.5	80.0
7	25.0	92.5	105.0
8	25.0	117.5	130.0
9	25.0	142.5	155.0
10	25.0	167.5	180.0
11	30.0	195.0	210.0
12	40.0	230.0	250.0
13	50.0	275.0	300.0
14	100.0	350.0	400.0
15	200.0	500.0	600.0
16	200.0	700.0	800.0
17	300.0	950.0	1100.0
18	400.0	1300.0	1500.0
19	700.0	1850.0	2200.0
20	700.0	2550.0	2900.0
21	700.0	3250.0	3600.0
22	700.0	3950.0	4300.0
23	700.0	4650.0	5000.0

Table 2-3. Spin-up runs for the control run

Run	Model	Prescribed forcing data	Integration period (years)	Forcing data output for the subsequent run (averaged years)
SPIN-UP1	OGCM	SSTo, SSSo, TAUo, Sio	24	--
SPIN-UP2	AGCM	SSTo, Sio	24	Flux-A1 (10)
SPIN-UP3	OGCM	Flux-A1, SSTo, SSSo, TAUo, SIo	30	--
SPIN-UP4	AGCM	SST-O2, Sio	16	Flux-A2 (10)
SPIN-UP5	OGCM	Flux-A2, SSTo, SSSo, TAUo, SIo	155	--
SPIN-UP6	CGCM	SSTo, SSSo, TAUo, Sio	65	Fadj-C1 (10)
SPIN-UP7	CGCM	Fadj-C1, Sio	17	--
SPIN-UP8	CGCM	Fadj-C1	29	--
CONTROL	CGCM	Fadj-C1	201	--

SSTo: Observed climatological sea surface temperature (Levitusand Boyer, 1994)
SSSo: Observed climatological sea surface salinity (Levitus et al., 1994)
TAUo: Observed climatological surface wind stress (Hellerman and Rosenstein, 1983)
SIo: Observed climatological sea ice distribution (SIGRID by Navy-NOAA Joint Ice Center, Bourke and Garrett, 1987)
Flux-*run*: Climatological surface fluxes (for heat, freshwater and momentum) obtained from the *run*
SST-*run*: Climatological sea surface temperature obtained from the *run*
Fadj-*run*: Climatological flux adjustment (for heat, freshwater and momentum) obtained from the *run*

3 Spatial and Temporal Structures of the Variabilities in the Pacific

In this section, we overview variabilities in the Pacific reproduced in the MRI-CGCM1, and contrast with those in the slab ocean coupled model (MRI-SGCM1) to elucidate factors determining the structures. The spatial and temporal structures are examined for the SST variability. For interannual variabilities, the structures, temporal evolutions and their involved mechanisms are investigated, particularly for an ENSO-like variability in the tropical Pacific and the interannual variability in the midlatitude North Pacific.

3.1 Spatial and Temporal Structures of the SST Variability

3.1.1 Spectra of the SST Variability

To examine the overall temporal structures of the SST variability in the Pacific Ocean, the spectra are calculated for the annual mean SSTs for the observation, the MRI-CGCM1 and MRI-SGCM1, (referred to as AOGCM and SGCM, respectively, in this section), and compared among them. Figure 3-1 shows the power spectral density of each SST for the Pacific sector of the extratropical North Pacific, tropical Pacific and extratropical South Pacific. Spectra are calculated for each grid point then averaged over respective regions.

In the tropical Pacific, the observed SST shows distinct peaks at periods between 3 years and 7 years (Fig. 3-1a). These spectral peaks are significant in comparison with the spectrum for the extratropical Pacific at the same timescale. This timescale is recognized as the ENSO timescale. For decadal to interdecadal timescale, the observed SST in the tropical Pacific shows relatively flat (white) spectrum with a gap at 8 year period and a faint peak at around 15 year period, although these are not statistically significant. In the extratropical North Pacific, the observed SST shows rather red spectrum over the timescales through ENSO to interdecadal with nearly constant gradient of the spectral density. There seems no distinct peak except the peak at 6-year period. In the midlatitude North Pacific, the SST variability becomes more dominant in the longer timescales (in particular around the Kuroshio Extension, not shown), whereas in the tropics it is dominant in the ENSO timescale. The observed SST in the extratropical South Pacific shows similar spectrum with the tropical Pacific except for ENSO timescale, where the spectrum has smaller power and no distinct peak. Reliability for long-term variation in the South Pacific is relatively low due to the lack of the observation number.

The AOGCM shows a spectrum of the tropical SST with distinct peaks at periods

between 3 years and 7 years, which correspond to timescale of the model ENSO (Yukimoto et al., 1996) with consistent feature with the delayed oscillator mechanism for the observed ENSO. The AOGCM also reveals flat (white) spectral density curve in the longer timescales, which results in good agreement in both magnitude and gradient of the spectral property with the observed one. For the spectrum of the SST in the midlatitude North Pacific, the AOGCM well simulates the overall feature for the observation, though periods of small peaks are not necessarily coincident. The spectrum for the South Pacific SST show very similar feature with that for the tropical Pacific except for ENSO timescale, where the spectrum has smaller power and no distinct peak. This feature is also consistent with the observation.

The SGCM shows quite different spectral property compared with the observation and the AOGCM. Peaks in the ENSO timescale are not distinct, and magnitude in the overall timescale is much larger. Especially, the spectrum for the tropical Pacific SST shows very large variance in decadal to interdecadal timescales. The tropical Pacific SST reveals rather red spectral characteristic compared to the observed and AOGCM. In the SGCM, variability of the tropical SST depends on strong positive feedbacks between SST and stratus clouds in the eastern Pacific and convective clouds in the western Pacific, respectively (Kitoh et al., 1999). The reason why the tropical variability in the SGCM is so large is probably because there are no mechanism for damping SST anomalies with oceanic current and waves that would carry SST anomalies in the eastern Pacific to the west. This implies that the effective heat capacity of the ocean in the SGCM is smaller than that in the AOGCM.

It is shown that the AOGCM is capable of simulating these overall features of temporal structure of the observed SST variability. The SGCM, on the other hand, shows a quite different temporal structure, particularly in the decadal to interdecadal timescale. A difference in gradients of the spectral curve probably is related with differences in the feedback mechanism on the SST variability.

3.1.2 Spatial Structure of the Leading Mode

We examine the overall spatial pattern of the dominant SST variabilities in the decadal to interdecadal timescale. The leading EOFs of the decadal to interdecadal SST variations (hereafter SST-1s) are shown in Fig. 3-2. In order to isolate the variations of the decadal to interdecadal timescale, the annual mean SST variations are decomposed with harmonic analysis, and reconstructed with a spectral window which covers periods of 8 years and longer. It is considered that the observed SST variability may be affected by external thermal forcing (i.e., CO_2 induced warming). The models also have small linear

trend in their global mean SST. Linear trends are removed in order to reduce components affected by these warming or model drift, though the observed spectrum could still be affected by the other external forcings; volcano eruptions, changes in sulfate loading and so on.

The basin-wide pattern for the observed SST-1 (Fig. 3-2a) shows positive sign in the central-eastern part of the tropical and subtropical Pacific Ocean and regions along the coast of Americas, and negative sign in the central-western part of the midlatitude in the both hemisphere. This spatial pattern is similar to that for the interdecadal SST shift occurred in mid 1970's (see Nitta and Yamada, 1989).

Figure 3-2b shows the SST-1 for the AOGCM. Similarity of the basin-wide patterns between observation and AOGCM is notable. It has a wedge-shaped signal through the tropics and subtropics as shown in the observed SST-1. The negative SST anomaly in the central North Pacific is also well simulated.

The maximum variation in the SST-1 for the AOGCM is located around the date line of the equatorial Pacific, whereas the observation does not have strong variation on the equator. We consider this is related to a bias in the model climatology as follows. The model SST anomaly shifts far westward in the mature stage of the El Niño (Yukimoto et al. 1996), while the observed El Niño has a maximum anomaly in the eastern equatorial Pacific. In the model climatology, easterly wind on the equator extends to the western Pacific and the maximum zonal gradient of the SST shifts westward. These climatological biases probably affect variability in the atmospheric convective activity that is sensitive to the SST variation in the west of the date line where the SST is higher than about 27°C.

Location of the negative maximum in the North Pacific also shifts westward for the AOGCM compared with the observed one. This may be related to westward shift of the equatorial signal, if it is assumed that the SST variation in the North Pacific is caused by atmospheric circulation changes with teleconnection from the tropical Pacific. The location of the trough of the atmospheric stationary wave shifts westward in the AGCM. This atmospheric bias in the model may also be related to the westward shift of location of the midlatitude variability.

We can notice resemblance of the basin-wide patterns of the SST-1 between AOGCM (Fig. 3-2b) and SGCM (Fig. 3-2c). There is a subtle similarity of the wedge shaped patterns with their apex at the western equatorial Pacific and their 'robe' in the eastern subtropics and midlatitude. However, a negative signal in the midlatitude North Pacific shifts further westward. The pattern in the northern tropics is zonally elongated and is not very significant. The SGCM tropical signal is extremely concentrated to the equator and zonally elongated. It should be reminded that the SGCM has no oceanic dynamical mechanism for

El Niño. Temperature anomalies are not carried and/or damped by oceanic currents and waves, and there is no change in Ekman pumping even if the wind stress changed. Differences between the SST variation patterns are considered associated with these factors.

Spatial patterns of the first SST EOFs for the ENSO timescale (2-7 year periods) are shown in Fig. 3-3. Comparison of the spatial patterns between the timescales of interdecadal and ENSO is suggestive for discussion in later. Both patterns for observation and AOGCM show wedge-shaped patterns similar to those for the interdecadal timescale (Fig. 3-2a, b). The interdecadal variations in the tropical Pacific are not so concentrated to the equator, while there are strongly concentrated variations along the equator for the ENSO timescale. It is noted that the interdecadal variations have relatively larger amplitude in the far off equator of the 'robes' of the wedge shape. It is also noted that the interdecadal signals in the central North Pacific is located further east, in comparison with the ENSO timescale.

3.1.3 Spatial Structure of the Second Mode

Spatial patterns of the second EOFs of the interdecadal SSTs (hereafter SST-2s) are shown in Fig. 3-4. The observed SST-2 shows a dominant variation in the midlatitude North Pacific with an oval shaped pattern with east-west axis along the Kuroshio Extension. Similar spatial pattern is also shown by an EOF as second mode for an SST data that contains interannual variation (e.g., Deser and Blackmon, 1995), though there are some differences in the tropical region. The variation in the tropical Pacific and the South Pacific for this mode appears to have smaller significance compared with the variation around the Kuroshio Extension region.

For the AOGCM, the SST-2 also shows a dominant variation in the midlatitude North Pacific as for the observation. Variability in the tropical Pacific and South Pacific is very small and its statistical significance is low as well as in the observation. The major signal in the midlatitude North Pacific for the AOGCM is shifted northwestward and is confined in the western half region compared to the observed one. This probably be related to the model's biases that the simulated Kuroshio Extension current has rather diffuse meridional structure with its axis around 40°N, and the Aleutian Low is simulated far west, compared to the observations.

The SST-2 for SGCM also shows a major variation in the midlatitude North Pacific and much smaller variations in the tropics and the Southern Hemisphere, which are similar features with AOGCM. A dipole pattern is apparent for the SST-2 for SGCM. There is a positive signal through the eastern subtropical Pacific to western tropical Pacific, as a counter part against a negative signal in the central North Pacific. This feature is also seen

in the SST-2 pattern for the AOGCM, though its southeastern side signal (confined around Hawaii) is very weak and not significant. Such dipole pattern is not seen in the observed SST-2. However, in an aspect that the most dominant SST variability appears in the midlatitude North Pacific, the SST-2s have a common spatial feature between the observation and the models.

3.1.4 Temporal Structure of the Principal Modes

For both the observation and the AOGCM, temporal coefficients of the SST-2 (Fig. 3-4) appear to have longer timescale than that of the SST-1s (Fig. 3-2). In order to investigate detailed temporal structure of these SST variabilities, power spectra of the temporal coefficients of the EOFs are examined (Fig. 3-5). Recall that the EOFs are pre-filtered as mentioned above. The observed SST-1 (Fig. 3-5a) has two spectral peaks around 13 years and 23 years. It is most dominant over a broad spectral band from decadal to interdecadal (~ 30 years), in contrast with other modes. It is found that the SST-2 reveals red spectral feature and is more dominant than the SST-1 in timescales longer than 40 years.

The spectrum of the AOGCM SST-1 (Fig. 3-5b) has a maximum around 20 year period and large power over the broad spectral band between 9 years and 30 years. The SST-2 for AOGCM shows rather red spectral characteristic, although the observed one shows stronger red property. There is a clear contrast of the spectra between SST-1 and SST-2; the former indicates dominant variability in decadal-interdecadal timescale, while the latter indicates dominant variability in longer timescales. This contrast in the spectra is commonly seen in both the observation and AOGCM. It is shown that the AOGCM well simulates the overall spectral properties of the dominant modes of the observed SST.

For the SGCM (Fig. 3-5c), the SST-1 has a very large spectral peak around 10 year period and a distinct spectral gap around 20 year period. The second mode for SGCM reveals white spectral property in decadal to interdecadal timescales. As a whole, the overall spectral property for SGCM is quite different from those for the observation and AOGCM. The SGCM also fails to reproduce the contrast of the spectral property between SST-1 and SST-2.

3.2 Model ENSO

The ENSO-like variability simulated in the MRI-CGCM1 is overviewed. Figure 3-6 shows time series of the simulated SST monthly anomaly at the equatorial central Pacific region(160˚E-160˚W, 6˚S-6˚N), and the southern oscillation index (SOI) defined as the sea level pressure difference between Tahiti and Darwin. Both the SST anomaly and the SOI show significant interannual oscillations with dominant periods of 3 to 6 years. The

magnitude of the SST anomaly is about twice larger than that of previous coupled models (Philander et al. 1992, Nagai et al. 1992, Latif et al. 1993), though it is still small compared to the observed peak value of 3°C. Our model has maximum variability of the SST around the date line, while it has smaller amplitude in NINO3 region (150˚W-90˚W, 5˚S-5˚N) of the east-central Pacific (peak value of 0.9°C). This is probably related to westward shift of the largest zonal gradient of the equatorial SST in the model climatology. Time series of the model SOI also show interannual variation, which has negative correlation (–0.72) with the SST anomaly. This correlation is comparable with that for the observed ENSO.

There are prominent 10 warm events and 8 cold events during the 70 years model integration. Common features of these events are typically seen in a warm event in the 10th year of the integration.

Figure 3-7 shows the time-longitude plots of anomalies for SST, zonal wind stress, vertical averaged temperature (VAT) along the equator, respectively, and the off-equatorial VAT along 8°N. These variables are plotted for the year 9 to year 13. The VAT represents heat content of the upper 300 *m* of the ocean.

Prior to the warm event, the VAT along the equator increases in the western Pacific and decreases at the east-central Pacific. This is equivalent to a deepening of the thermocline at the western boundary and a shoaling of it at the east-central Pacific. During this period, large easterly wind anomaly in the central Pacific is sustaining. The VAT positive anomaly in the equatorial western boundary begins to propagate eastward in January of year 10, and reaches the eastern boundary in March of year 10 (Fig. 3-7c). It takes about 2-3 months for the signal to cross the basin. The propagation speed is comparable with that of the first equatorial Kelvin mode. Beginning of the signal propagation is seasonally phase-locked to boreal winter in most of the model events. It can be seen that several pulses of VAT anomalies (which follow impulsive westerly wind anomalies in the central Pacific) propagate successively for more than one year, and subsequently, the positive VAT anomaly in the western Pacific disappears.

Warming of the SST starts at the east-central Pacific when the first VAT anomaly arrive at the eastern Pacific. The SST warming which is initiated at the eastern Pacific extends westward accompanying the westerly wind stress anomaly (Fig. 3-7a and b). In the mature stage of the model warm event, SST warming is enhanced around the date line, and westerly wind stress anomaly becomes dominant in the central Pacific. To the west of the date line, at the mature stage of the SST warming, significant positive downward heat flux anomaly at the ocean surface (not shown here) correspond with the SST warming.

It is clearly seen that westerly wind stress anomalies in the central equatorial Pacific generate negative VAT signals off the equator (Fig. 3-7d) by weakening of the Ekman

convergence there. These negative VAT signals propagate westward and reach at the western boundary. It takes about half a year for the signals to cross the half of the basin. Its propagation speed approximately corresponds to the group velocity of an oceanic Rossby wave along this latitude. The propagation of this signal off the equator contributes to the decrease of ocean heat content in the western Pacific. After the decrease of ocean heat content in the western Pacific, negative signal propagates eastward, in turn (at the beginning of year 12). Variation similar to what is mentioned above is repeated with the opposite sign as the next La Niña phase. This cycle in the model ENSO is consistent with the delayed-oscillator which has been proposed by Schopf and Suarez (1988) and Battisti and Hirst (1989), and argued by Nagai et al. (1992) with their CGCM.

3.3 Interannual Variabilities in the Mid-high Latitudes

There are spectral peaks at periods around 3.5-4 years, 6 years, 8-9 years and 13-20 years for the tropical Pacific SST (Fig. 3-1). Since a gap in the spectra is recognized at the period of 12 years, we define (1) variation with the 2 to 12 years' period as (model's) ENSO time-scale variation and (2) variation with the period longer than 12 years as interdecadal time-scale variation. We separated these variations by applying time filter for the annual mean data set. Then, empirical orthogonal function (EOF) analyses are made for those time filtered data of the Indo-Pacific region (region A). Calculation of the EOFs are based on variance-covariance matrix in order to see relative magnitude of the variations. We focus on the ENSO time-scale variation of the Pacific in the mid-high latitudes.

Figure 3-8 shows EOFs of the first mode (EOF1) for the ENSO time-scale variation of the simulated (a) SST and (b) wind stress. The EOF1 of the SST and the wind stress accounts for 30.8% and 20.4% of all variance in this time scale. The spatial pattern of the EOF1 of SST indicates that there is an intensive positive signal in the central equatorial Pacific where the model ENSO shows maximum SST variations. Notable peaks in the temporal coefficients coincide with years of the prominent events in the equatorial SST (Fig. 3-6a). Accordingly, it is considered that this EOF1 mode represents variation in the equatorial Pacific region associated with the model ENSO. In the mid-high latitudes, the EOF1 of SST shows positive in the eastern Pacific, especially between Hawaii and the west off California and negative in the central North Pacific and the west-central South Pacific. This wedge shaped pattern is typically seen in the EOF1 of the observed SST in the same time scale (not shown).

The EOF1 of the wind stress also corresponds to the variation associated with the model ENSO, since the temporal coefficients correlates well with that of the EOF1 of the SST (r=0.82). During the maximum phase of the equatorial SST, large westerly wind stress

anomaly in the western equatorial Pacific and convergence of anomalous wind stress from the equator (around 150˚W) to 120˚W-12˚S in the South Pacific, are clearly seen. This feature of the wind stress anomaly is well documented in the observed El Niño (e.g., Rasmusson and Carpenter, 1982). In the central North Pacific, there is a dominant westerly wind anomaly and a cyclonic wind anomaly in its northern side which corresponds to the intensification of the Aleutian low in winter. The eastern North Pacific around Hawaii is also dominated by the westerly wind stress anomaly (Fig. 3-8b). This results in a weakened north-easterly trade and a suppression of evaporation which contribute to warming of the SST there. Along the coast of Canada and Alaska, a strong southerly wind anomaly, which leads warm air advection, is expected to raise the SST there as is seen in the EOF1 of SST (Fig. 3-8a). Associated variation is also recognized in the 500 *hPa* geopotential height (Z500). Correlation map between Z500 of northern winter (December to February) and the time coefficient of the EOF1 of the SST for the ENSO time-scale (Fig. 3-9a) shows the largest positive correlation in the tropical Pacific and marked negative correlation in the North Pacific with a center at around 170˚E, 45˚N. Another positive correlation is seen in the North America centered at around the western part of Canada. These features are seen in similar correlation map for the observation (Fig. 3-9b). These PNA-like teleconnection originate from the equatorial Pacific as a midlatitude atmospheric response of Northern Hemisphere to the warm SST anomaly in the tropics (Horel and Wallace, 1981).

In order to examine whether the SST anomaly is forced by the surface heat flux, or the surface heat flux is controlled by the SST, for the ENSO time-scale, we calculate correlation between temporal coefficient of the EOF1 of the SST and total heat flux (including radiative flux) at the ocean surface (Fig. 3-10a). Except for the equatorial region, the heat flux anomaly is positive downward where the SST anomaly is positive, and vice versa. It implies that the extratropical SST is forced by the surface heat flux variation in the ENSO time-scale. Next, in order to see whether the surface heat flux anomaly is a dominant factor for the extratropical SST change in terms of heat budget, correlation between the SST tendency anomaly and the surface heat flux anomaly for the northern winter (December to February) is examined (Fig. 3-10b). The seasonal mean SST tendency is defined from the raw monthly mean data. It is found that the correlation is higher than 0.6 in a large part of the midlatitude of the Pacific. Area averaged correlation is 0.78 for the central North Pacific (160˚E-160˚W, 30˚N-42˚N) and 0.91 for the region east of Hawaii (160˚W-120˚W, 14˚N-26˚N), where large values appeared in the spatial EOF1 of SST (Fig. 3-8a). Correlation of the midlatitude in summer (not shown here) has qualitatively similar feature with that in winter, and has slightly smaller value. Although the correlation north of 40˚N in winter is low (Fig. 3-10b), the correlation north of 40˚N in summer is close to that

in the midlatitudes. Analysis of the SST heat budget shows that the heat flux anomaly accounts for large part of the SST tendency anomaly in the midlatitude North Pacific. The SST variation in these regions is, therefore, mainly controlled by the surface heat flux variation in the ENSO time-scale.

The ocean subsurface variation in relation with the model ENSO is examined for the whole Pacific. The vertical averaged temperature (VAT) over the upper 300 *m* of the ocean is used as an indicator of the ocean subsurface variation, and the temporal coefficient of EOF1 of the SST for the ENSO time-scale is chosen as an indicator of the model ENSO. Figure 3-11 shows lagged regressions of the VAT from the temporal coefficient of EOF1 of the SST.

In the tropical Pacific, the VAT variation associated with the model ENSO is apparent. Prior to the maximum phase of the model ENSO (lag = –1, Fig. 3-11a) positive equatorial signal is notable, suggesting a propagation of an equatorial Kelvin wave. In the following 2 years, it appears that a negative signal off the equator propagates westward and reaches the western boundary (Fig. 3-11b,c).

In the midlatitude of the North Pacific, significant variation is found to be associated with the model ENSO. Negative anomalies appear in the central North Pacific (A in Fig. 3-11b) and the Kuroshio extension region (B in Fig. 3-11b) at the maximum phase of the model ENSO. The negative anomalies (A and B) develop and are combined one year later (C in Fig. 3-11c). Afterwards, the southern portion of the developed anomaly (C) migrates westward and reaches the western Pacific (Fig. 3-11d,e). A similar signal with the opposite sign to the signal A is seen in lag=3 years (D in Fig. 3-11e), which has migrated from the offshore of California. Propagation of these signals and their enhancement in the central North Pacific are evident in the vertical zonal cross section along 32˚N for similar lag regression analyses (Fig. 3-12a-e). It is analyzed that the horizontal pattern of the shallow signals is consistent with heating and cooling region shown in Fig. 3-10a. A warming in the eastern part and a cooling in the central part of the surface layer (~100 *m*) are separated from the deeper signals in the subsurface (Fig. 3-12a,b). Westward propagation of the subsurface signals (200 *m* ~ 500 *m* depth) is clearly seen: for example, a negative signal around 150˚W at lag = –1 year migrates to 160˚E during the following 4 years. The propagation speed (~ 5 $cm\ s^{-1}$) is almost comparable to the group velocity of oceanic first baroclinic Rossby wave at this latitude in the model.

After a year from the maximum phase (lag = 1), cooling in the central Pacific extends beyond 800 *m* depth (Fig. 3-12b,c). Location of the negative subsurface signal around 160˚W corresponds to that of the large positive vorticity of the wind stress anomaly (Fig. 3-8b). It is considered, therefore, that the development of this subsurface signal is s dynamical

response to the wind forcing through the Ekman pumping.

3.4 Summary and Discussion

Interannual and interdecadal time-scale variations in the Pacific region are investigated with the analysis of a 150-year integration of the MRI-CGCM1. It is shown that the coupled model with a dynamical ocean model (CGCM) reproduces basin-wide patterns of the principal SST variability similar to the observed one. Temporal structures of the SST variability also agree well between the observation and the CGCM. On the other hand, SGCM (a slab ocean model coupled to the same atmospheric component as in the CGCM) fails to simulate the observed temporal structure. It is suggested, therefore, that the timescale of the coupled variability is associated with dynamical processes in the ocean.

The model reveals interannual variability in the tropical Pacific, which has several typical characteristics of the observed ENSO. The oceanic heat, which is piled up in the equatorial western Pacific preceding the warm event, propagates eastward as an equatorial Kelvin wave and brings about the warming of the SST in the eastern Pacific. In the model events, however, there is no indication of eastward evolution of SST and wind stress coupled with Kelvin wave propagation (Philander et al., 1984). The SST warming spreads westward, accompanied by the westward propagation of the westerly wind stress anomaly. This stage reminds us an SST mode (Neelin, 1991) which behaves as a wind stress-upwelling feedback. Similar behavior of the SST signals with global coupled models were reported by Meehl (1990) and Lau et al. (1992). At the mature stage, the SST warming develops around the date line with increased downward surface heat flux. The model shows that the westward propagation of the oceanic heat content off the equator contributes to the pile-up of ocean heat content in the western Pacific to prepare the next event. This cycle implies the delayed-oscillator mechanism (Schopf and Suarez, 1988; Battisti and Hirst, 1989) of the model ENSO.

Basin scale feature of the principal SST variation for the ENSO time-scale (representing the model ENSO in the tropics) shows negative correlation in the central North Pacific against the tropical SST, and it is similar to that of the observed one. The associated variation of the atmosphere indicates the intensification of the Aleutian low and the PNA-like teleconnection pattern as a response to the tropical warm SST anomaly. It is shown that the surface heat flux associated with atmospheric circulation changes is a dominant factor for the midlatitude SST variation in the North Pacific. Tokioka et al. (1993) argued that the enhanced Aleutian low in winter contributes to cooling in the central North Pacific ocean by increase of evaporation and southward cold water advection by the Ekman transport in a coupled GCM. Miller (1992) also reported the similar result with a simple

coupled model. Our result is consistent with those studies.

It is shown that the ENSO time-scale variability of the midlatitude ocean consists of the westward propagation of the subsurface temperature signal and the temperature variation within the shallow mixed layer forced by atmospheric heat fluxes. The temporal evolution of the negative subsurface temperature anomaly may be explained as follows. The negative anomaly is apparently either originated by the last La Niña along the eastern coast of the North Pacific, or generated by the northerly wind anomaly along the Californian coast. This negative anomaly migrates westward as an oceanic Rossby wave, while the next El Niño occurs. The wind forcing, as a result of atmospheric response to the El Niño, contributes to enhancing this signal through both surface cooling and positive vorticity input. Consequently, the negative anomaly is enhanced sufficiently to sustain its amplitude until it reaches the western Pacific. Thus, close time-scales of the model ENSO and the westward propagation of the midlatitude subsurface signal across the basin may enhance midlatitude oceanic variation in the ENSO timescale.

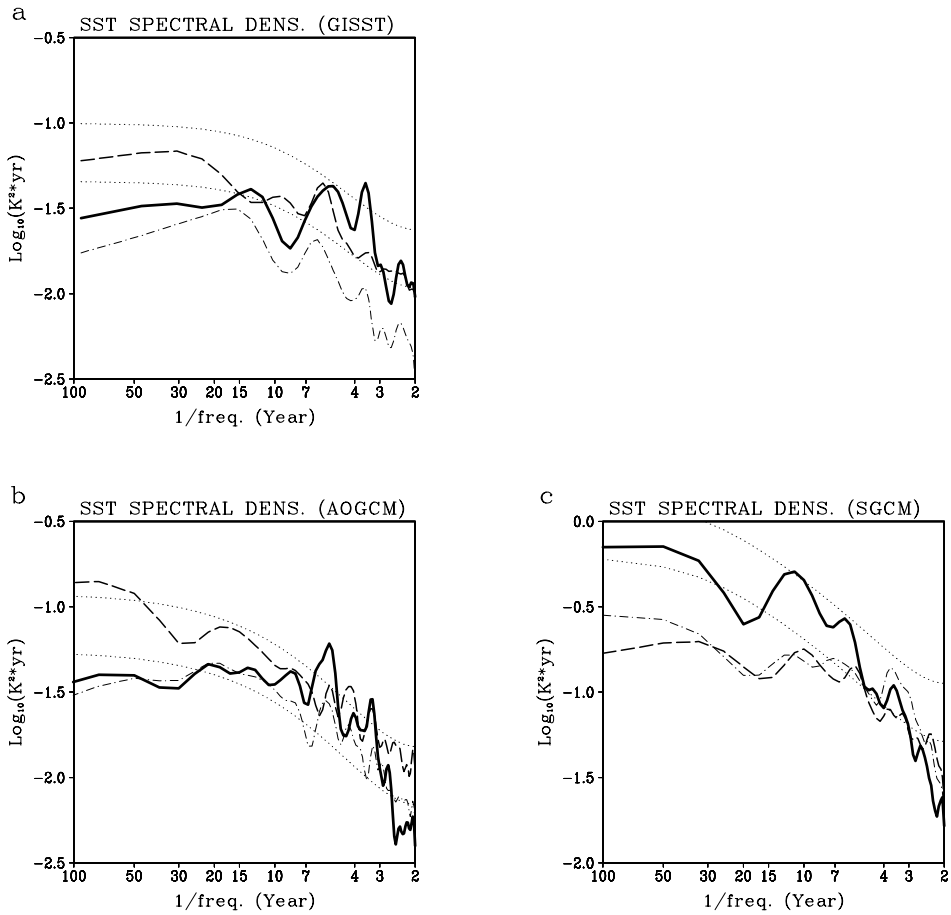

Figure 3-1 Temporal spectra of the SSTs for the (a) observation, (b) AOGCM and (c) SGCM. The spectra are calculated at each grid point and averaged over the North Pacific (150°E-90°W, 15°N-55°N; dashed curves) tropical Pacific (150°E-90°W, 10°S-10°N; solid curves) and the South Pacific (150°E-90°W, 35°S-15°S; dot-dashed curves), respectively. The values are common logarithm of the power density of temperature (unit is K^2). Thin dotted curves show red noise spectra by AR1 model fitted to the entire Pacific (150°E-90°W, 35°S-55°N) SST and its 95% confidence level. Differences of the confidence limit range between basins are very small and negligible.

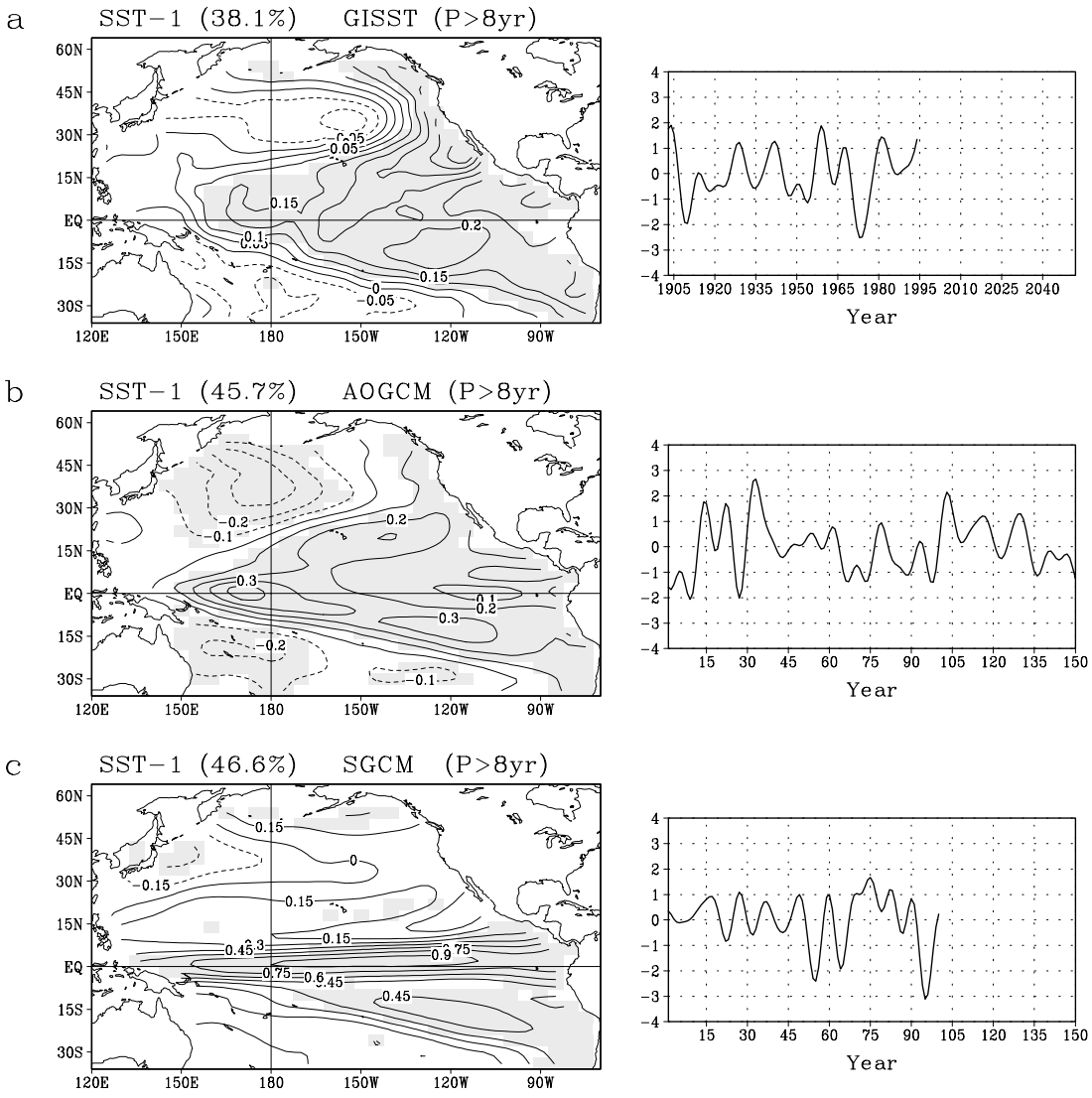

Figure 3-2 Spatial patterns (left panels) and temporal coefficients (right panels) for the leading modes of EOF of the interdecadal SST variations (period > 8 years) in the Pacific region (120°E-70°W, 34°S-60°N) for (a) observation, (b) AOGCM, and (c) SGCM. The EOFs are based on variance-covariance matrix. Values in the spatial patterns denote variance (unit is K^2). The temporal coefficients are normalized to have a unit standard deviation. Correlations significant at the 95% level are shaded.

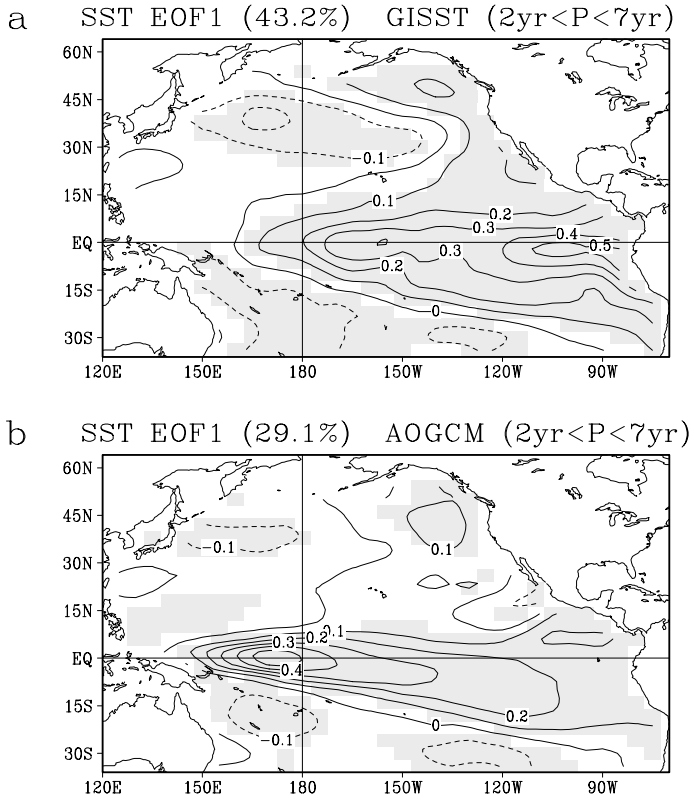

Figure 3-3 Spatial patterns of the leading EOF modes for the ENSO timescale (2-7 year periods) SST variations in the Pacific region (120°E-70°W, 34°S-60°N) for (a) observation and (b) AOGCM. The EOFs are based on variance-covariance matrix. The values in the spatial patterns denote variance (unit is K^2). The temporal coefficients are normalized to have unit standard deviation. Correlations significant at the 95% level are shaded.

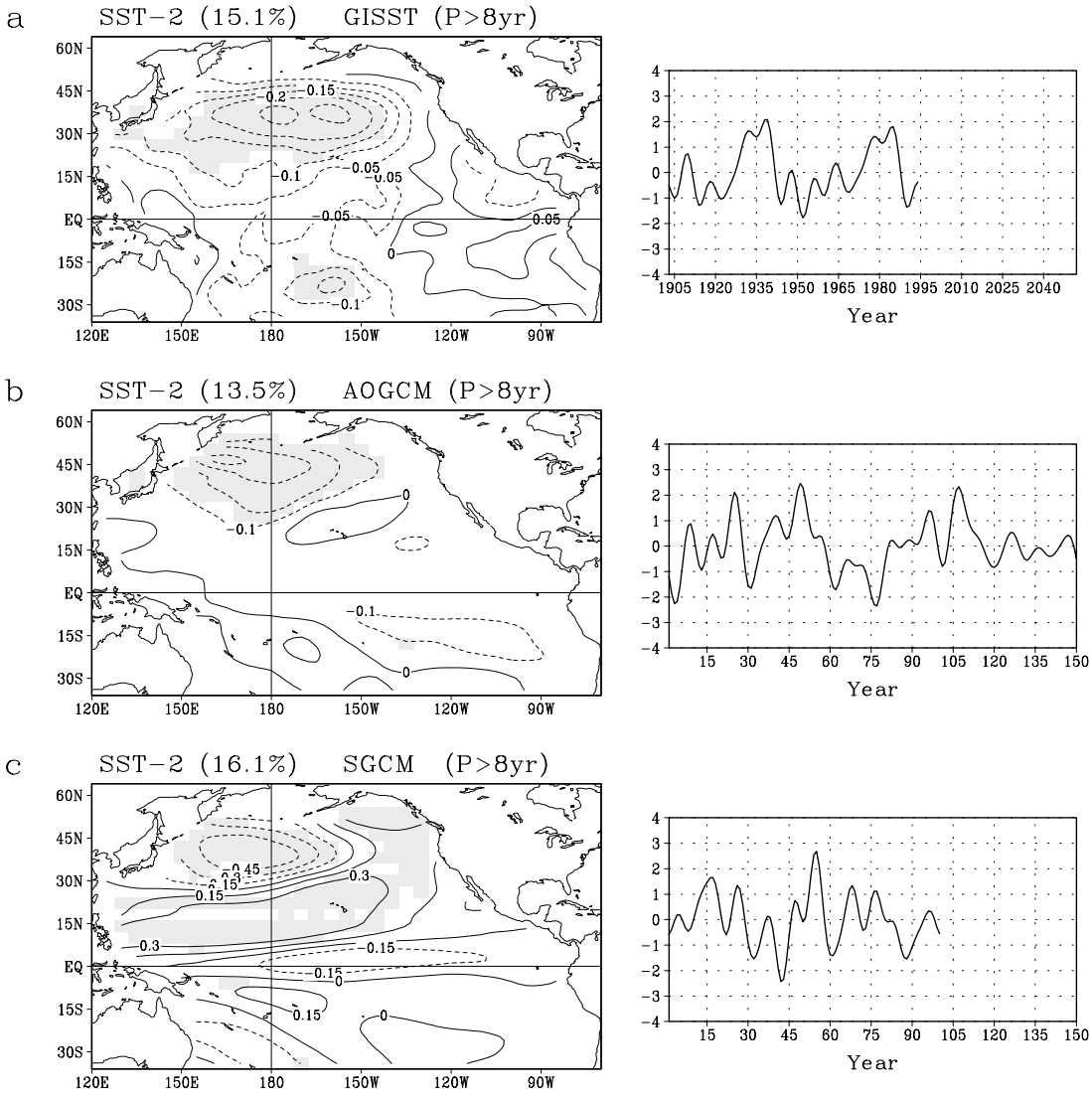

Figure 3-4 Same as Fig. 3-2 but for the second EOFs.

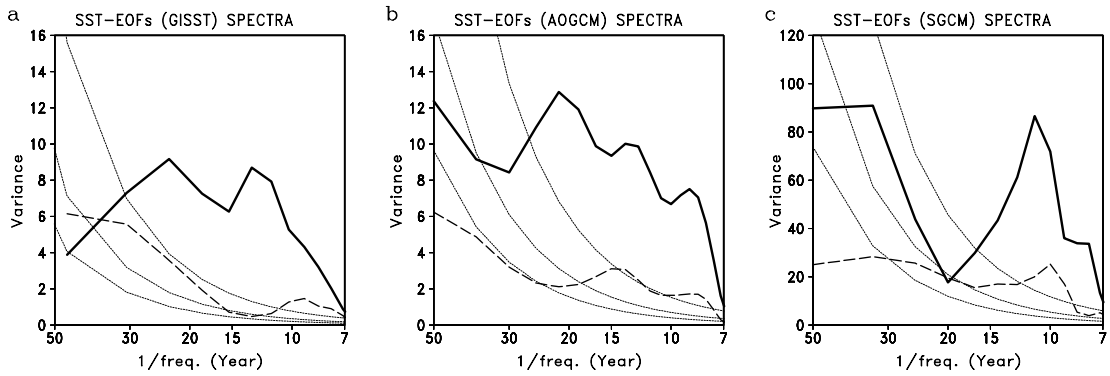

Figure 3-5 Power spectra of the temporal coefficients of the EOFs (first mode: solid curve, second mode: dashed curve) of the interdecadal SST variations for (a) observation, (b) AOGCM and (c) SGCM. The values in the abscissa are periods (years), and values in the ordinate are common logarithm of the power density (unit is relative). Thin dotted lines show red spectra by lag one auto-correlation fitted to spectra of the second mode and its confidence levels at 5% and 95%.

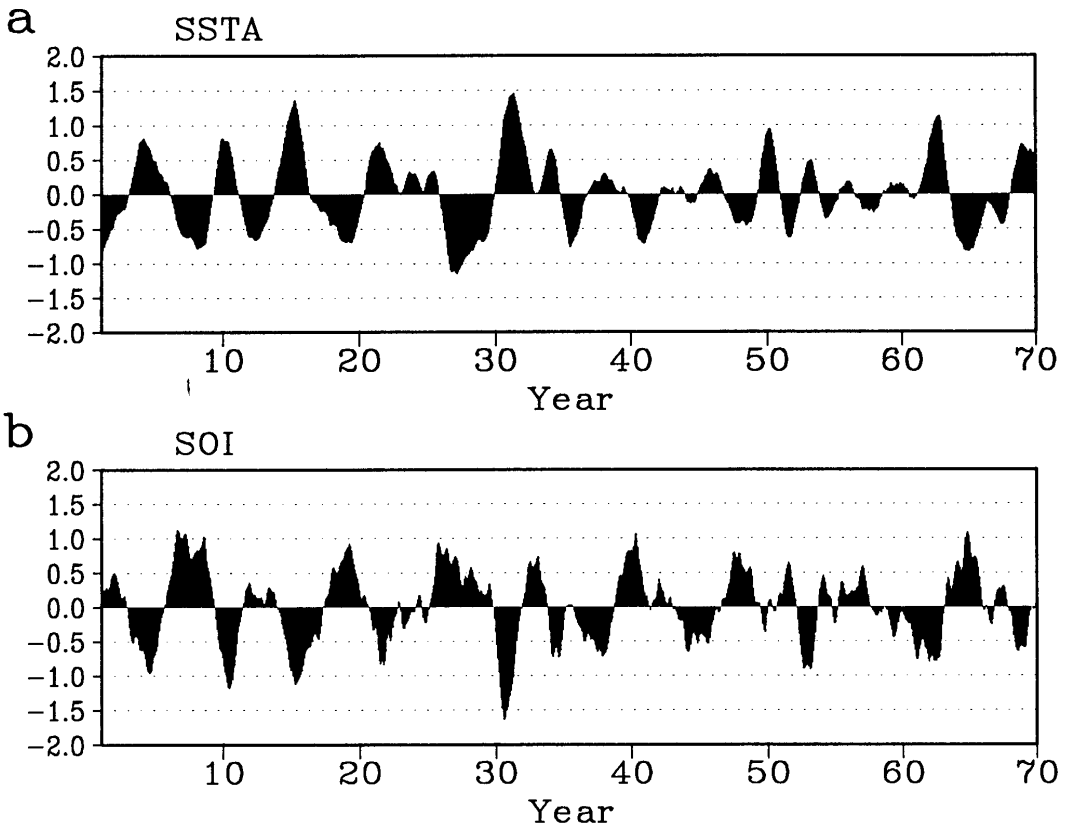

Figure 3-6 Time series of the simulated (a) SST anomaly in the central equatorial Pacific region (160°E-160°W, 6S-6N) and (b) SOI, for the 70 years model run. The values are 13 months running mean.

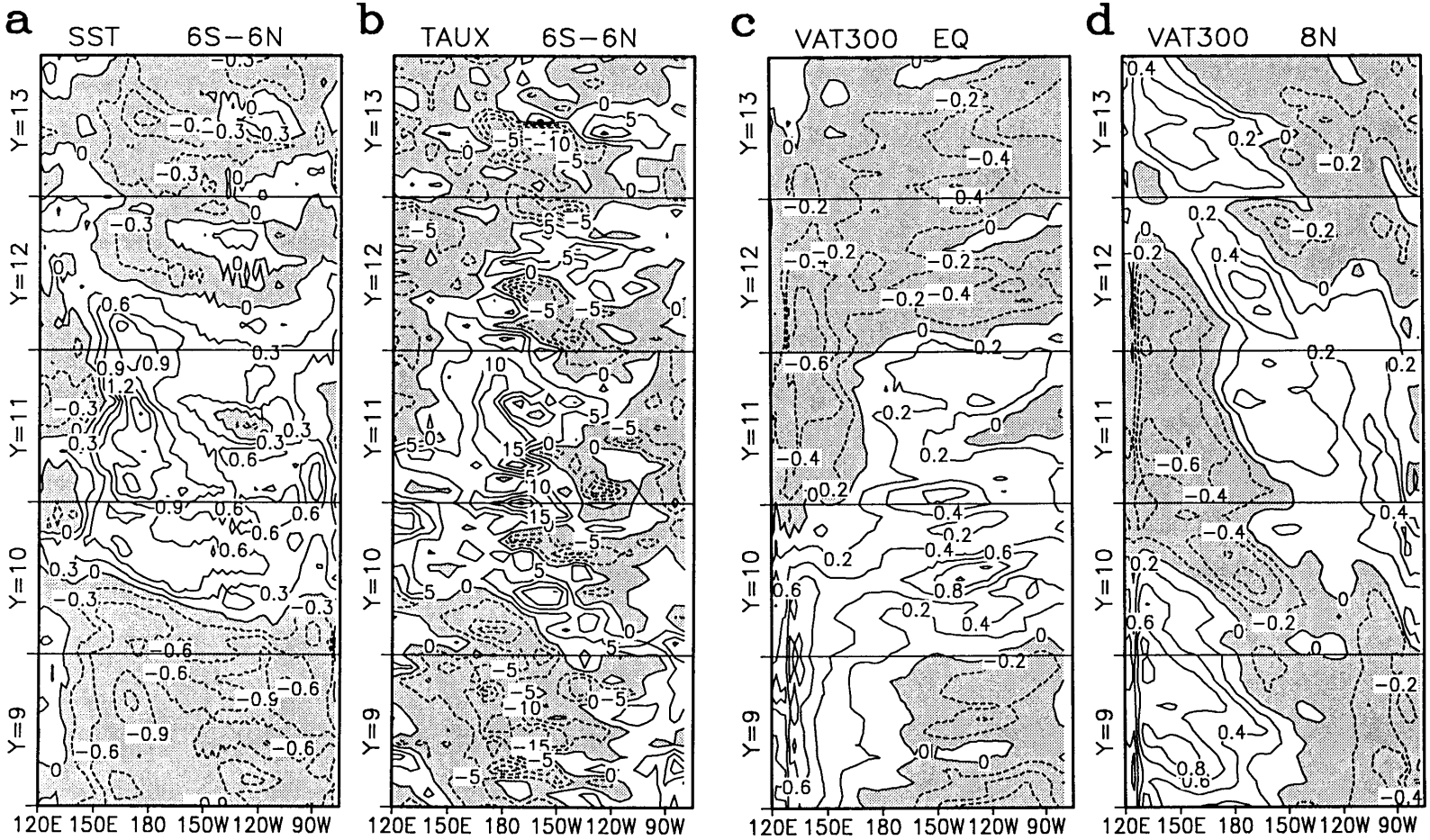

Figure 3-7 Longitude-time plot for the anomalies of (a) SST (average between 6°S and 6°N) , (b) zonal wind stress (average between 6°S and 6°N) , (c) VAT along the equator and (d) VAT along 8°N. Time covers year 9 to year 13 of the model run. Negative values are shaded. Contour intervals are (a) 0.3 °C, (b) 0.05 Nm^{-2}, (c) 0.2 °C and (d) 0.2 °C.

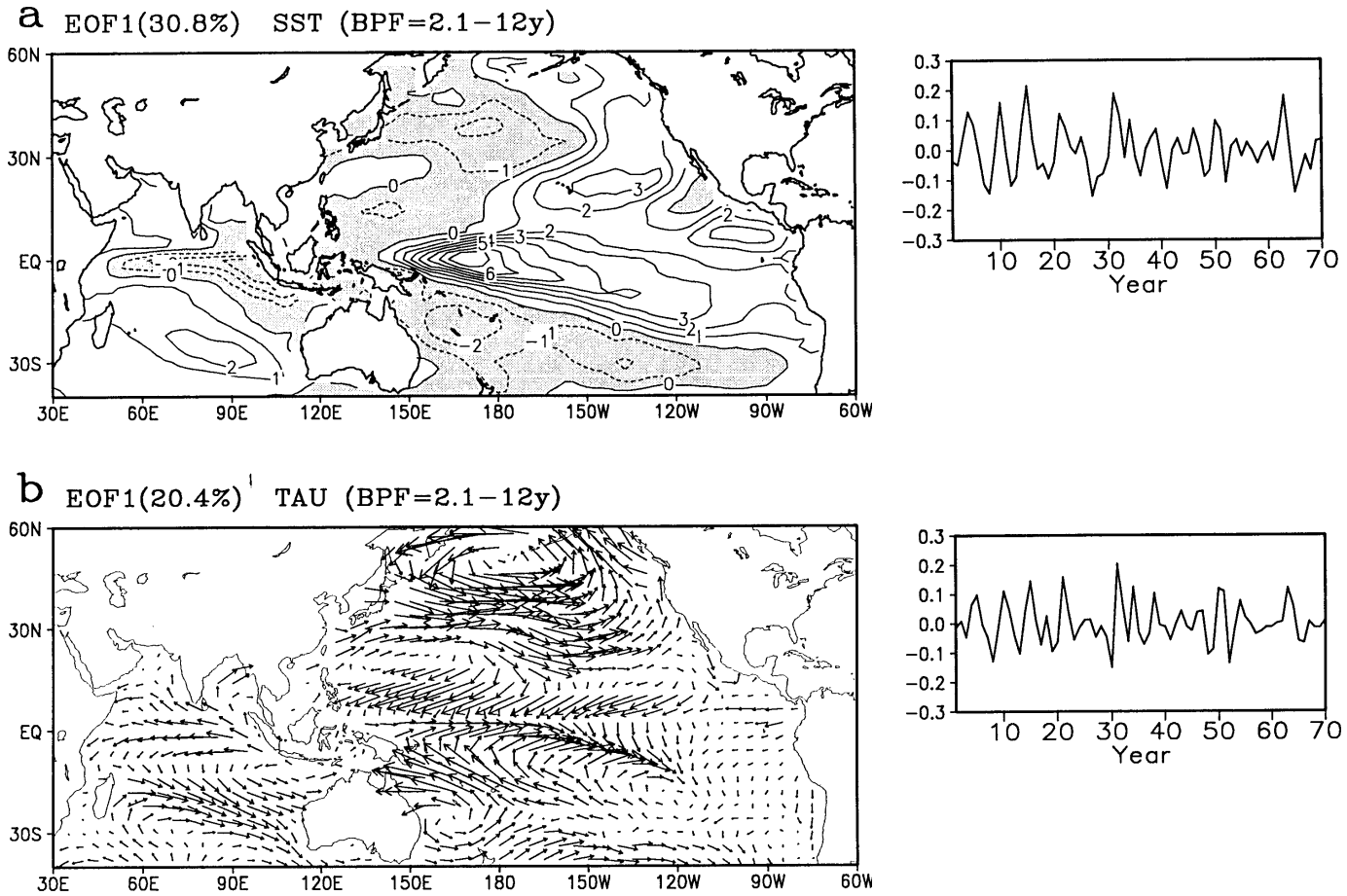

Figure 3-8 Eigenvectors and time coefficients of the first EOFs of simulated (a) SST and (b) wind stress for ENSO time-scale (2 - 12 years). Negative region is shaded in (a). The values of eigenvectors are in proportion to amplitude of variance, since EOFs are calculated for variance matrix.

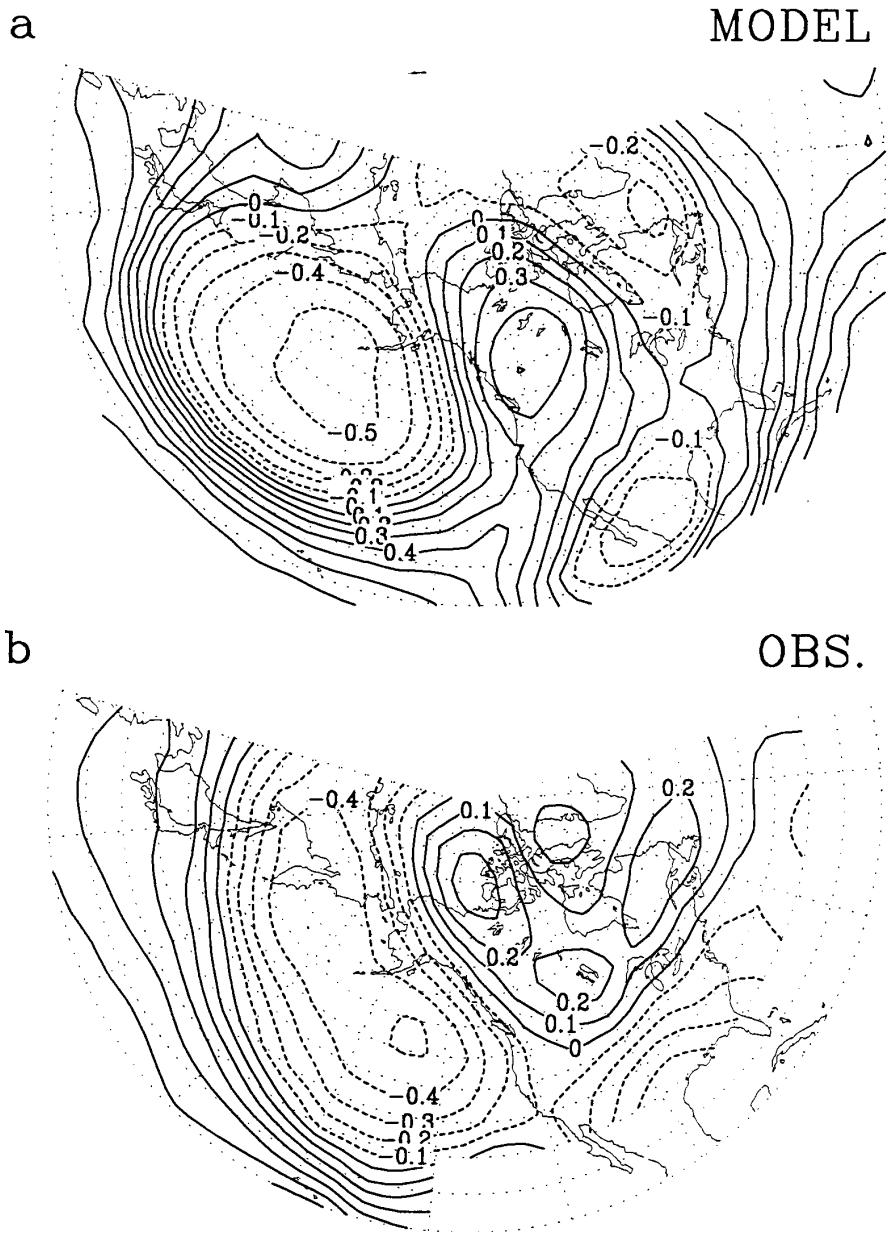

Figure 3-9 Correlation between boreal winter (December to February) Z500 and temporal coefficient of EOF1 of the SST for the ENSO time-scale, for (a) the model and (b) the observation, respectively. The observed correlations are calculated for the period 1946-1992.

a

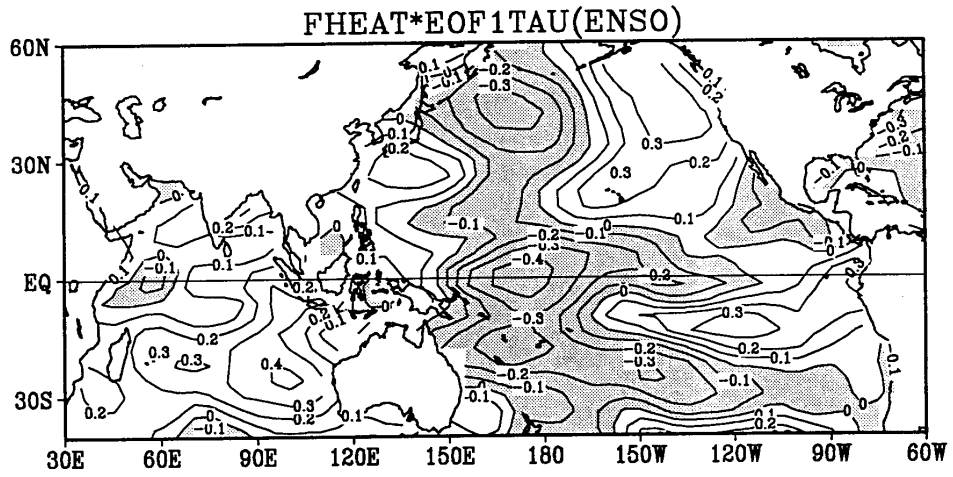

b

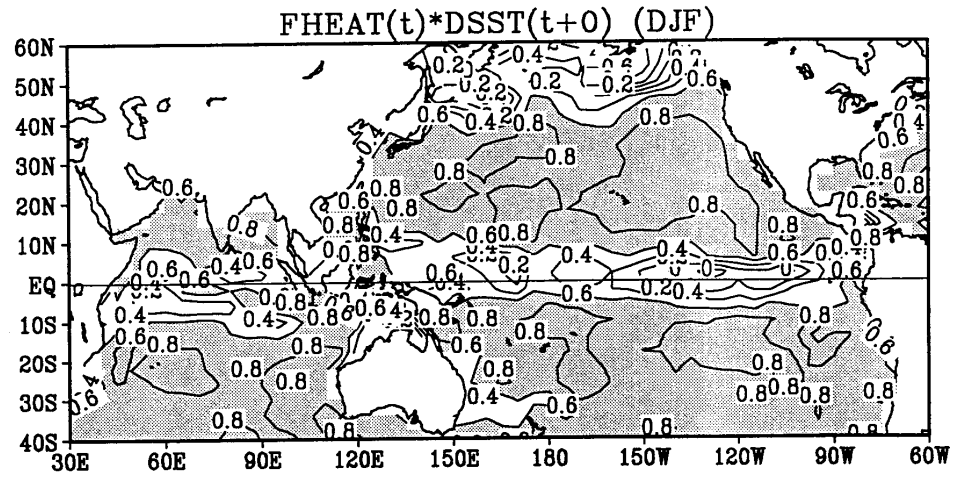

Figure 3-10 Distributions of (a) the correlation between downward heat flux (sensible+latent heat and net radiative flux) at the ocean surface and temporal coefficient of the first EOF of the SST for the ENSO time-scale (negative regions are shaded), and (b) the correlation between the SST tendency anomaly and the downward surface heat flux anomaly for the northern winter (December to January). The SST tendency is defined from the raw monthly mean data. High correlation (r>0.6) regions are shaded in (b).

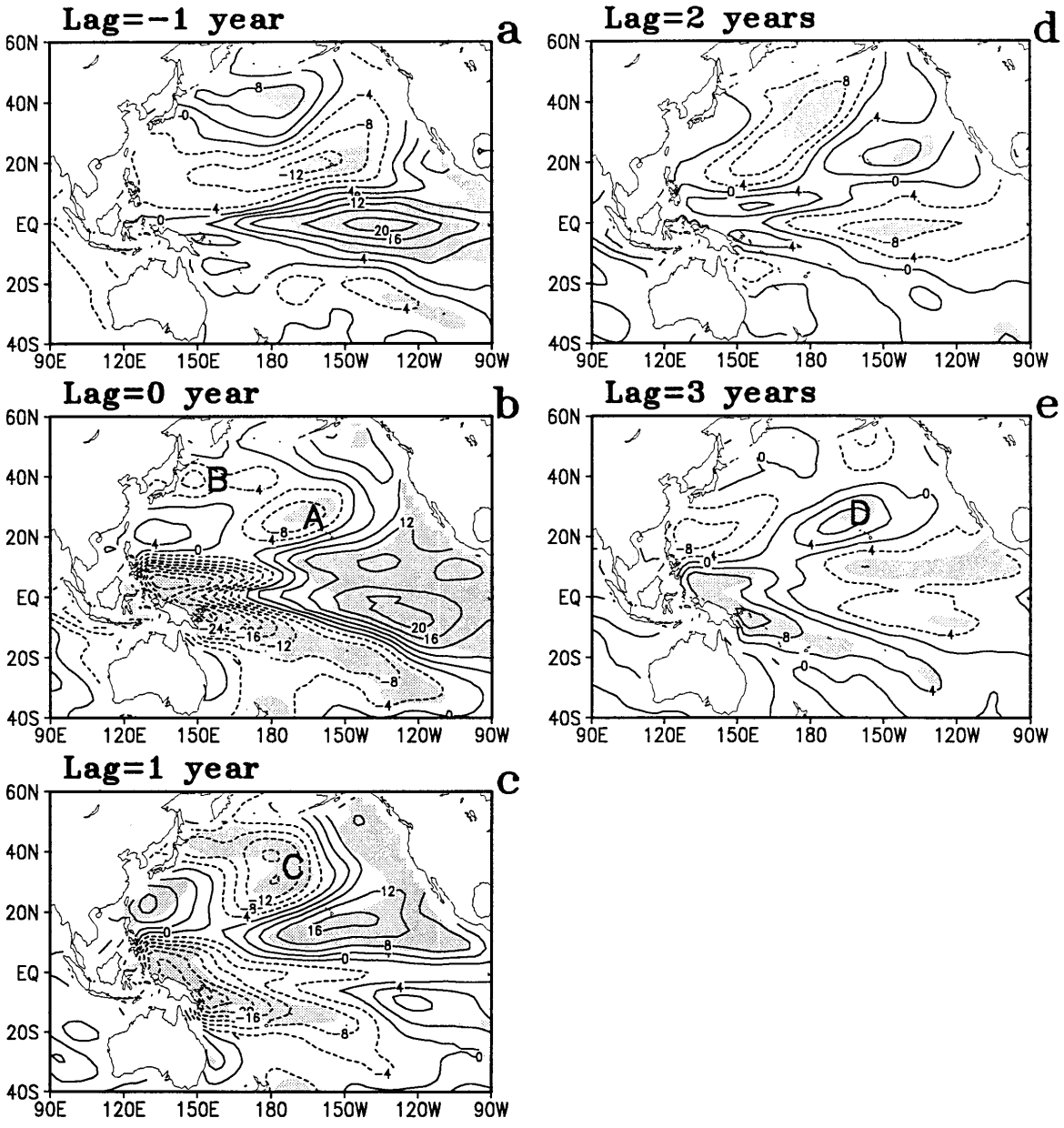

Figure 3-11 Lagged regressions of the VAT with the time coefficient of the EOF1 of SST for the ENSO time-scale. (a) lag=–1 year, (b) lag=0, (c) lag=1 year, (d) lag=2 years, (e) lag=3 years. High correlation ($|r| > 0.4$) is shown in shaded region. The units are relative.

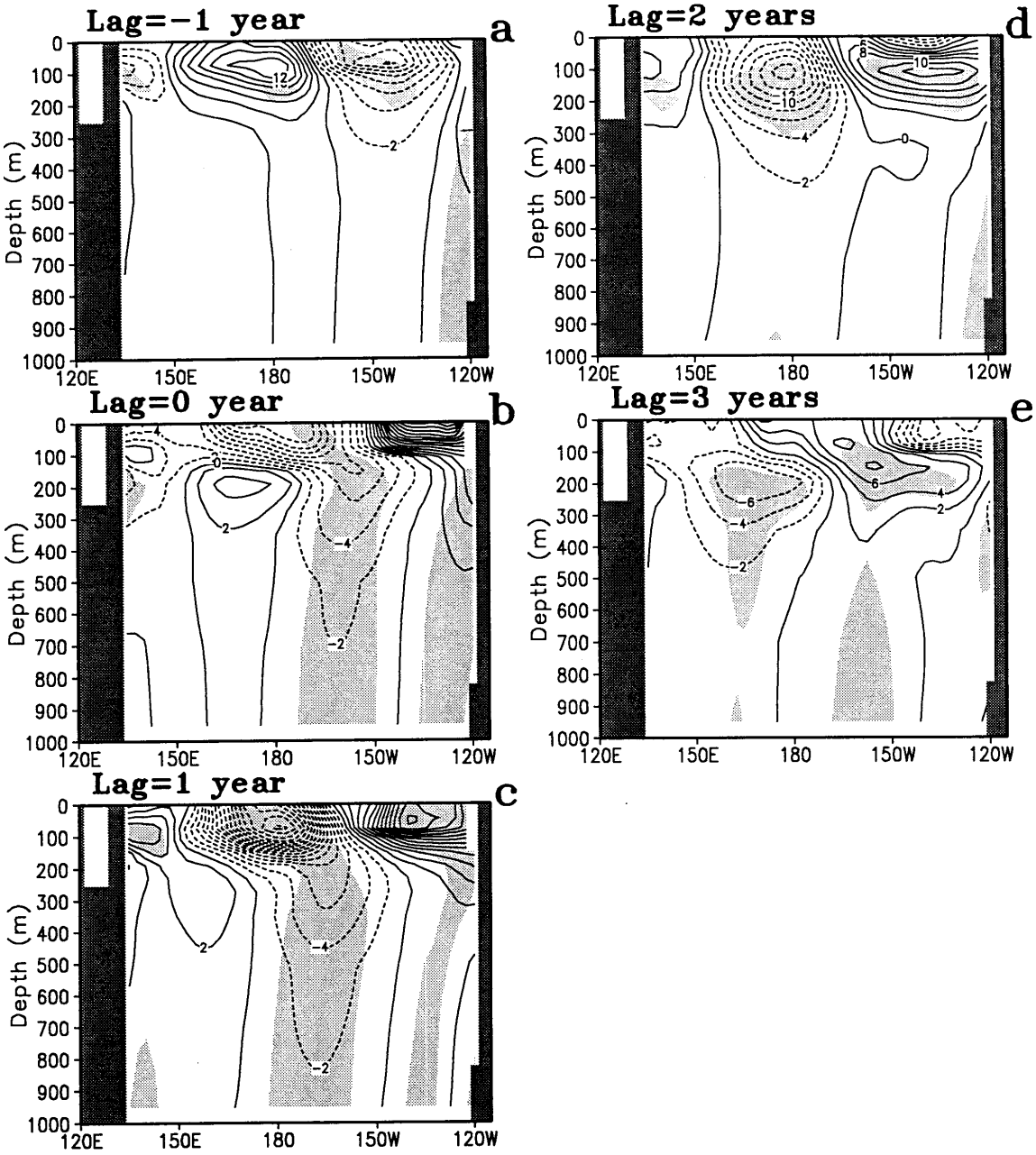

Figure 3-12 Lagged regressions of the ocean temperature in zonal-vertical cross section along 32°N with the time coefficient of the EOF1 of SST for the ENSO time-scale. (a) lag=–1 year, (b) lag=0, (c) lag=1 year, (d) lag=2 years, (e) lag=3 years. Units are relative. High correlation ($|r| > 0.4$) regions are shaded.

4 Decadal to Interdecadal Variability in the MRI-CGCM1

4.1 Interdecadal Variability in the Upper Ocean

In the previous section, it is shown that the MRI-CGCM1 well reproduces the spatial and temporal structure of the SST variability in the Pacific. The difference between AOGCM and SGCM in their spectral property suggests that the temporal structure of the variability is related to dynamical processes in the ocean. Since the variation of surface wind stress affects thermocline depth by its curl component, it is important to interpret the SST variations in conjunction with variations of the subsurface ocean temperature and surface wind stress. Spatial structure and its temporal evolution of the variability of the upper ocean heat content are analyzed with the vertically averaged temperature (VAT) of AOGCM. Temperature of the upper ocean is averaged between the surface and 600 *m* depth, so that averaged depth is taken to be enough to include a large part of the thermocline which was diffuse compared with the observed one (Fig. 2-4).

The temporal spectra of the VAT variation are shown in Fig. 4-1, for the tropical Pacific, the midlatitude North Pacific and the midlatitude South Pacific, respectively. The spectrum of the tropical VAT shows similar characteristic with that of the SST; red spectrum with several distinct peaks in the ENSO timescale and relatively white spectrum and less distinct peak in the longer timescale. Almost all the peaks are consistent with those for the SST (Fig. 3-1b) over the entire timescales from ENSO to interdecadal. For example, both SST and VAT in the tropical Pacific have distinct spectral peaks at 3.3 year and 5.4 year period and a smaller peak at 8-year period. A faint spectral peak around 15 - 20 year periods for the North Pacific also seems to correspond to that in the north Pacific SST, though it is not statistically significant. The variability of the VAT in the North Pacific is characterized by red spectrum in the decadal to interdecadal timescales, and the variability becomes much larger than that in the tropical and south Pacific for the periods longer than 30 years. This feature is consistent with the SST-2, which has dominant variability in the midlatitude North Pacific (Fig. 3-4b) and has red spectral characteristic (Fig. 3-5b).

It is shown that the spectra of the VAT are consistent with those of the SST, however, it does not mean that SST and VAT change without time lags. Temporal evolution of the spatial structure of variations should be considered with several year lags, since it takes longer than a decade for the ocean in the mid-high latitude to adjust to a change of wind forcing.

In order to examine temporal evolution of the VAT, a complex EOF (CEOF) analysis is applied to the band-pass filtered VAT data. Complex EOF analysis is one of the most

convenient way to extract variations with phase propagation. From regression on its principal components, associated variation with a phase lag/lead (for instance, a forcing that leads 90° for the driving variation) can be obtained. Ordinary EOF is not appropriate for such lag regression analysis when the variation has broad spectral band or red spectrum. We used band-pass filter with 8 - 50 year spectral window for this analysis. We examined several cases with different filter bands, and found that including periods longer than 50 years makes degree of freedom very small and makes it difficult to discuss its temporal evolution statistically. We consider the variability longer than 50 years should be discussed in another study with much longer model integration.

Temporal evolution of the reconstructed spatial pattern of the first CEOF mode (hereafter VAT-1) is shown in Fig. 4-2. This mode accounts for 42.5% of the total variance of the filtered VAT. The temporal coefficient of this mode has spectral peaks around 10 year and 20 year periods (Fig. 4-3), and shows spectral curve similar with that for the SST-1 (Fig. 3-5b) except for periods longer than 30 years. This spectral feature is robust when the pre-filter band for CEOF analysis is changed. A wedge-shaped pattern of a negative signal appears in a phase lag ϕ = 0° (Fig. 4-2, top left) with quasi-symmetry about the equator. There is a pair of negative signals in the subtropical eastern Pacific of both hemispheres. The northern part of it extends from the off Baja-California to the central basin at around 12°N, and southern part of it has its center around 120°W at 10°S with an inclination from southeast to northwest. It can be seen that the northern signal propagates westward as phase (time) proceeds. Along latitude band between 20°N and 30°N, for example, there is a negative anomaly near the eastern coast at ϕ = 0°, and it proceeds near the date line at ϕ = 180°, meanwhile, there is a positive anomaly near the date line at ϕ = 0°, and it reaches near the western boundary at ϕ = 180°. On the other hand, signals in the tropics and the South Pacific reveal standing oscillation rather than propagating feature. At ϕ = 90°, the feature of positive anomaly along the equator is reminiscent of equatorial signal in ENSO that propagates eastward as Kelvin waves.

The second CEOF mode of the interdecadal VAT variation (hereafter VAT-2) is shown in Fig. 4-4. A positive signal appears at the midlatitude central (ϕ = 60°) and develops in the midlatitude central North Pacific. Then it moves southwestward in the central North Pacific (ϕ = 90 ~ 120°) to the latitude around 20°N. Afterwards, it extends to the subtropical western Pacific region at phase lags from ϕ = 150° to ϕ = 180°. Evolution of spatial pattern of this mode seems there are signals clockwisely rotating along the subtropical gyre circulation of the North Pacific. The percentage of explained variance is 21.2% and much larger than the third (11.5%) and fourth (8.1%) mode. Thus VAT-2 is robust and is well separated from higher mode with statistical significance. The spectrum for VAT-2 shows

obvious difference from that for VAT-1 (Fig. 4-3). It has a dominant peak around 15-year period. Thus, we consider there are two distinct modes at least in the upper ocean temperature variability in our model.

4.2 ENSO-like Evolution of the Primary Mode

The first mode of interdecadal VAT variation has good correlation with variations in the SST and the surface wind stress, which have coherent basin-wide spatial patterns. Associated SST and wind stress variation are estimated with regression on the reconstructed temporal coefficients (for example, variation for $\phi = 0°$ is obtained by projection on the real part of principal component) of VAT-1 (Fig. 4-5). In the tropical Pacific, a westerly (easterly) wind anomaly appears in the west-central Pacific and a positive (negative) SST anomaly appears in the central-eastern Pacific, when the positive (negative) VAT anomaly appears in the eastern Pacific. These features are similar to those in ENSO, except that meridional extent of the interdecadal signal is broader. A basin-wide spatial pattern of the SST at $\phi = 120°$ is almost identical to the SST-1 (Fig. 3-2b), and correlation between the temporal coefficients for the VAT-1 (reconstructed for $\phi = 120°$) and the SST-1 is 0.79. Correlation higher than 0.46 are significant at 95 % confidence level for the filtered data. It is shown that the VAT-1 is closely linked with the SST-1. The SST oscillates stationary keeping the basin-wide spatial pattern, whereas the VAT signals in the North Pacific propagate across the basin. The SST variation in the midlatitude central North Pacific appears to be slightly delayed relative to the variation at the equator (maximum at $\phi = 120°$ vs. $\phi = 180°$).

At the time of the largest amplitude of the equatorial SST anomaly, the wind stress anomaly also has the largest amplitude over the entire Pacific (Fig. 4-5b, $\phi = 120°$). There is a strong westerly wind anomaly in the western-central equatorial region. A cyclonic pattern is notable in the subtropical North Pacific with its center north of Hawaii. This wind anomaly indicates weakened wind speed in the trade wind zone that induces increase of the SST due to decreased evaporation. The southerly wind anomaly near the eastern coast contributes to Ekman downwelling (not shown), which makes positive VAT anomaly in the eastern subtropical Pacific. Another cyclonic wind anomaly is seen in the northern North Pacific implicative of intensification of the Aleutian Low.

Evolution of vertical structure of the upper ocean temperature is examined with the similar procedure with that for SST and wind stress. The ocean temperature variations in cross sections along 20°N and the equator are shown in Fig. 4-6. We selected the 20°N latitude section because the signals become strong at this latitude in the western Pacific. At 20°N, westward propagating signals are found in the subsurface layer. A signal is formed

near the surface in the eastern Pacific. As the signal migrates westward, its maximum is detached from the surface in the central basin. It appears that it is propagating as a wave in the upper layer of the thermocline (~100 *m* depth) in the model.

Along the equator, there is a large temperature variation in the western Pacific centered at around 100 *m* depth and a surface variation in the central-eastern Pacific with an opposite sign. The vertical structure indicates an east-west seesaw of the thermocline depth that dominates in the central-western Pacific and is similar to what is observed in El Niño. When the positive subsurface signal at 20°N reach around 150°E (between ϕ = 40° and ϕ = 80°), temperature anomaly along the equator is switched to positive at the surface in the eastern Pacific. The change seems to occur in a very short period. It is plausible to interpret the eastward migration of subsurface signal in such a short period as an ensemble effect of propagation of the equatorial Kelvin waves. Individual signals that suggests propagation of the equatorial Kelvin waves are not visible in filtered data, though they are seen in the ENSO timescale (Yukimoto et al., 1996).

We examined phase relationships between the variations of possible forcing acting on each other. Covariance distributions in the phase lag (in ordinate, time increase upward) relative to the VAT-1 and the longitude (in abscissa) along 20°N are shown in Fig. 4-7. The SST (Fig. 4-7a) reveals large fluctuations in the eastern Pacific and its temporal evolution seems rather standing than propagative.

In contrast, propagation of the temperature anomalies is apparent in the upper thermocline (Fig. 4-7b). Its apparent westward velocity is different between the eastern Pacific and the west central Pacific. Estimated phase velocities for each region are shown in Table 4-1. Since the spectrum of the VAT-1 (Fig. 4-3) shows large variability in the broad range periods from 10 years to 30 years, the phase velocity is examined for 10, 20 and 30 year periods respectively. The apparent westward phase speed is about 1.5 $cm\,s^{-1}$ in the central Pacific (160°W - 150 °E) and about 4.6 $cm\,s^{-1}$ in the eastern Pacific (100°W - 160°W), for the assumed period of 20 years. These values range from 1.0 $cm\,s^{-1}$ and 3.1 $cm\,s^{-1}$ to 3.0 $cm\,s^{-1}$ and 9.2 $cm\,s^{-1}$, for the period range from 30 years to 10 years, respectively. Apparent velocity of the westward signal propagation at 30°N is also estimated from similar analysis (not shown), and is found to be about 1.5 ~ 3.6 $cm\,s^{-1}$ for 20 year period oscillation.

The velocities of the first and second mode of free baroclinic Rossby waves inferred from the model ocean stratification (zonally averaged in the Pacific sector) are also shown in Table 4-1. The free first baroclinic mode has phase velocity of –7 ~ –8 $cm\,s^{-1}$ at 20°N, and the second baroclinic mode has phase velocity of –2 ~ –2.3 $cm\,s^{-1}$, approximately. The vertical structure of the propagating signal appears to be basically the first baroclinic mode (Fig. 4-6a), however, the apparent phase speeds for dominant period of 20 years are much

slower than the free first baroclinic mode. The discrepancy of the propagation speeds will be discussed later.

The surface heat flux variation (Fig. 4-7c) positively correlates with the SST variation at the subtropical (20°N) North Pacific, though its statistical significance is small. To the east of 170°W, especially in the longitudes between 140°W and 160°W, the ocean heating (cooling) is almost in-phase with the positive (negative) SST anomaly. In the higher latitude (30°N-40°N; not shown), similar relationship between the surface heat flux and the SST is found with larger significance, that is, the ocean heating positively correlates with the SST variation in the eastern region (where the SST is positively correlates with the tropical SST variation) and central North Pacific (where the SST is negatively correlates with the tropical SST).

The wind stress curl mainly fluctuates between 170°E and 140°W with maximum amplitude around 160°W. There is little propagating feature in the wind stress curl variation; rather it is regarded as a standing oscillation that synchronously excites the upper thermocline temperature anomaly. The positive (negative) wind stress curl locally makes Ekman pumping (downwelling) effect, and generates Rossby waves, which propagate westward. Therefore, the fluctuating wind stress curl can make remote response of the subsurface in the west of the forcing center with a few year time lags. Consistently with this, the positive anomaly of the upper thermocline temperature is enhanced in the western side of a negative anomaly of the wind stress curl.

Similar analysis as in Fig. 4-7 (but with zonal wind stress instead of wind stress curl) is made for the equator section (Fig. 4-8). During the upper thermocline temperature anomaly is positive (Fig. 4-8b, around $\phi = -120° \sim 30°$), heat is piled up in the subsurface equatorial western Pacific with the lowered thermocline (see also Fig. 4-6a, b $\phi = 120°$ but opposite sign). This state accompanies a negative SST anomaly in the central-eastern Pacific (with the maximum amplitude around the date line), and an easterly wind stress anomaly (Fig. 4-8d) and a positive heat flux (ocean heating) anomaly in the central Pacific (Fig. 4-8c). Easterly wind anomaly forces the thermocline lowered in the western Pacific, and intensifies the equatorial upwelling that contributes to the negative SST anomaly. Therefore, the wind stress variation implies positive feedback on the equatorial SST variation through wind-upwelling relation. The surface heat flux anomaly is negatively correlates with the SST anomaly, therefore it implies that the surface heat flux variation behaves as a damping on the equatorial SST variation. Increase of solar irradiance due to decrease of cloud amount (not shown) with weakened convective activity contributes to the increase of ocean heating.

When the positive subsurface anomaly at 20°N comes into the western Pacific (Fig.

4-7b; with its maximum around 160°E), the equatorial upper thermocline temperature anomaly in the eastern Pacific changes sign from negative to positive (Fig. 4-8b, around ϕ = 20°). This change accompanies the changes in the SST, zonal wind stress and heat flux (Figs. 4-8a, 4-8d and 4-8c). These changes occur almost simultaneously, except that the transition of the upper thermocline temperature in the equatorial eastern Pacific slightly leads other changes. It is noted that the phase change of the equatorial SST (Fig. 4-8a) corresponds approximately to that of the wind stress curl change in the far-off-equatorial central Pacific (Fig. 4-7d).

The evolution of the variability associated with the VAT-1 is summarized as follows. The positive (negative) triangular SST pattern is formed in the tropical Pacific. For the formation of the tropical SST anomaly, the wind-upwelling positive feedback process in the equatorial region plays an important role as in ENSO. The tropical SST anomaly accompanies significant wind variation not only in the equatorial region but also in the subtropical central-eastern Pacific. The cyclonic (anti-cyclonic) wind anomaly contributes to the formation of the positive (negative) subtropical signal in the subtropical eastern Pacific. The subtropical signal propagates westward at upper thermocline depth with getting intensification by the subtropical wind forcing over the central basin. Arrival of the positive (negative) subtropical signal at the western Pacific triggers the reversal of the seesaw of the equatorial subsurface anomaly. Consequently, the equatorial SST anomaly turns from positive (negative) to negative (positive). As a whole, evolution of these variations is similar to "delayed oscillator" which is known for ENSO (Schopf and Suarez, 1988). For the present variability, a major difference from ENSO is the latitude where the signal propagates westward. The signal propagation occurs in the subtropical gyre unlike ENSO in which it occurs within the equatorial wave band. A decadal subsurface temperature signal with westward trans-Pacific phase propagation in the subtropical gyre is found in the observational data (Zhang and Levitus, 1997).

One essential process to be examined is how the propagation of subtropical signal in the thermocline affects the phase transition of the subsurface anomaly in the equatorial region. Figure 4-9 shows anomalous horizontal oceanic heat transport in the western tropical Pacific at the phase of transition (ϕ = 60°). At this phase, the subtropical VAT signal (at 20°N) reaches around the 150°E longitude. There is a region of large westward heat transport anomalies in the southern side of the positive VAT anomaly, extending to the western Pacific at latitudes between 8°N and 15°N. In that region, the heat transport anomaly vector is approximately parallel to the contour of VAT anomaly, which is suggestive of geostrophic current anomaly. At the western boundary, a large southward heat transport anomaly is dominant south of the 10°N. This suggests that an anomalous

heat is transported into equatorial western Pacific across the latitude around 10°N in accordance with an approach of the positive subtropical signal to the western boundary.

In the warm pool region as indicated with thick lines in Fig. 4-9, heat balance for the VAT variation is examined with regression on the VAT-1 (Fig. 4-10). The VAT variation averaged over the region (not shown) has 90° phase lag relative to the total tendency and becomes positive maximum at $\phi = -30°$. Heat transport due to horizontal advection is the most dominant and major contributor to the total tendency. Thus, the horizontal advection is a major component for driving the VAT variation in this region. The surface heat flux has second importance but it is almost in-phase with VAT variation (lags about 90° to the total tendency). At the phase of maximum VAT, there is a negative SST anomaly in the central-eastern basin, and a strong positive heat flux anomaly is located where the SST anomaly is large (Fig. 4-8a-c). This suggests that the heat flux acts as a negative feedback for the SST variation but acts as a positive feedback for the VAT variation in this region. Contribution from vertical diffusion has about a half amplitude of that from horizontal advection and varies almost in-phase with that. Contribution from vertical advection is not significant in this region.

It is shown that the major process, which connects variations in the subtropics and the equator, is the oceanic horizontal heat transport through the western boundary. This process resembles to the Rossby wave reflection at the western boundary as seen in the equatorial region for ENSO (except its much broader meridional extent). Gu and Philander (1997) discussed on another mechanism of decadal variability in the tropical Pacific. In their hypothesis, subtropical subsurface signal is advected from the subduction region in the midlatitude, and it is further advected into equatorial region through shallow meridional overturning. In our model, on the contrary, subduction is not seen associated with the present variability.

The other point to be noted is how and where the subtropical VAT signal is formed. The wind forcing associated with the variation of the subtropical anti-cyclone is significant (Fig. 4-5b). The wind variation induces the surface heat flux change (Fig. 4-7c) through the variation of the wind speed of the trade wind. In addition, the wind variation along the eastern coast changes the Ekman drift and upwelling near the eastern coast. It is considered that the both changes work for enhancing the wedge-shaped VAT anomaly in the eastern basin. However, it is not clear whether the variation of the subtropical anti-cyclone is attributed to the local feedback from oceanic variation in the subtropical eastern Pacific, or the remote forcing from the tropical SST anomaly through the variation of the Hadley circulation. To make it clear, some AGCM experiments forced by the SST anomaly would be required.

Although the feedback loop of the variability mechanism is closed within the tropics and subtropics as mentioned, influence of the tropical SST variation extends to the midlatitude. The tropical SST anomaly accompanies an anomalous atmospheric convective activity in the tropical western Pacific, which induces the midlatitude atmospheric circulation anomaly with teleconnection patterns (Horel and Wallace, 1981), and consequently forces the midlatitude ocean (e.g., Miller et al., 1994). These processes are consistent with the claims that the interdecadal variability of the SST in the midlatitude North Pacific is primarily attributed to the tropical SST variation, as argued by Graham et al. (1994), Lau and Nath (1994) and others. It is considered that the SST anomaly in the central-western North Pacific in the midlatitude in the CGCM (Fig. 4-5a) is a result of these processes.

The temporal structure of the variability is determined by the combination of the strength of coupling and the delay time in the feedback mechanisms. This is typically seen in the theory of the delayed oscillator in the ENSO oscillation (Suarez and Schopf, 1988). The propagation of the off-equatorial signal determines the ENSO timescale. Processes found for the first mode coupled variability in the CGCM are conformed to the above conditions. The timescale of the first mode depends on the travel time of the subtropical signal to transverse the basin. Since the signal in the western Pacific is dominant at around 20°N, signal propagation at this latitude seems to determine the dominant timescale. The apparent propagation is faster in the eastern basin (~4.6 $cm\ s^{-1}$) than in the central-western basin (~1.5 $cm\ s^{-1}$). The vertical structure of the propagating signal appears to be basically the first baroclinic mode (Fig. 4-6a), however, the apparent phase speeds for dominant period of 20 years are much slower than the free first baroclinic mode. As the propagating signal in the model is forced by continuously varying wind stress curl (Fig. 4-7d), it is considered that group velocity of Rossby wave is modulated, and that of free modes are not directly applicable. Location of the wind stress curl itself also shows a little migration while forcing the traveling signal. With a linear model including forced baroclinic oceanic Rossby wave and a simple atmospheric feedback effect, Jin (1997) showed that a frequency of the oscillation (which is interpreted as apparent velocity of the trans-Pacific signal) depends on spatial structure of the wind forcing. The variation of wind forcing structure may also affect the timescale of this mode. Recent work by Liu (1998a,b) suggests that anomalous Ekman pumping generates the first baroclinic Rossby wave which propagates fast and straight westward without Doppler-shift, and the second baroclinic Rossby wave which propagates slowly in the direction of the subsurface flow. Since the subsurface flow is nearly zonal around the 20°N in the model, non-linear influence of these waves also might have some relevance to the modulation of propagation speed.

Our result is similar with what is simulated by KM98 in some aspects. The decadal SST variation in KM98 has similar triangular pattern; also, there is the westward propagation in the upper ocean temperature. However, the westward propagation of the signal in KM98 is confined around 12°N, whereas that in our model extends further north (20°N~30°N) from the subtropics to the midlatitude. This seems consistent with the difference of dominant timescales, that is, our mode has longer timescale (~20 years) than that of KM98 (we estimated it approximately as 12 years from their Fig. 3-5). We showed forcing of the subtropical wind variation plays an important role for the formation and reinforcement of the subtropical subsurface signal. It is considered that the spatial structures of the wind variation (especially in the subtropics) are different between the models, though unfortunately, KM98 did not explicitly shown their subtropical wind variation.

In the CGCM , the surface heat flux in the equatorial region has damping effect on the SST anomaly that is primarily caused by the equatorial ocean dynamics. In SGCM, however, the dominant components of the surface heat flux variation (i.e., latent heat and shortwave radiation) show basically positive feedback on the local SST (Kitoh et al., 1999). There is no coherent negative feedback forcing, but only the summation of the each component results in unstable oscillatory variation. Cause of the variation of the total heat is not known. It might be a result of a stochastic atmospheric forcing, which can accounts for the incoherent temporal structure of the variability in the SGCM, while the variability in the CGCM has the dominant timescale associated with the dynamical mechanism as mentioned above.

4.3 The Other Interdecadal Variability

The SST-2 of the CGCM shows good correspondence with the observed SST-2. Associated VAT variation is estimated with regression on the SST-2 (not shown), which is basically standing oscillation with a dominant variation in the midlatitude. It is characterized by a dipole pattern in the North Pacific and somewhat resembles to the pattern in VAT-1 at $\phi = 60°$ (Fig. 4-2) but the center of action is shifted further north. Since the dominant timescale for the SST-2 is longer than 50 years and the associated VAT variation has low statistical significance, we were unable to make detailed analysis about this mode. Taking into account that the SST-2 of SGCM has similar spatial pattern in the North Pacific, dynamical effects of ocean seems not essential for the mode in CGCM. However, since the dominant timescale is very long, the standing oscillation in the associated VAT does not necessarily means the absence of any ocean dynamical mechanism.

By filtering out very long-term variation (longer than 50 years), the VAT variation in CGCM shows the robust second mode with rotating signals (Fig. 4-4). Regressing on the VAT-2, the variations of SST and the surface wind stress are shown in Fig. 4-11. It is characterized by a tri-pole pattern: a positive anomaly in the central North Pacific, a negative anomaly in the subtropical eastern North Pacific and a positive anomaly in the eastern South Pacific (anti-symmetrical to the northern negative anomaly about the equator). This tri-pole SST pattern is close to that for the third EOF of SST (not shown). The wind stress pattern (Fig. 4-10b) seems coherent to the SST pattern: a strong westerly wind anomaly in the northern North Pacific, an anti-cyclonic pattern in the subtropical central-eastern North Pacific and an anomalous wind flowing across the equator and continuing to a northwesterly wind anomaly in the southern hemisphere. It is interesting that these SST and wind patterns are reminiscent of the Pan-Atlantic decadal oscillation that is seen in the Atlantic (Xie and Tanimoto, 1998). However, the variation that corresponds to this mode has not been found in the Pacific for the observed data.

The second mode of VAT variation is characterized by clockwise rotation of the signal along the subtropical gyre in the North Pacific. Latif and Barnett (1994) presented a similar apparent feature of the ocean heat content. They argued that the rotating behavior is attributed to the spin-up (spin-down) of the subtropical gyre by the midlatitude atmospheric change. The associated meridional heat transport by the western boundary current changes the northwestern midlatitude SST to reverse the phase of the cycle. In our CGCM, a spin-up (spin-down) of the subtropical ocean gyre is recognized associated with the second VAT mode. With this dynamical response of the ocean, however, the meridional heat transport works for maintaining or enhancing the midlatitude SST anomaly rather than reversing the phase. In this sense, it is hard to consider that our second VAT mode is a manifestation of atmosphere-ocean coupled instability. Rather, this mode might be regarded as a resonance-like response of the ocean to a stochastic atmospheric forcing (Saravanan and McWilliams, 1997). This remains highly speculative and should be pursued more in future.

4.4 Sammary and Discussion

It is shown that the coupled model with a dynamical ocean model (CGCM) reproduces basin-wide patterns of the principal SST variability similar to the observed one. Temporal structures of the SST variability also agree well between the observation and the CGCM. On the other hand, SGCM (a slab ocean model coupled to the same atmospheric component as in the CGCM) fails to simulate the observed temporal structure. It is suggested, therefore, that the timescale of the coupled variability is associated with

dynamical processes in the ocean.

A distinct interdecadal mode of the coupled atmosphere-upper ocean temperature variability is found in the Pacific Ocean in the CGCM. This mode accompanies an ENSO-like spatial structure for the SST and the surface wind in the tropical Pacific. It is suggested that the mode is reinforced by the positive feedback in the tropical atmosphere-ocean coupling processes similar to ENSO. Associated with the variation in the tropical Pacific, subtropical ocean temperature signal is formed in the eastern Pacific as well as in the central North Pacific (with the opposite sign). Subsequently the eastern signal propagates westward as a signal in the upper thermocline. During the transverse of the basin, the signal is intensified in the central basin by the wind stress forcing. When the signal gets into the western Pacific, the heat transport at the western boundary changes, which triggers the phase change of tropical air-sea coupling. Consequently, the anomalies in the tropical Pacific are switched to the opposite sign. This subtropical westward trans-Pacific signal in the upper thermocline temperature appears to determine the timescale for the mode that behaves like a delayed oscillator in ENSO. In short, we can conclude that the mode is excited by tropical air-sea interaction and its timescale is regulated by the subsurface signal propagation, which is forced by the subtropical wind forcing.

The CGCM successfully simulated the second mode of SST with a major variation in the midlatitude North Pacific as in the observed SST. In the upper ocean temperature, we found another distinct mode, which is characterized by a midlatitude-subtropics dipole pattern rotating clockwise around the North Pacific subtropical gyre. However, the associated SST variation of this mode shows a poor correspondence in the dominant interdecadal modes for the observed SST.

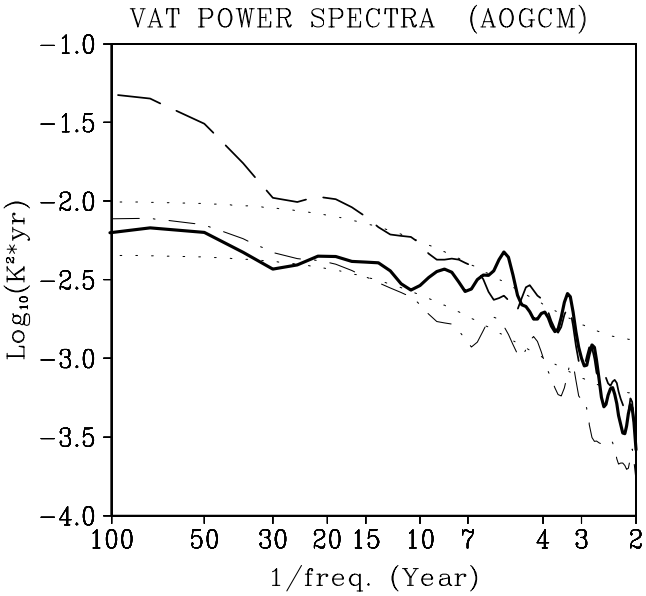

Figure 4-1 Temporal spectra of the VAT, averaged over the North Pacific (150°E-90°W, 15°N-55°N) (dashed curve), tropical Pacific (150°E-90°W, 10°S-10°N) (solid curve) and South Pacific (150°E-90°W, 35°S-15°S) (dot-dashed curve). Values are in common logarithm of the power density of temperature (unit is K^2). Thin dotted curves show red spectra by AR1 model fitted to the tropical Pacific VAT and its 95% confidence level.

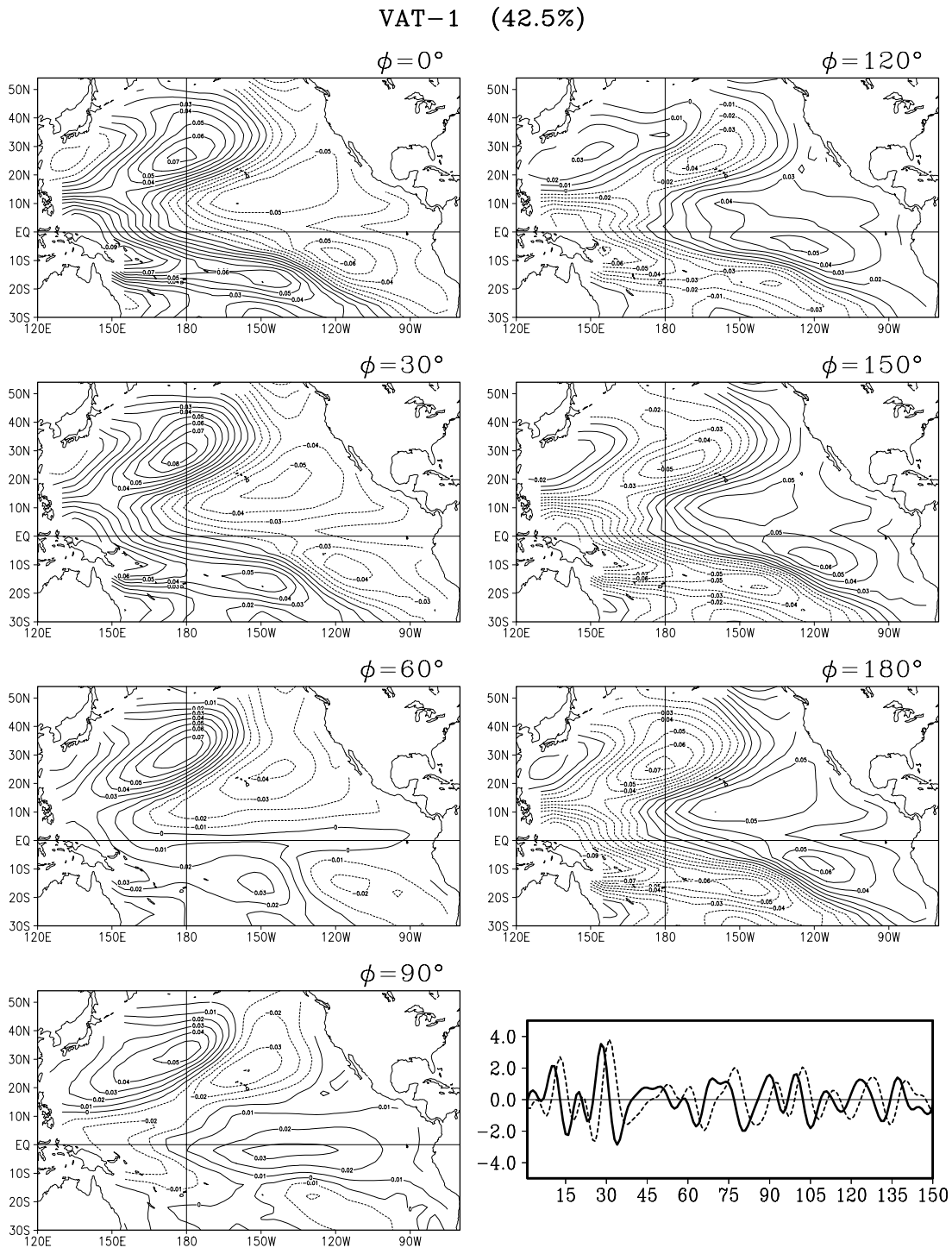

Figure 4-2 Reconstructed spatial patterns of the first mode of CEOF for the interdecadal VAT (0-600m) variation (period: 8-50 years) for phase lags from 0° to 180° at 30° interval (contour plots), and real (solid curve) and imaginary (dashed curve) part of the temporal coefficients (right bottom panel). Values in the spatial patterns denote variance (unit is K^2). Temporal coefficients are normalized to have unit standard deviation.

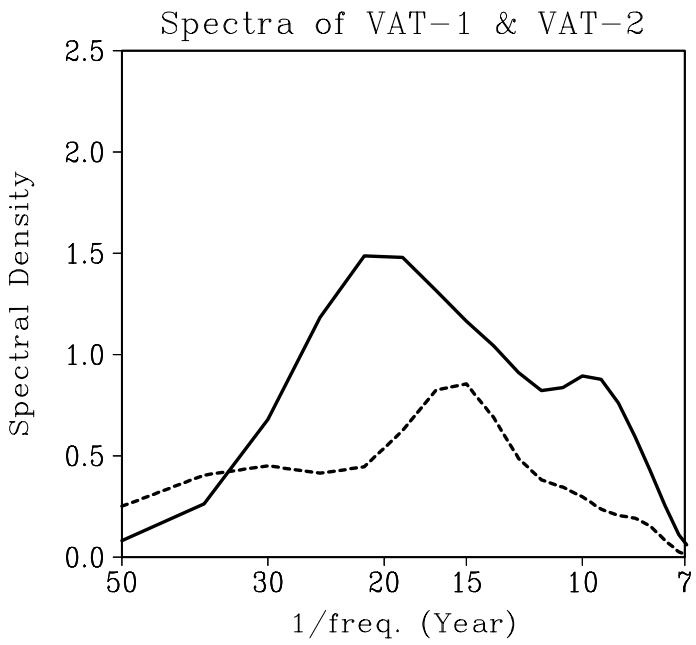

Figure 4-3 Power spectra of the temporal coefficients of the interdecadal VAT (pre-filtered periods 8-50 years) CEOFs, for the first mode (solid curve) and the second mode (dashed curve). Values are common logarithm of the power density of temperature (unit is relative).

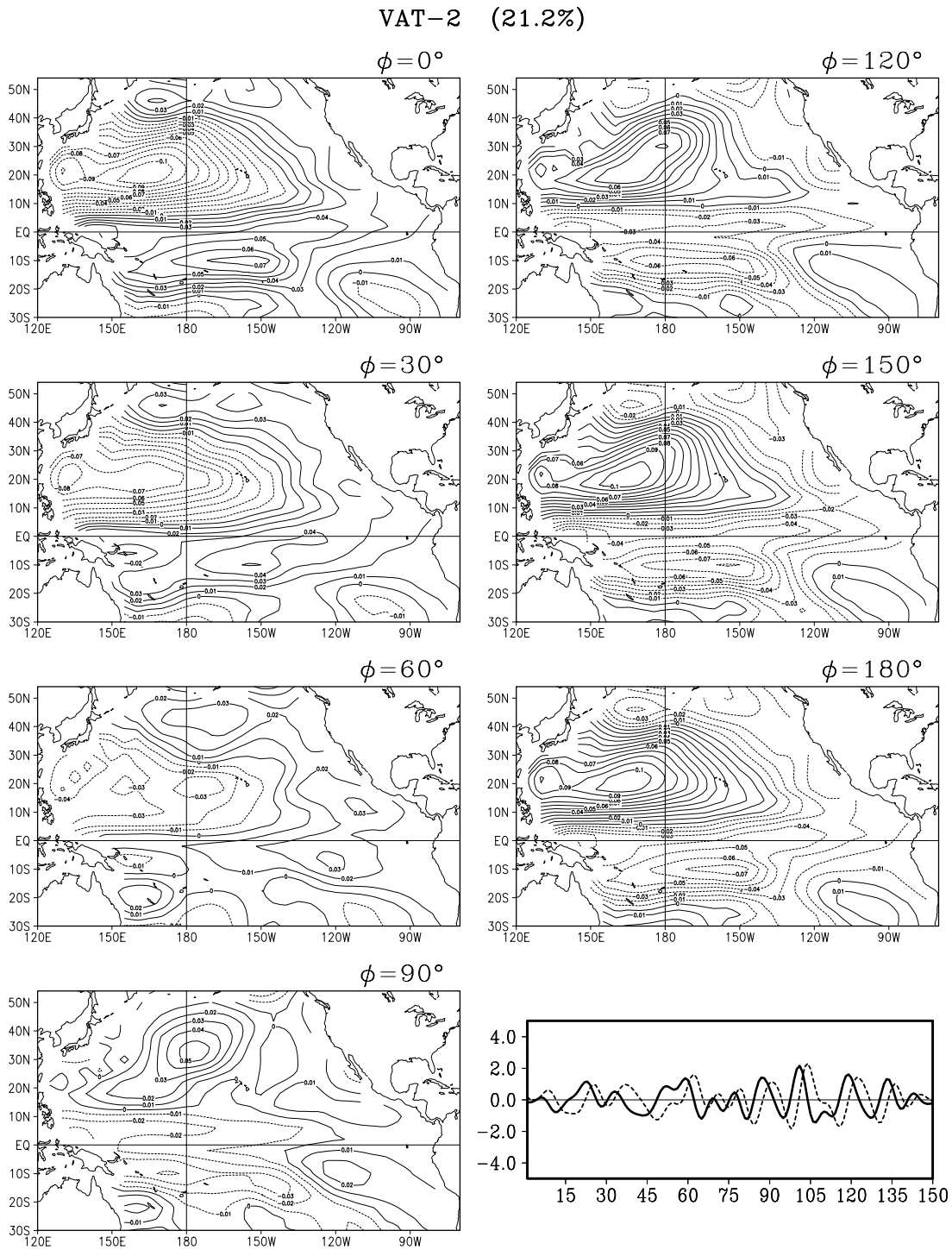

Figure 4-4 Same as Fig. 4-2 except for the second mode of CEOF.

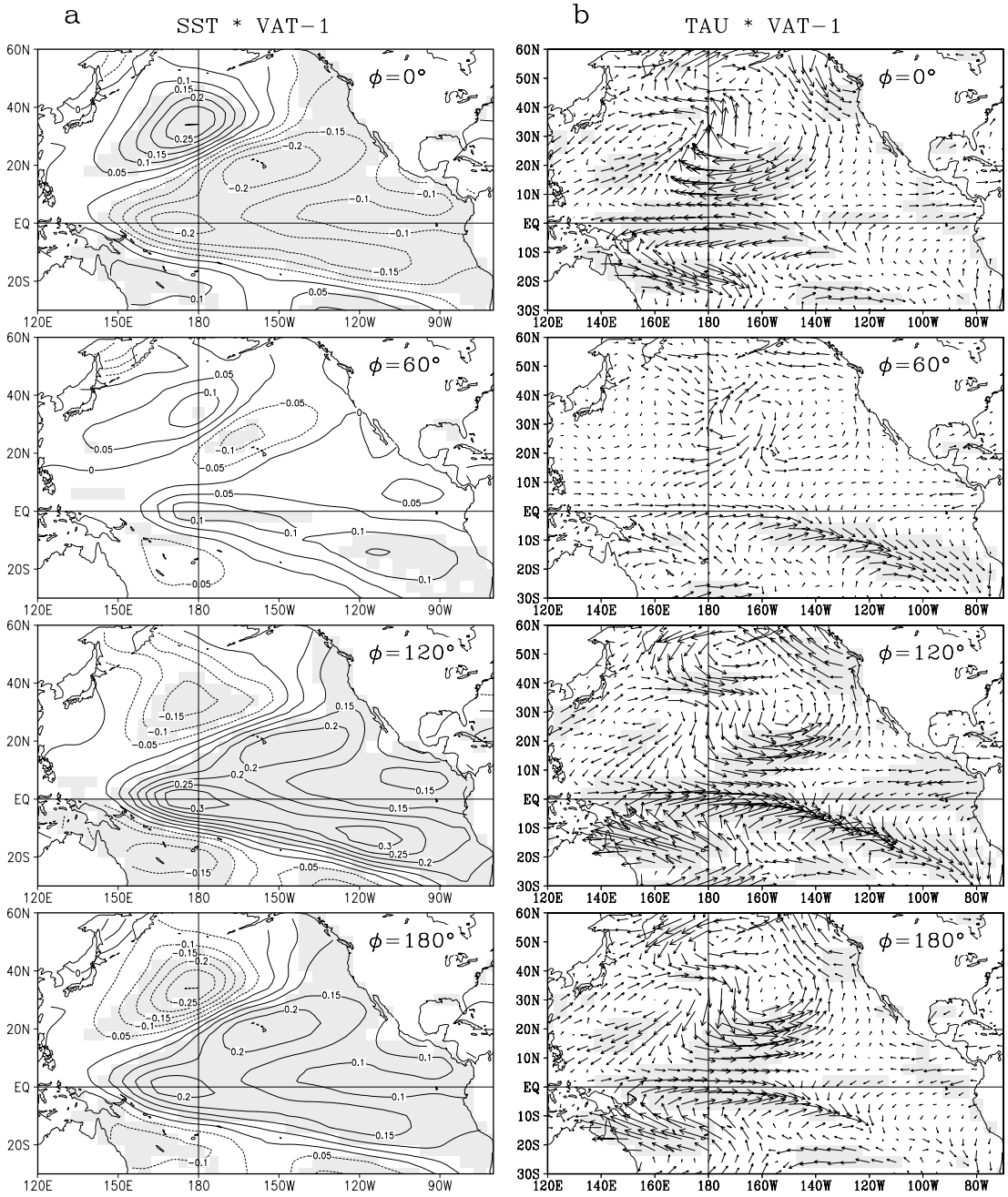

Figure 4-5 Variations of (a) the SST (left panels) and (b) surface wind stress (right panels) corresponding to the first mode at the phase lags 0°, 40°, 80° and 120°, obtained by regressing on the temporal CEOF of the VAT reconstructed for each phase lags. Correlations significant at the 95% level are shaded.

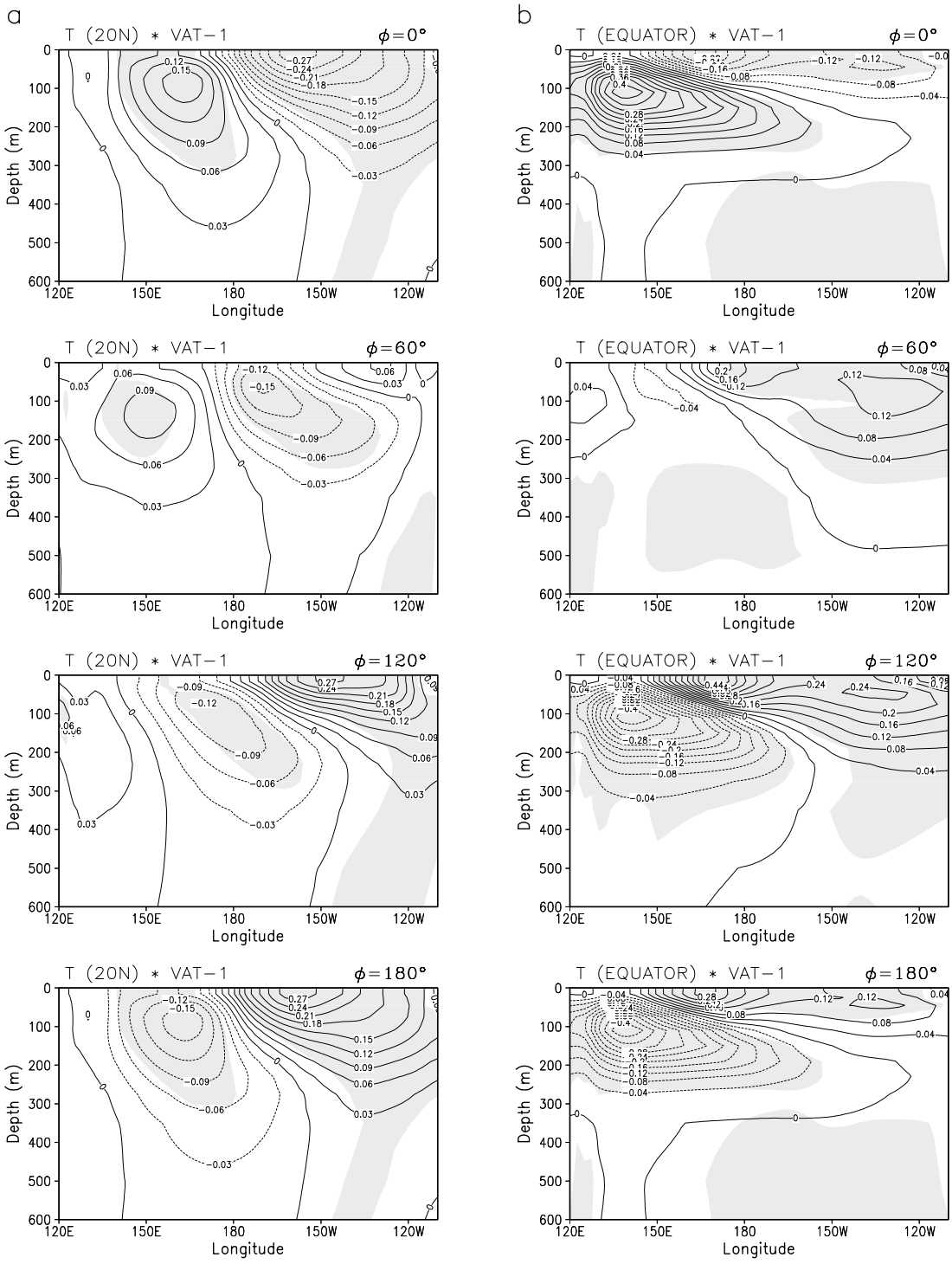

Figure 4-6 Ocean temperature variations for the first mode in the zonal vertical section (a) along 20°N and (b) along the equator, at the phase lags 0°, 40°, 80° and 120°, obtained by regressing on the temporal CEOF of the VAT reconstructed for each phase lag. Correlations significant at the 95% level are shaded.

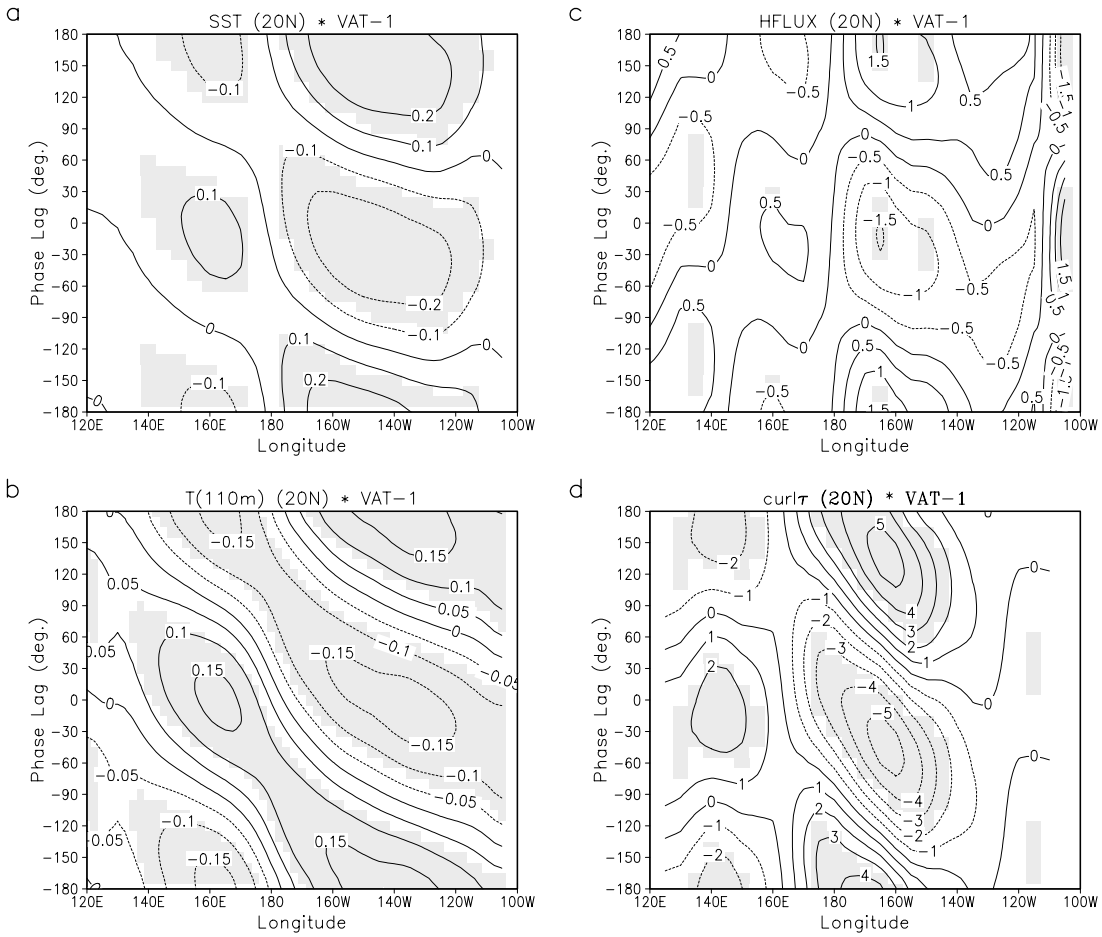

Figure 4-7 Longitude-phase plots for the variations along 20°N of (a) SST, (b) ocean temperature at 110m depth, (c) positive downward surface heat flux and (d) surface wind stress curl, corresponding to the first mode, obtained by regressing on the reconstructed temporal CEOF of the VAT. Correlations significant at the 95% level are shaded. Values denote covariance in units (a) K^2, (b) K^2, (c) Wm^{-2}, (d) $10^9\ Nm^{-3}$.

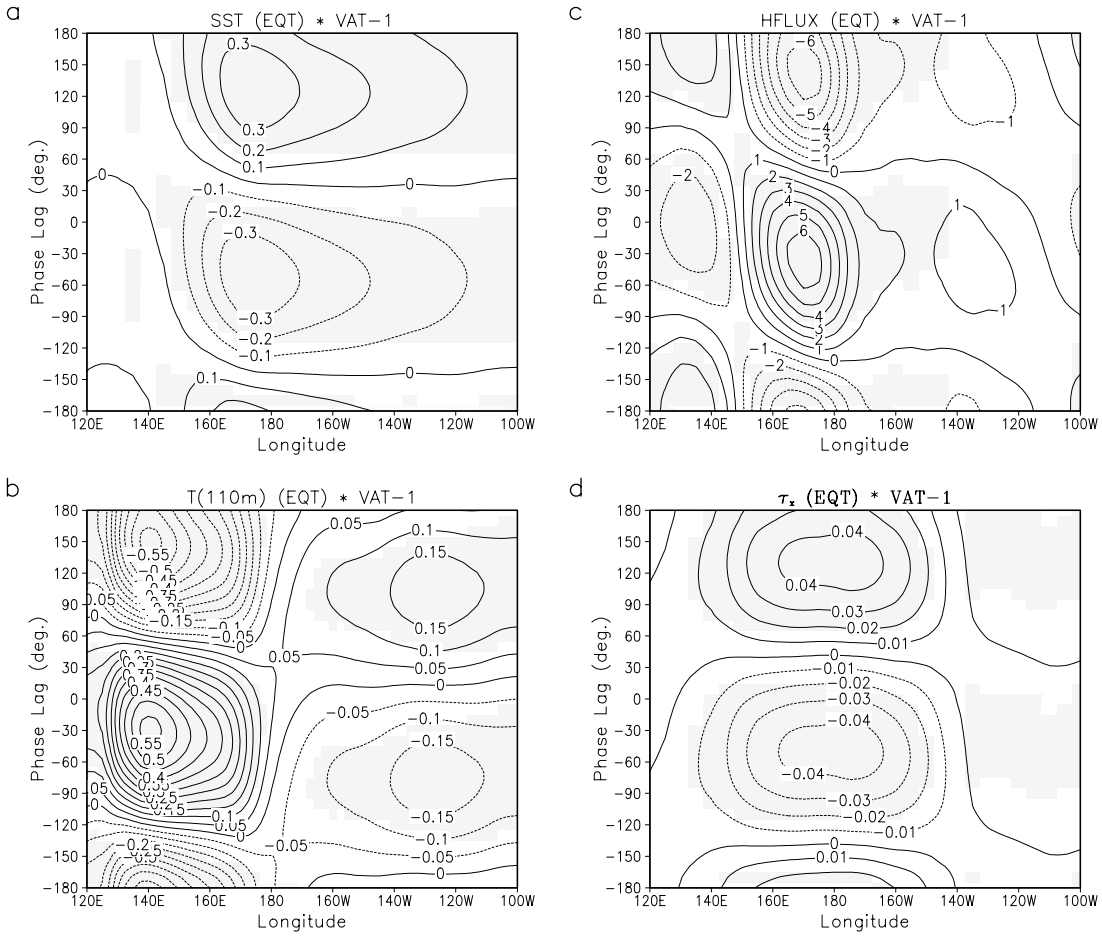

Figure 4-8 Longitude-phase plots for the variations along the equator of (a) SST, (b) ocean temperature at 110m depth, (c) positive downward surface heat flux and (d) zonal surface wind stress, corresponding to the first mode, obtained by regressing on the reconstructed temporal CEOF of the VAT. Correlations significant at the 95% level are shaded. Values denote covariance in units (a) K^{-2}, (b) K^{-2}, (c) Wm^{-2}, (d) Nm^{-2}.

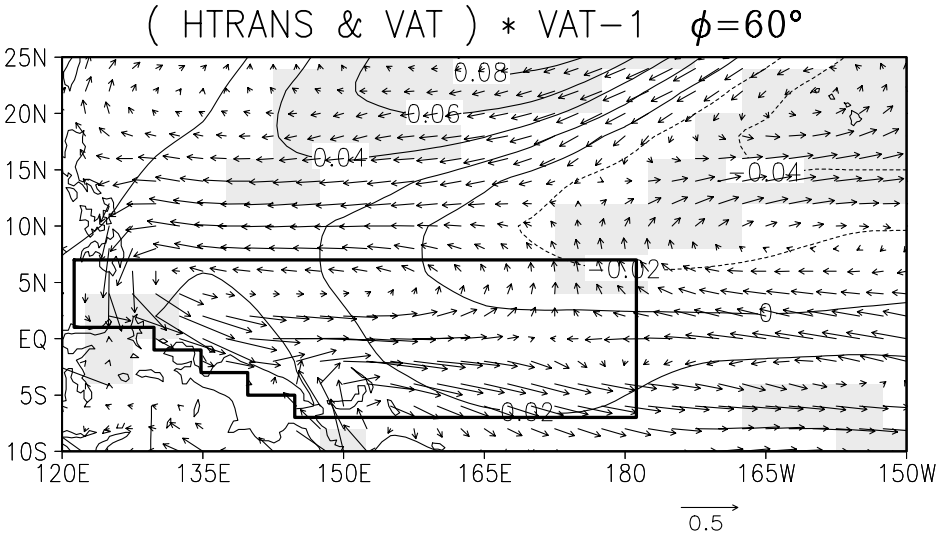

Figure 4-9 The horizontal oceanic heat transport (average of 600m) variation (arrow plot) and the VAT variation (contour plot) in the tropical western Pacific for the first mode, obtained by regressing on the temporal CEOF of the VAT reconstructed for phase lag 60°. Correlations (for the VAT) significant at the 95% level are shaded. The region bounded by thick lines is for the heat balance calculation that is shown in Fig. 4-10.

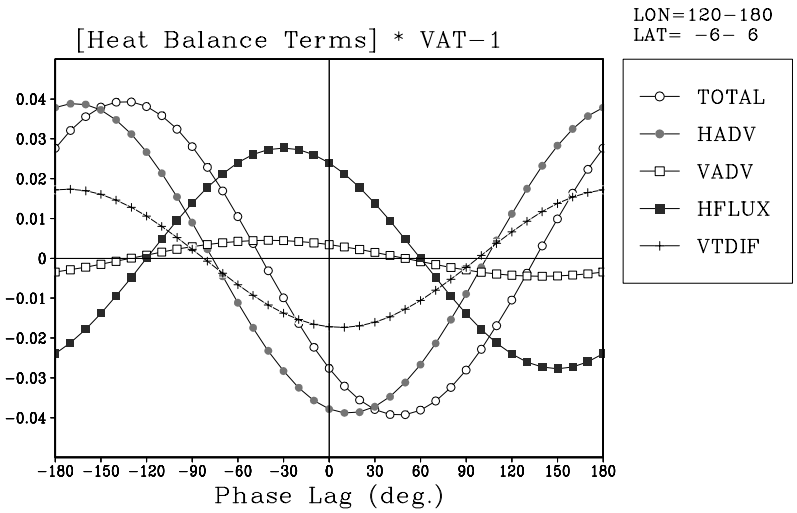

Figure 4-10 Lag regressions of the heat balance terms for the first mode at the equatorial western Pacific (the region shown in Fig. 4-9) on the reconstructed temporal CEOF of the VAT. Curves show contributions to total tendency of the VAT (open circle) by horizontal advection (shaded circle), vertical advection (open square), surface heat flux (filled square), vertical diffusion (cross).

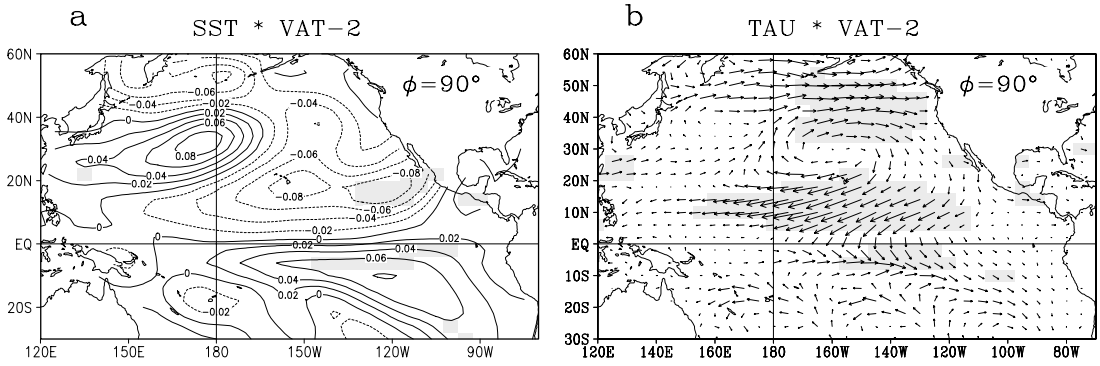

Figure 4-11 Same as Fig. 4-5 except for the second mode of CEOF for the phase lag 90°.

Table 4-1 Apparent phase velocity (positive for eastward) of the subsurface (at 110m depth) signal at 20°N corresponding to the VAT-1 estimated for oscillation periods of 10, 20 and 30 years respectively, and phase velocity of the first and second baroclinic Rossby wave estimated from the stratification of the model (right two columns).

	P=10 years	P=20 years	P=30 years	First Rossby	Second Rossby
Eastern Pacific (100∝W - 160∝W)	ñ9.2 cm/s	ñ4.6 cm/s	ñ3.1 cm/s	ñ7.5 cm/s	ñ2.0 cm/s
Central Pacific (160∝W - 150∝E)	ñ3.0 cm/s	ñ1.5 cm/s	ñ1.0 cm/s	ñ8.6 cm/s	ñ2.3 cm/s

5 Irregularity of El Nino in the MRI-CGCM2

In this section, the irregularity of El Niño is investigated with a 400-year simulation of the MRI-CGCM2.

5.1 Model ENSO in the MRI-CGCM2

5.1.1 Simulated SST Variability in the Tropical Pacific

Figure 5-1 shows the time series of the SST anomaly in the NINO3 region (150°W-90°W, 5°S-5°N) (hereafter SST-NINO3), for the first 200 years of the 400-year simulation. There are prominent interannual oscillations in the SST-NINO3 time series. The correlation between SST-NINO3 and the Southern Oscillation Index (SOI; defined as mean sea level pressure difference of Tahiti minus Darwin; not shown in the figure) is –0.72, which implies the well-known air-sea covariant relationship in the observed ENSO. The SST-NINO3 frequently shows several large positive peaks (El Niño) exceeding +4°C, while it shows the maximum negative peaks around –2.5°C (La Niña). This asymmetric amplitude for El Niño versus La Niña is also a realistically simulated feature in the observed ENSO. With respect to the magnitude of variability, the standard deviation of SST-NINO3 is 1.6°C, which is substantially larger than the observed 0.7°C. The maximum peak value of +4°C is comparable with that for the observed 1997/98 El Niño (+3.6°C), however, such strong events happen more frequently in the model than are observed.

It is apparent that there is an interdecadal modulation of the SST-NINO3 amplitude. For instance, years 105-130 and 150-185 appear to be active periods with a number of large events, while years 60-70, and 130-145, are relatively calm periods. With respect to frequency, quasi-biennial oscillation appears dominant, however, longer (3 - 6 years) intervals become notable in the active periods, with larger peaks in SST-NINO3. This implies that there is a frequency modulation that might be related to the amplitude modulation.

The time series of the equatorial zonal-mean ocean heat content anomaly is also shown in Fig. 5-1. The vertically averaged temperature from the surface to 300 m depth (VAT300) is defined as an indicator of the ocean heat content, which reflects a variation of thermocline depth. It is apparent that this variation is closely linked with the SST-NINO3 variation. A peak in the ocean heat content anomaly precedes the SST anomaly peak. Larger heat anomalies build up prior to a larger SST anomaly in many cases.

5.1.2 Spatial Structure

The geographical anomaly distributions associated with the model ENSO for SST

and zonal wind stress are examined with projections on the SST-NINO3 time series with linear regressions (Fig. 5-2). The SST anomaly pattern in the tropical Pacific is similar to what is typically observed, that is, a positive anomaly extending from off-Peru to the central Pacific along the equator. The atmospheric response in the tropical Pacific on the SST anomaly is remarkable in the wind stress anomaly distribution (Fig. 5-2b) that shares basic features with the observed one. There is a significant westerly wind stress anomaly in the west central Pacific near the equator. In the off-equator regions, easterly anomalies are seen around the Inter-Tropical Convergence Zone (ITCZ) in the Northern Hemisphere, and the South Pacific Convergence Zone (SPCZ) in the Southern Hemisphere.

This wind anomaly pattern is closely related to the precipitation change with an enhancement in the central Pacific along the equator, and a weakening along the ITCZ and SPCZ. The enhanced convective precipitation in the equator leads to an anomalous local Hadley circulation with the ascending branch on the equator, as well as an anomalous Walker circulation with a westerly wind anomaly along the equator in the west-central Pacific. The anomalous Hadley circulation accompanies descending branches near the ITCZ and the SPCZ, which are associated with the suppression of convective activity. For the observed El Niño, Oort and Yienger (1996) demonstrated that the atmospheric meridional circulation becomes stronger than normal with its ascending branch at the equator and descending branch near the ITCZ accompanying an easterly wind anomaly around the ITCZ, which leads to an enhancement of the atmospheric poleward heat transport at the tropical latitudes. The meridional gradient of the zonal wind stress anomaly implies a pair of positive wind stress *curl* anomalies, along the off-equator region in both hemispheres, which will lead to anomalous poleward Sverdrup flows in the upper ocean.

5.1.3 Temporal Evolution

Figure 5-3 shows the temporal variations of zonal distributions for SST, zonal wind stress and VAT300 along the equator (averaged between 6°S and 6°N). These are calculated with lagged regressions on the SST-NINO3 time series, to extract the related variation of the fields with the model ENSO. The variation of SST along the equator exhibits an oscillation in nearly the entire Pacific, with the maximum positive peak in the central Pacific at the 0-month lag (a simultaneous variation with SST-NINO3 by definition). There is no east-west propagation; the entire basin displays a standing oscillation without a phase difference. The zonal wind stress at the equator has a major variation in the west central Pacific. The westerly anomaly is in phase with the positive SST anomaly, which suggests that the tropical atmospheric circulation responds quickly to the SST anomaly in the equator.

The variation of ocean heat content indicates a distinct phase difference between the eastern and western Pacific. At the time of the positive peak in SST anomaly (Lag=0), the ocean heat content anomaly shows a positive in the east and a negative in the west, suggesting an anomalous eastward gradient of the thermocline along the equator, which is considered to be a dynamical response of the upper ocean to an anomalous eastward pressure gradient due to the westerly wind stress anomaly. The east-west phase lag is roughly 6 months, and it appears to be propagating eastward. The arrival of the positive ocean heat content anomaly at the eastern Pacific corresponds to the onset of the positive SST anomaly. The evolution of the ocean heat content anomaly captures the characteristics of the variations of thermocline depth and dynamic height observed by TAO/TRITON measurements. The basic characteristics of the evolution are often well represented by simple coupled models of the tropical Pacific (e.g. Battisti and Hirst 1989), and are explained by the composite effect of the contributions from Kelvin and Rossby waves (Kang and An 1998).

5.1.4 Oscillation Mechanism

The recharge oscillator mechanism in the ENSO cycle is characterized by variation in ocean heat content anomalies along the equator, with a zonal mean component and a zonal asymmetric component, in which the former is the manifestation of charge and discharge of ocean heat content in the equatorial Pacific. In order to verify the mechanism of the model ENSO from the aspect of the recharge oscillator, the empirical orthogonal functions (EOFs) for the zonal ocean heat content along the equator (average of 6°S – 6°N) were calculated. Since finding that the variation of the zonally averaged ocean heat content was out of phase between the equatorial latitudes of 6°S-6°N, and the off-equator (poleward of 6°S and 6°N), the equatorial region was refered to for the model ENSO as those latitudes (6°S-6°N).

Figures 5-4a and 4b present the first and second EOFs, which account for 55% and 33% of the total variance of equatorial ocean heat content. It is obvious that the first mode represents the zonal asymmetric component with an east-west seesaw, and that the second mode represents the zonal mean component with the same sign across the entire basin. The phase relationship between the two modes was examined by a lag correlation between the principal components (PCs) (Fig. 5-4c). The auto-correlation for the PC1 indicates unity at lag=0 (by definition) and minimum values of about –0.5 at around –12 and 12 months, which implies that biennial oscillation is dominant in the model ENSO. Lag correlations of the PCs with SST-NINO3 were also calculated, and it was found that the first mode (i.e., the zonal asymmetric mode) is highly correlated (0.92) and had very little phase lag relative to the SST-NINO3. In that sense, this mode is closely linked to the equatorial SST and is

considered as the SST-dynamics part in the recharge oscillator theory. The second mode (i.e., the zonal mean mode) has a maximum correlation (0.57) six months prior to the first mode and a minimum correlation (–0.76) six months lagging. In view of the recharge oscillator theory, this mode is related to the ocean-adjustment part that acts as negative feedback or a phase transition mechanism. Oscillatory behavior of the two modes, with an approximate 90-degree phase lag in a phase trajectory plot (Fig. 5-4d), was confirmed. This suggests that the two modes of SST, and the charge-discharge of the equatorial heat content, act as negative feedback for phase transition for each other.

Figure 5-5 illustrates geographical distributions of the ocean heat content anomaly corresponding to the two EOFs. The anomaly pattern for the zonal asymmetric mode along the equator (the first mode; Fig. 5-5a) has a maximum anomaly in the eastern equatorial Pacific, and negative anomalies in the western Pacific concentrated at the northern and southern off-equator regions. This pattern reflects the westward thermocline tilt due to the Fast adjustment to westerly wind stress forcing at the equator. Thus, the pattern is in quasi-equilibrium with the wind forcing, since it has little phase lag with the SST pattern and the wind pattern shown in Fig. 5-2.

The anomaly pattern related to the zonal equatorial mode (the second mode; Fig. 5-5b) shows the same sign across the basin with a spindle shape along the equator. This pattern is dominated by the zonal-mean variation of the equatorial heat content, which is associated with the Very Low Frequency mode (Jin 2001) of the tropical ocean adjustment. This pattern is thus not in quasi-equilibrium with the equatorial zonal wind stress, but it is slowly adjusting to the off-equatorial wind stress *curl* in Fig. 5-2b.

The first and second patterns may be reminiscent of Rossby waves (propagating westward) in the off-equatorial western Pacific, and a Kelvin wave (propagating eastward) along the equator, respectively. However, it should be noted that both patterns include components of Kelvin and Rossby waves, and are a result of the interference of these equatorial waves. Therefore, the slowness of this adjustment makes the second pattern (Fig. 5-5b) far behind (~ 6 months) the first pattern (Fig. 5-5a) compared with the time lag that is expected from a free-wave reflection at the western boundary. The above behavior of the ocean heat content pattern is a clear illustration that confirms the recharge oscillator mechanism is at work in this model.

Figure 5-6 depicts temporal evolutions for zonal mean variables related to the SST-NINO3 variation. The evolution of zonal mean equatorial (6°S-6°N) SST is almost identical to the SST-NINO3 variation. The variation of the ocean heat content, averaged for 6°S-6°N, exhibits a maximum peak about 4 months prior to the SST peak. The wind stress *curl* at the off-equator (6°N) has an in-phase variation with the equatorial SST, since it

reflects the instantaneous response of the tropical atmosphere to the SST anomalies, as previously mentioned.

It is believed that the zonally integrated wind stress *curl* anomaly in the off-equator regions will lead to a meridional heat advection change at those latitudes through an anomalous geostrophic current. The variation of the northward heat advection at 6°N possesses a 1-2 month phase lag behind the wind stress *curl* variation, which is consistent with the above assumption. Furthermore, there is a quarter cycle phase lag relative to the ocean heat content variation, which means an out-of-phase relation with the tendency of ocean heat content. A positive anomaly of the northward heat advection at the northern off-equatorial latitudes suggests a contribution to heat content discharge from the equatorial region.

The zonal structure of the variation of northward heat advection is shown in Fig. 5-3d. There are positive (northward) heat advection anomalies in phase with the maximum westerly wind stress (Fig. 5-3b), and positive *curl* at 6°N (Fig. 5-6) over most of the basin, though there is a phase difference between the eastern and western end. The intense anomalies at the western boundary are out-of-phase with the anomalies in the interior basin. This seems to be consistent with the effects of wave reflections at the boundary, for instance, a southward heat advection anomaly is expected from the negative ocean heat content anomaly in the east off the Philippines (Fig. 5-5a).

However, the meridional transport anomaly over the ocean interior makes a larger contribution to the zonally integrated net heat transport than that at the western boundary with the opposite sign in the model ENSO. With a simple coupled model, Zebiak (1989) demonstrated that the meridional heat transport at the western boundary opposes the tendency in the equatorial heat content with a compensating interior transport. Our result is also supported by the suggestion of An and Kang (2000), that the net meridional mass transport variation is accomplished through a competition between the meridional transport over the tropical ocean interior and the east-west boundary fluxes, where the former dominates the latter. This evidence supports the conclusion that a charge-discharge mechanism is at least partially attributable to the wind-driven meridional circulation (or Sverdrup flow) change in the tropical upper ocean.

5.2 Irregularity of the Model's Warm Events

5.2.1 The SST-NINO3 Evolution of Warm Events

The previous section suggested that the oscillation mechanism acting in this model ENSO is consistent with the recharge oscillator paradigm (Jin 1997) from the analyses for the spatial and temporal structure of the variations in SST, ocean heat content, and wind

stress. Next the focus is on why the amplitude of the model ENSO events differs from one event to another, as seen in the time series of the SST-NINO3 in Fig. 5-1.

Figure 5-7 presents a histogram of the peak value of three-month mean SST-NINO3 anomalies for the warm and cold events in the 400-year model integration. The peaks are defined by searching the maximum or minimum for the consecutive 11 months' bins in order to avoid double counting a single event with double peaks. The amplitude ranges from less than –2°C for the cold events, to above +4°C for the warm events. It is remarkable that the peak value distribution is skewed toward warm events compared with a normal (Gaussian) distribution. The observed ENSO also exhibits such skewness in the SST-NINO3 time series (Trenberth 1997), which is considered to be associated with the nonlinearity of ENSO and will be discussed later. Since the cold events in the model ENSO have a smaller range in their amplitude, thus showing less amplitude irregularity. Then the amplitude irregularity is investigated only for warm events.

The total number of the warm events is 151, counting warm events with peaks larger than 1.0°C, which means that the average interval between significant warm events is 2.6 years. A strong events group and a weak events group are selected, with peak values of 3-month mean SST-NINO3 anomalies of greater than 3.0°C and 1.0-1.5°C, respectively. The criteria for choosing them was that the number of events in both groups were close to each other. In the 400-year model integration, 27 events were classified as strong ones and 26 events as weak.

Figure 5-8 shows the seasonal evolutions of SST-NINO3 anomalies for strong and weak events. It is apparent that there is a phase-locking of peaks from September through December. There is no peak in boreal spring (February to June) for the strong events group. In contrast, the weak events tend to have their peaks in relatively diverse seasons, June to the following January. A few events in the weak group have peaks in boreal spring. This implies some relationship between the irregularities of amplitude and the seasonal locking of El Niño. This interesting phase locking behavior will be discussed later.

5.2.2 Lagged Composites for Strong and Weak Events

A set of lagged composite analyses was made to examine the difference between strong and weak events. The composites were made so that their SST-NINO3 peaks came to lag=0, and the temporal evolutions were compared between the composites for the strong events and weak events. The examined fields were zonal averages of SST, zonal wind stress and ocean heat content, in the equatorial band (6°S-6°N), and the off-equatorial wind stress *curl* and northward heat transport in the upper ocean at 6°N latitude (Fig. 5-9). The standard deviations of the composite are also shown for each group as well as the composite averages, in order to evaluate the statistical significance of the difference

between the strong and weak events groups.

The equatorial SSTs (Fig. 5-9a) obviously show a significant difference (90% level) between the strong and weak composites around the peak phase (lags from –4 to 4 months) as a matter of course by definition. The evolutions of equatorial ocean heat content variation exhibit their maximum 4 to 6 months prior to the development of equatorial SST anomalies, and the strong events composite seems to peak slightly earlier than the weak composite. The ocean heat content anomaly about 6 months before the strong events is significantly larger than that before the weak events. The relationship between magnitudes of SST and ocean heat content anomalies is clearly illustrated in Fig. 5-9. At around 12 months before the peak phase (when the equatorial SSTs show minimum), there is a marginally significant difference (70% level) in the equatorial SST and wind stress *curl* between the strong and weak composites. This implies that the stronger warm events tend to have preceding colder events as a precursor. The negative anomalies of wind stress *curl* at the northern off-equator (6°N) regions have larger magnitude prior to the strong events than the weak events, and the difference is marginally significant 12 to 9 months before the peak SST phase (Fig. 5-9a).

The period (lags from –15 months to –6 months) when the equatorial ocean heat content is developing (i.e., positive tendency) can be regarded as the recharge phase in the model ENSO. During the recharge phase, the negative wind stress *curl* anomaly is expected to make an anomalous southward transport at the northern edge of the equatorial band. The meridional heat advection anomalies (Fig. 5-9d) indicate a larger southward heat transport for the strong events than for the weak events, however the difference is not statistically significant. There also seems to be a phase difference at the negative (southward) peak of heat transport, –10 months for the strong, and –13 months for the weak, but the difference is not statistically significant.

After the event, the evolution of the ocean heat content anomaly exhibits different evolutions between strong and weak events after +6 months lag, and a significant difference remains for more than 12 months. The ocean heat content anomaly after strong events stays significantly lower than after weak events. Since the decrease of ocean heat content is much larger for strong events due to the larger discharge of heat content in the equator associated with the stronger atmospheric changes (e.g., the off-equatorial positive wind stress *curl*, Fig. 5-9c), the “overshooting” of the discharge is considered to make the post-event difference. The over-discharged ocean heat content in the equator does not recover until 20 months after the strong events, which may prevent preconditioning for future warm events in successive years. This is possibly why a multi-decadal epoch with strong events (as seen in Fig. 5-1) is more favorable for a longer (3yr - 6yr) period oscillation

rather than a biennial oscillation, at least in this model ENSO.

The variation of meridional heat transport at the northern off-equator (6°N) region indicates a fairly good correlation with the charge-discharge of the ocean heat content in the equator (Fig. 5-6). Figure 5-9d implies a certain contribution of the meridional heat transport to the charge-discharge, but shows little significant difference between strong and weak events, suggesting that it does not provide a sufficient condition for the difference of charge-discharge intensity.

5.2.3 Heat Budgets for Amplitude Irregularity

The variation of ocean heat content is a result of the balance among horizontal and vertical advection, diffusion, and surface heat flux (including penetrative solar radiation), and these variables fluctuate greatly compared to the total heat budget. A heat budget analysis is made for the tendency of ocean heat content in the region bounded by the eastern and western coast and 6°N and 6°S latitudes with a bottom at 300 m depth. Figure 5-11 shows the total tendency and its contributions from horizontal advection, surface heat flux (radiation included), vertical advection at the bottom and residual terms. The composite variations are shown for the strong and weak events groups in the same manner as in Fig. 5-9.

The total tendency is the rate of change of the ocean heat content variation shown in Fig. 5-9b. For strong events, its magnitude is significantly larger both in the recharge phase (–15 to –6 months lags) and discharge phase (–3 to +6 months lags), compared to that for the weak events. The horizontal advection for strong events makes a dominant contribution to the total tendency, and has a significantly larger anomaly in the recharge phase than that for the weak events, while there is no significant difference in the discharge phase.

The contribution from vertical advection exhibits a damping for the total tendency, with a magnitude roughly 40% of that. Yu and Mechoso (2001) suggested a dominant contribution of vertical advection to the building up of subsurface temperature anomalies in the western equatorial Pacific. This does not, however, contradict the present result, since in their analysis the heat budget is calculated separately for surface and subsurface layers, thus reflecting the variation of thermocline zonal gradient as well as gross heat content. The present analysis, on the other hand, calculated the heat budget for the entire upper 300 m of ocean in order to focus on the exchange of gross heat content of the equator.

The surface heat flux makes a positive contribution to the total tendency and has a slightly smaller magnitude than the vertical advection. This suggests that the cooling (warming) due to upwelling (downwelling) is nearly cancelled by the surface flux anomaly. The difference of surface flux between strong and weak events is significant in the discharge phase (0 – 3 month lags). It is suggested that the surface heat flux plays a

relatively larger role for discharge than for recharge, since cooling by the surface evaporation exponentially increases in a warmer SST.

Note that the horizontal advection term (Fig. 5-11b) includes a large part of the transport by the propagation and wave reflection of transient waves as well as the transport by the mean current, since the effects of those waves (including tropical instability waves) are reasonably resolved by the model with a 0.5 degree grid interval near the equator. The residual term includes the heat fluxes due to sub-gridscale mixing at the lateral boundary, and the diffusive flux at the bottom, and is negligible for the variation. In order to evaluate the effects of the model's resolved eddies and wave reflection at the boundary, the transport calculated by the product of monthly mean fields for velocity and temperature is subtracted from the total horizontal advection (Fig. 5-11f). Although the contribution of the transient wave effects is not small and is in phase with the total, there is no significant difference associated with the magnitude of the event in the recharge phase. This suggests that the larger recharge before strong events is mainly dominated by the larger meridional convergence of the mean transport and the larger surface heating.

5.2.4 Precursors in the Recharge Phase

It is useful to compare the meridional anomaly distributions of the associated variables during the recharge phase (average of –15 to –6 months lags), to understand the causes of magnitude differences of ocean heat recharge. For strong events, the zonally averaged ocean heat content tendency (Fig. 5-12a) indicates that the heat build up is larger at the equator, whereas there are only slight differences in heat losses in the subtropics (larger heat loss for strong events), though their differences are not significant.

The zonally averaged surface heat flux (Fig. 5-12b) suggests larger input in the subtropics (23°S-12°S, 12°N-17°N) in the recharge phase of strong events, though there is no significant difference at the equator. The surface heating anomalies in the subtropics are consistent with the westerly wind stress anomalies, which imply a weakening of climatological easterly trade wind and a suppression of evaporative surface cooling. It also implies that the subtropical upper ocean loses energy by charging it into the equator, but it is partly compensated by getting energy at the surface. The energy flow in the model recharge phase is schematically shown in Fig. 5-13. In other words, in the recharge phase of warm events, there is an energy flow from the subtropical atmosphere to the equatorial upper ocean through meridional heat exchange in the upper ocean, and the energy flow is intensified before strong events.

If the Sverdrup flow relation is considered, the meridional distribution of the zonal wind stress has an essentially dynamical effect on the meridional mass transport in the upper ocean. The zonal wind stress anomalies (Fig. 5-12c) near the equator have easterly

anomalies with no significant differences between the strong and weak events. In contrast, in the off-equator to subtropics particularly around 10°N, a larger westerly wind stress anomaly is evident for strong events. The wind stress *curl* anomalies also exhibit differences between strong and weak composites. The negative wind stress *curl* anomaly shown in the northern off-equator region (centered at 5°N) implies the generation of a southward Sverdrup flow, and the positive wind stress *curl* anomaly in the South Pacific implies the generation of a northward Sverdrup flow. The zonally integrated effect of these meridional flow anomalies leads to a convergence of mass into the equator, which lowers the thermocline and increases the heat content at the equator. It is suggested that the larger heat recharge is related to the larger wind stress *curl* anomaly in the northern off-equator region. In the southern Pacific, on the other hand, there is no significant difference in the wind stress *curl* anomalies associated with the strength of events, which suggests little contribution from the heat transport from the south, at least in relation to the magnitude irregularity in the model ENSO.

It is an interesting topic to investigate whether or not similar differences are seen for the observed El Niño events, which have been shown for the recharge phase in the model ENSO. Although, there are too few observed events to support a statistical discussion, the Florida State University pseudo wind stress data, based on the observation for 1980-1999 (Legler et al. 1989), and the surface heat flux from NCEP/NCAR reanalysis (Kalnay et al. 1996) are used. The 1982 and 1997 events are selected as strong El Niños, and the 1987 and 1992 events as weak El Niños. As in the model ENSO, the periods from 15 to 6 months before the observed SST-NINO3 peak phase are assumed to be the recharge phase.

Both the 1982 and 1997 El Niños exhibit the zonal wind stress anomaly (Fig. 5-14a), with positive anomalies at around 10°N and negative anomalies in the equator through the southern tropical Pacific, and the wind stress *curl* distribution (Fig. 5-14b) with negative anomalies near the equator through 10°N. These meridional structures of zonal wind stress anomalies agree with those for the model, implying an effective recharge of heat into the equator. For the 1987 and 1992 El Niños, however, such meridional structures are not robust; rather those in the northern off-equator zone appear to possess opposite signs. It is found that the typical structure of the wind stress anomaly for the heat recharge into the equator is significant, particularly for the 1982/83 El Niño.

The anomalies of surface heat flux (Fig. 5-14c) do not exhibit the typical meridional distribution as seen in the recharge phase of the model ENSO. However, it cannot be concluded that the surface heat flux has little contribution from this result, since the surface heat flux data from the reanalysis is not based on direct observation, but is dependent on the response of the atmospheric model to SST anomalies, and the reliability has not been

sufficiently verified.

Figure 5-15 depicts the geographical distribution of wind stress *curl* in the recharge phase for the observed 1982/83 and 1997/98 El Niños together with the composite for strong events in the model. It is notable that positive anomalies are dominant in the region northward of 10°N, and negative anomalies are dominant in the equator through 10°N, for both the observed and model wind stress. Compared to the 1982/83 El Niño, the distribution for the 1997/98 El Niño has less similarity with that of the model, though there is a notable positive anomaly in the western North Pacific around 10°N-20°N, the same as for the 1982/83 El Niño.

5.2.5 The Irregularity of Phase Locking

The previous section demonstrated that the model adequately simulated the peak phase of the equatorial Pacific SST anomaly (Fig. 5-8) tending to appear in the preferred season, specifically September through December. Furthermore, there is an irregularity of the phase-locking behavior closely related with the amplitude of the events. Figure 5-16 presents the histogram of the simulated warm events (with amplitude exceeding 1.0°C) relative to the calendar months of the peak. A large number of peaks is simulated in September through December, and there is a secondary mode in May, which can be categorized as early-peak events. To examine the differences in the condition of event evolutions associated with the different peak seasons, The events are classified into two groups: normal-peak events, with their peaks in September through December, and early-peak events, with their peaks in May through August. The normal-peak group contains 87 events, and the early-peak group contains 14 events.

Figure 5-17 illustrates the composite evolutions of the equatorial SST and ocean heat content anomalies, for the normal- and early-peak events. There is little difference in the onset timing of the SST anomaly between the normal- and early-peak events. However, the development of the SST anomaly for the early-peak events is suppressed after July, while that for the normal-peak events is sustained until November, and leads to the larger SST peak anomaly. The early-peak events possess a broader peak phase than the normal-peak events. A similar feature is seen for the observed El Niños, as pointed out by Neelin et al. (2000), though they categorized it as early-onset rather than early-peak. The evolution of ocean heat content for the early-peak events has slightly earlier onset (~ 1 month) and earlier peak (~ 1 month) than the normal events, and a sharp decrease after April. It is interesting to note that the magnitude of the ocean heat content anomaly for the early-peak events is larger, even though the SST peak is significantly smaller, compared to those for the normal events.

A heat budget analysis was made for the variation of the equatorial ocean heat

content for each composite (not shown). It was found that the variation of horizontal advection with the mean current is the dominant term and that the relations between other terms are also similar to those shown in Fig. 5-11, except that the evolutions are earlier after April for the early-peak events relative to those for the normal-peak events. Xie (1995) demonstrated in a pair of OGCM experiments that the SST anomalies in the eastern equatorial Pacific are larger when the thermocline depth anomaly peaks in boreal fall than when it does in boreal spring, in response to identical wind forcing and thermocline anomalies. The present result seems to be supported by Xie's conclusion that the ocean thermodynamics (SST equation) contains a nonlinearity that tends to produce larger SST variability in boreal fall/winter, than in spring.

5.3 Summary and Discussion

The irregularity of El Niño was investigated with a 400-year simulation of a coupled GCM. The model simulated ENSO variability with reasonably realistic spatial structure and temporal evolution. The simulated maximum SST anomaly in the NINO3 region ranged from 1°C to 4°C. The temporal phase relationships, between the variation of SST, wind stress and ocean heat content in the tropical Pacific, are consistently explained with the recharge oscillator theory proposed by Jin (1997). It was shown that the zonally averaged ocean heat content anomalies are exchanged between the northern subtropics and the equatorial region, and the maximum phase of the equatorial ocean heat content anomaly precedes that of the SST anomaly at the equator, while the wind stress anomaly is almost simultaneously linked with the SST anomaly.

The variation of the equatorial ocean heat content possesses two distinct dominant modes. The first is a zonal asymmetric variation that explains the variation of east-west tilt in the thermocline depth, and the second explains the variation of the zonal mean ocean heat content. The spatial pattern of the ocean heat content variation, related to these two modes, suggests the Fast adjustment mode and the Very Low Frequency mode (Jin 2001) associated with the recharge oscillator mechanism.

The equatorial ocean heat content anomaly is charged (discharged) coherently with equatorward (poleward) zonally integrated anomalous heat transport in the upper ocean. The variation of meridional heat transport is consistent with the Sverdrup flow change implied from the wind stress *curl* forcing in the off-equator region. It is suggested that the meridional structure of the wind stress *curl* anomaly near 6°N, reflecting the wind anomaly near 10°N associated with the atmospheric response to the equatorial SST anomaly, is important for the effective recharge-discharge.

It was found that the variation of northward heat transport at 6°N lagged behind the

variation of the wind stress *curl* by 1-2 months (Fig. 5-6). This phase difference is thought to be an oceanic adjustment time through off-equatorial Rossby waves to the wind variation. It is noted that the observed wind stress *curl* variation has a slightly broader latitudinal extent (Fig. 5-14b) that would make the phase difference longer. Consistent with this meridional distribution of the wind variation, the model exhibits a slightly narrower latitudinal extent for the variations of ocean heat content and SST than for the observed one. Since the meridional extent of the ocean heat content variation is smaller than observed, the required time for the heat charge becomes shorter even though there was the same meridional transport. It is thought that that the period of the model ENSO also depends on the strength of the negative feedback associated with the meridional transport that includes the effect of wave reflections.

The variation of zonal mean convergence of the meridional transport is dominated by the change in the ocean interior current, though it is mostly cancelled by the effects of Rossby wave reflection at the western boundary as implied in Fig. 5-3d and Fig. 5-6. This feature agrees with the suggestion by An and Kang (2000) in their simple model. If the efficiency of Rossby wave reflection is underestimated in the model, the stronger negative feedback (due to the weaker cancellation against the mean meridional transport) may lead to a shorter timescale oscillation. These differences are consistent with the generally shorter period of the model ENSO compared to the observed ENSO. However, identifying the causes for the model's shorter ENSO timescale is a complicated problem, and should be studied in the future.

The amplitude irregularity for the model warm events was examined by comparing composites for the strong and weak events. It was found that a larger amount of heat is built up in the equatorial upper ocean as a precursor of stronger events. This result agrees with the analysis by Meinen and McPhaden (2000), for the observed ENSO, which showed that the largest heat content anomaly in the equator was found before the 1997/98 strongest El Niño during the analyzed period. The heat budget analysis suggests that the larger building-up of the heat content anomaly is primarily due to the larger equatorward heat transport by horizontal advection associated with a wind stress *curl* anomaly in the off-equator region. The surface heat flux anomaly is a secondarily important contribution for the building-up of the equatorial heat content in the recharge phase, whereas it is relatively more important in the discharge phase.

The magnitude of the SST anomaly is nonlinearly proportional to the preceding equatorial ocean heat content anomaly. It is noted that there is an interesting asymmetric relationship between the anomalies of SST and ocean heat content, in which positive SST anomalies (warm events) reach larger magnitudes than negative SST anomalies (cold

events) for a given magnitude of ocean heat content, as shown in Fig. 5-10. This feature also agrees with the observed ENSO (Meinen and McPhaden 2000).

Why strong events are strong and weak events are weak is an essential question in the model ENSO. The analysis from Fig. 5-9 indicates that for strong events, everything is larger, and for weak events, everything is smaller in amplitude. One possible explanation is that nonlinearity is inherent to the ENSO system with its chaotic behavior. If there is a very small (but statistically detected) difference in the pre-conditioning phase, it possibly amplifies due to the nonlinearity of the ENSO system and leads to the large difference at the peak phase.

It is not easy to answer what is nonlinearity in the model ENSO in a highly complex CGCM. Recently, Hannachi et al. (2003) evaluated the nonlinearity of the model ENSO for many CGCMs. They used statistics for the amplitude relationship between thermocline depth anomaly and SST anomaly at the equator and the skewness of probability density distribution of the NINO3 SST. They pointed out that the nonlinearity is generally underestimated in the majority of the models. For our model, however, the amplitude relationship (Fig. 5-10) exhibits nonlinearity, and the SST peak distribution is remarkably skewed, as shown in (Fig. 5-7). This qualitative evidence implies that nonlinearity plays a key role in amplitude irregularity in the model ENSO.

An alternative candidate for the cause of the amplitude irregularity is the forcing that is external to the ENSO system (against the intrinsic ENSO system). The forcing may include a stochastic high frequency forcing (such as westerly wind bursts), and a forcing from the outside of the equatorial Pacific Ocean (i.e. the extratropical Pacific and/or Indian Ocean). The external forcing enhances (suppresses) the events in the pre-conditioning phase or the developing phase or both, and results in larger (smaller) amplitude at the peak phase than the inherent amplitude. This explanation is plausible for two reasons. (i) The differences between strong and weak events can be traced back to before the SST warming, when there is no significant difference in the ocean heat content at the equator (Fig. 5-9b). (ii) Significant differences are seen only in the subtropics (Fig. 5-12). Both the nonlinearity and the external forcing are believed to induce the irregularity, though it is difficult to evaluate which contribution is dominant.

During the recharge phase of the observed strong El Niños in 1982/83 and 1997/98, the spatial structure of the wind stress anomalies was consistent with the model result, in which the wind stress *curl* exhibited negative anomalies in the northern off-equator region, and positive anomalies further north, particularly in the western North Pacific. It is difficult to evaluate the reliability of this agreement because there are very few observed samples.

At present, it is still uncertain what causes this difference of the wind anomaly in the

recharge phase. However, in the subtropical western Pacific, there is a climatologically large amount of precipitation, and its interannual variability is also large. We posit that atmospheric circulation anomalies in the subtropical western North Pacific may play a key role in the modulation of preconditioning. In the studies about intrinsic ENSO mechanisms with simplified or theoretical coupled models, these variations have been regarded as stochastic forcing or weather noise. However, there is a connection (which may not be robust, but which has a certain level of statistical significance) between the subtropical western Pacific wind stress *curl* and the tropical oceans, through the influence of ENSO. For instance, it has been widely noted that the interannual variation of the Asian summer monsoon is influenced by the El Niño during the preceding winter (e.g. Shukla and Paolino 1983). A number of hypothetical mechanisms have been proposed for that linkage (e.g. Krishnamurthy and Goswami 2000). Furthermore, there is an interdecadal modulation of the Asian summer monsoon - ENSO coherency, which was pointed out by Torrence and Webster (1999), Krishnamurthy and Goswami (2000) and Kinter et al. (2002). In the meantime, Kawamura et al. (2001) suggested a possible teleconnection from the Asian summer monsoon variation to the atmosphere-ocean variations in the subtropical western Pacific. By forcing a Cane-Zebiak model with a heating in the Asian monsoon region that is correlated with the tropical Pacific SST, Chung and Nigam (1999) found that the Asian monsoon heating modulates the ENSO variability (although their coupled domain is limited in the 20°S-20°N latitudes). These studies imply that there is a possible feedback mechanism in the ENSO-monsoon system.

With regard to the feedback process associated with variation in the off-equator regions, on the other hand, Weisberg and Wang (1997) proposed a hypothesis for the ENSO oscillation paradigm, which emphasizes the importance of the off-equatorial SST anomaly in the western Pacific induced by wind forcing in response to the SST anomaly in the east-central equatorial Pacific.

It is believed there is a potential predictability for the magnitude of El Niño, with the precursors shown in this study, through a certain feedback mechanism such as ENSO-monsoon feedback. However, the feedback mechanism is probably complicated and may not be robust, since, as a matter of course, the Asian monsoon reflects the land surface condition over the Asian continent; moreover, the atmospheric circulation at subtropical latitudes is easily influenced by midlatitude atmospheric dynamics.

The phase locking of peak phase of ENSO to the end of the calendar year is widely known (e.g. Rasmusson and Carpenter 1982), however, the mechanism is not yet fully explained. Some studies attributed it to the seasonality of coupled instability (e.g. Tziperman et al. 1998; Galanti and Tziperman 2000), suggesting that the coupled instability

reaches its minimum at the end of a calendar year. Penland and Sardeshmukh (1995) suggested that the phase locking is due to seasonality in the stochastic noise forcing. Alternatively, Neelin et al. (2000) revealed the scattered phase-locking behavior of the observed ENSO, and investigated its mechanism with two different complexity coupled models. They suggested that the phase locking is due to a nonlinear interaction between the inherent ENSO cycle and the annual cycle, and argued that the scatter of the phase locking can be induced by the variation of nonlinearity. They also showed that the behavior becomes realistic when atmospheric stochastic forcing is included.

It has been shown that our model reasonably reproduces the phase locking and its irregular behavior. The strong events tend to have their peaks in September through December, while the weak events have their peaks in more diverse seasons (Fig. 5-8). If it is accepted that the phase-locking mechanisms are due to the seasonality of the coupling instability, it may explain the relationship between amplitude and phase locking in the model ENSO. The events whose peak phases arrive at the time of minimum coupled instability can develop significantly, otherwise the development of the event will be suppressed.

It is also possible to explain the relationship by the differences of nonlinearity as proposed by Neelin et al. (2000). When warm events are strong, it has to be more nonlinear. Since the phase locking is possible only if nonlinearity is sufficiently strong, it is natural that strong events are phase locked due to strong interaction with the seasonal cycle. The small amplitudes of weak events mean that the nonlinear processes are less important. Thus, it is hard for the phase to be seasonally locked, and the phase tends to spread.

These explanations are consistent for the simulated phase-locking behavior. However, it is more difficult to evaluate the variation of coupling instability and nonlinearity in the full CGCM than it is in simplified models. A composite analysis for the early-peak and normal-peak events, revealed no significant indication of the cause except for the earlier evolution of the equatorial ocean heat content for the early-peak events. Phase locking is probably sensitive to the small differences of parameters such as nonlinearity and external (stochastic) forcing. One way to confirm the above argument is to conduct some additional experiments, for example, to run the model with different external forcing, which should be considered in another paper.

A possible linkage, between frequency modulation and amplitude modulation, is implied for the model ENSO. The model generally exhibits dominant biennial oscillation. However, the lower frequency, with 3 - 6 year intervals, appears more dominant in the periods with larger amplitude events. A similar magnitude-frequency relationship in ENSO was pointed out by Zebiak and Cane (1987). In their simple coupled model, a stronger

atmosphere-ocean coupling induced larger oscillations with a longer timescale.

It can be deduced that the linkage was as follows. Since the ocean heat content is over-discharged from the equator during strong events, the post-event condition of the equatorial upper ocean is maintained for a longer time, which retards the build-up of the ocean heat content anomaly for the next warm event. If the recharge phase is retarded, the development phases of the following events do not occur in a season with a coupling strength favorable for development. That results in missing the quasi-biennial interval of the events.

Since the above explanation is based on a statistical feature, there are some exceptions, for instance, the warm event in the 73-74 model year is immediately followed by another strong event, even though there is a strong discharge of the equatorial ocean heat content (Fig. 5-1). The differences are examined, between the multi-decadal period with low frequency (105-127 and 160-175 model year), and the rest of the period (not shown), and no significant difference were found, in the climatological background or pre-conditioning phase, to indicate the cause of the frequency difference. The cause of these irregularities may be difficult to identify by examining individual events one at a time, since it is related to the chaotic behavior of the model ENSO induced by the nonlinearity. Some additional experiments may be useful, for instance, to run the model with a forcing (or some parameter change) that can alter the dominant period of the model ENSO, which should be considered in a future study.

We are interested in improving the quantitative accuracy and the reliability of El Nino forecasts, by searching for a precursor to the magnitude of an expected warm event. The present analysis has shown that the precursor signals in the recharge phase of following events have a moderate significance level (70%). However, the information, even at this significance level, is useful for probability forecasts. Furthermore, the information gives useful suggestions as to the key factor for improving the forecasting skills of the model.

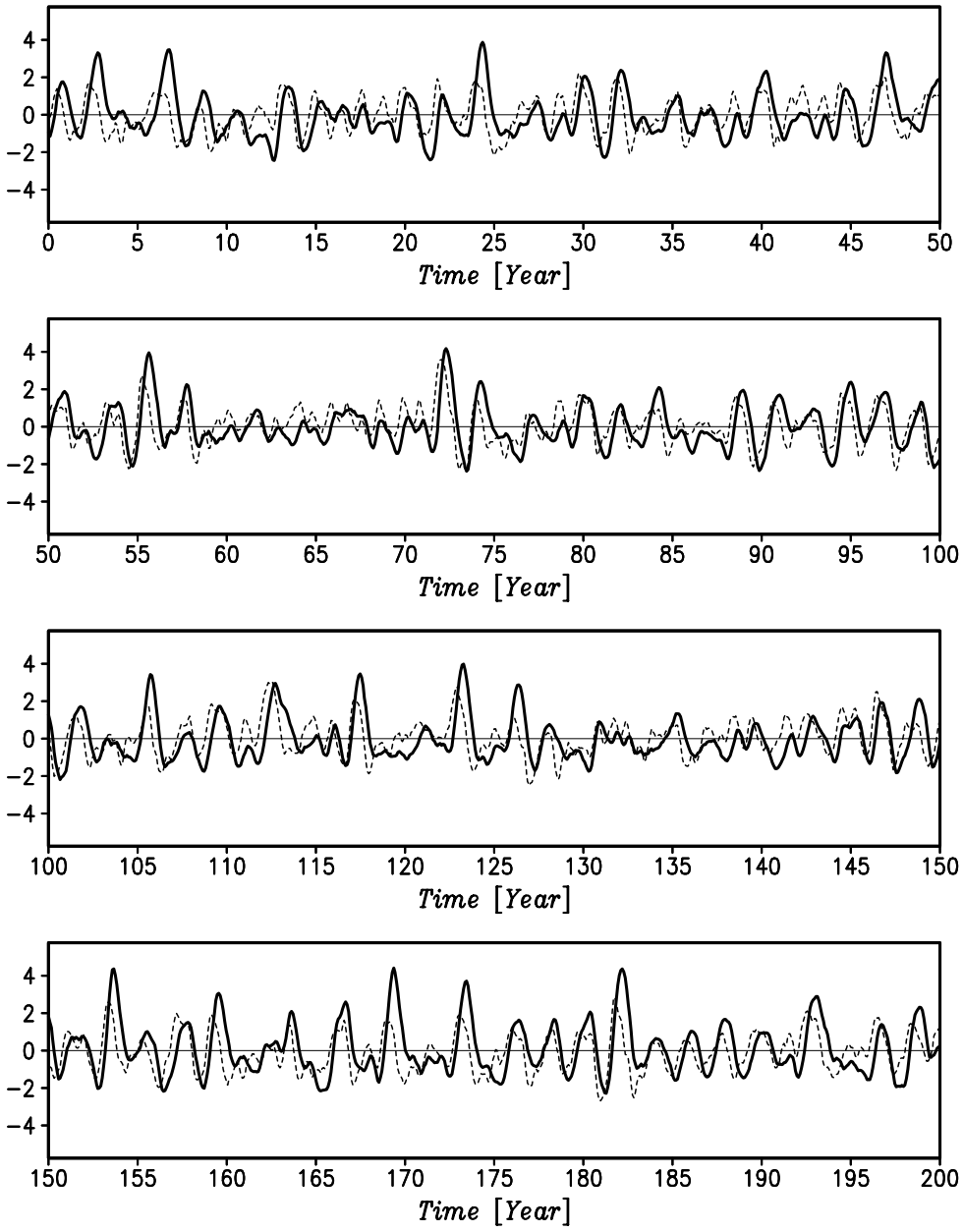

Figure 5-1 Time series of the SST anomaly averaged in the NINO3 region (150°W–90°W, 5°S–5°N) (solid line) and VAT300 anomaly in the equatorial Pacific (120°E–80°W, 6°S–6°N, dashed curve) for the first 200 years of the 400-year simulation of the model.

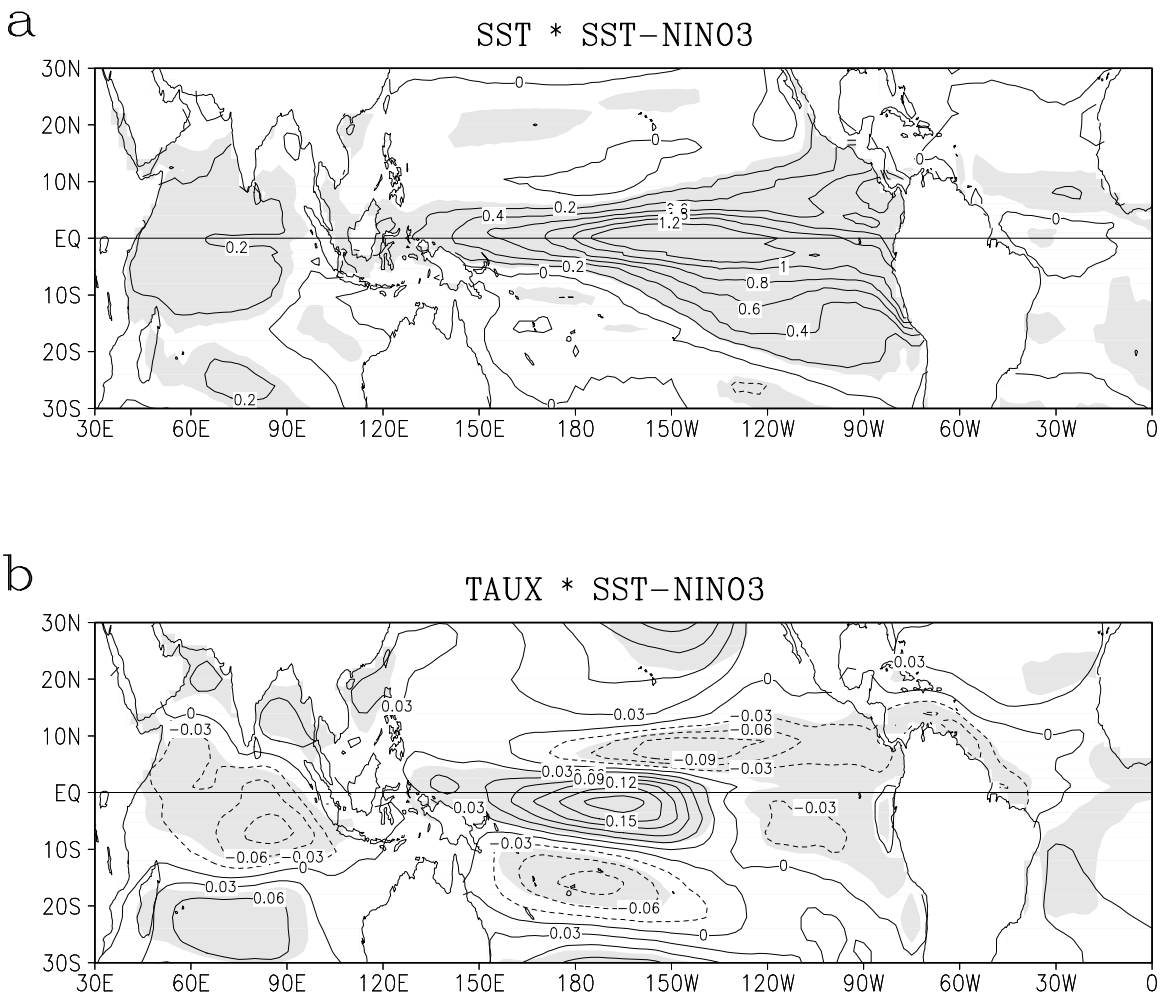

Figure 5-2 Geographical distributions of (a) SST anomaly, (b) zonal wind stress anomaly at the peak phase of the model El Niño, by the linear regression on the SST-NINO3 index. Values are standard deviations in units of (a) K and (b) 10^{-2} Pa. Shading denotes the regions with significance levels higher than 99%.

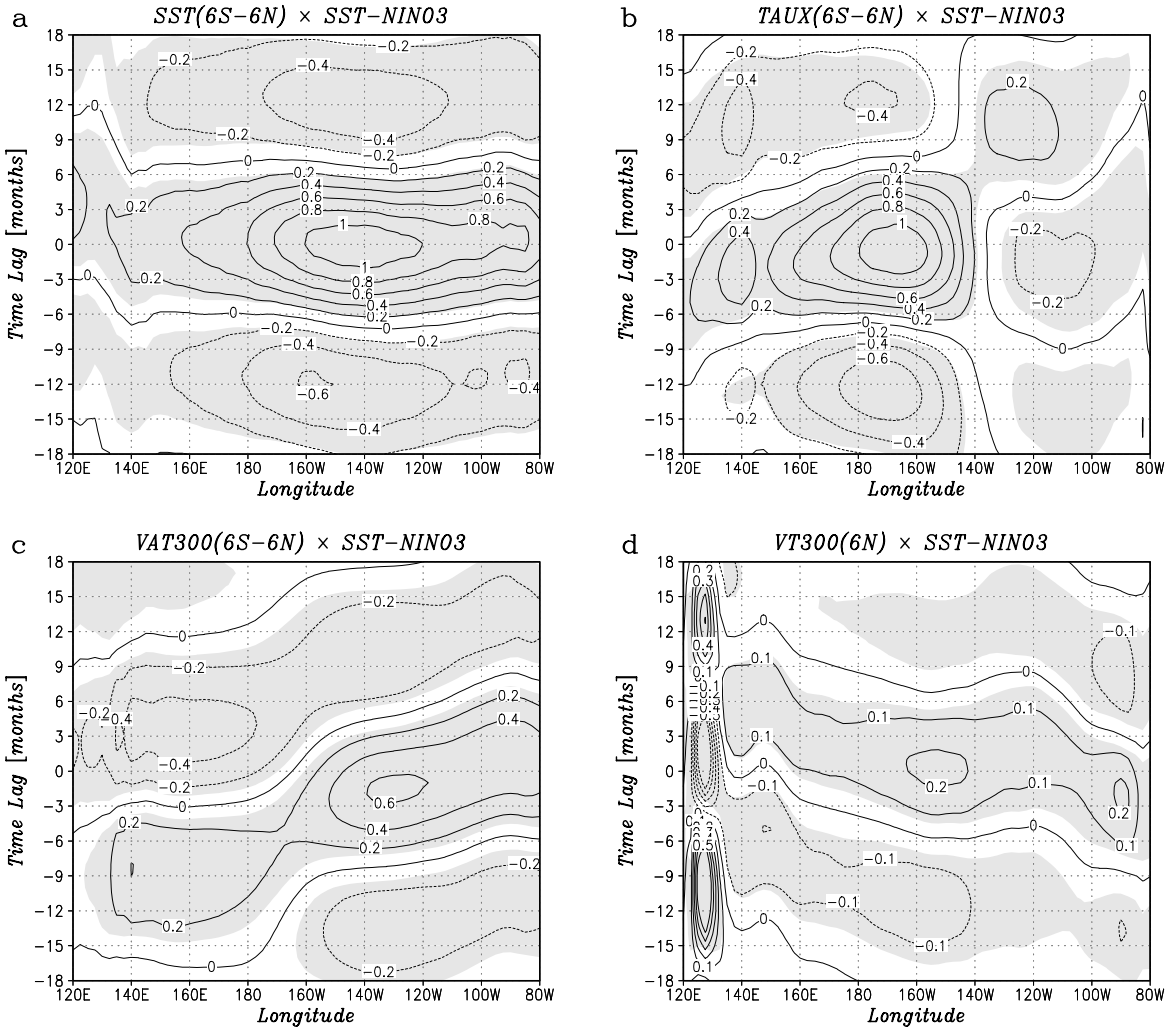

Figure 5-3 Longitude-time variations relative to the SST-NINO3 variation, for the (a) SST, (b) zonal surface wind stress, (c) VAT300 along the equator (average of 6°S-6°N), and (d) northward heat advection in the upper ocean (0-300m) along 6°N latitude. Values are standard deviations in units of (a) K, (b) 10^{-3} Pa, (c) K and (d) PW. Significance levels higher than 99% are shaded.

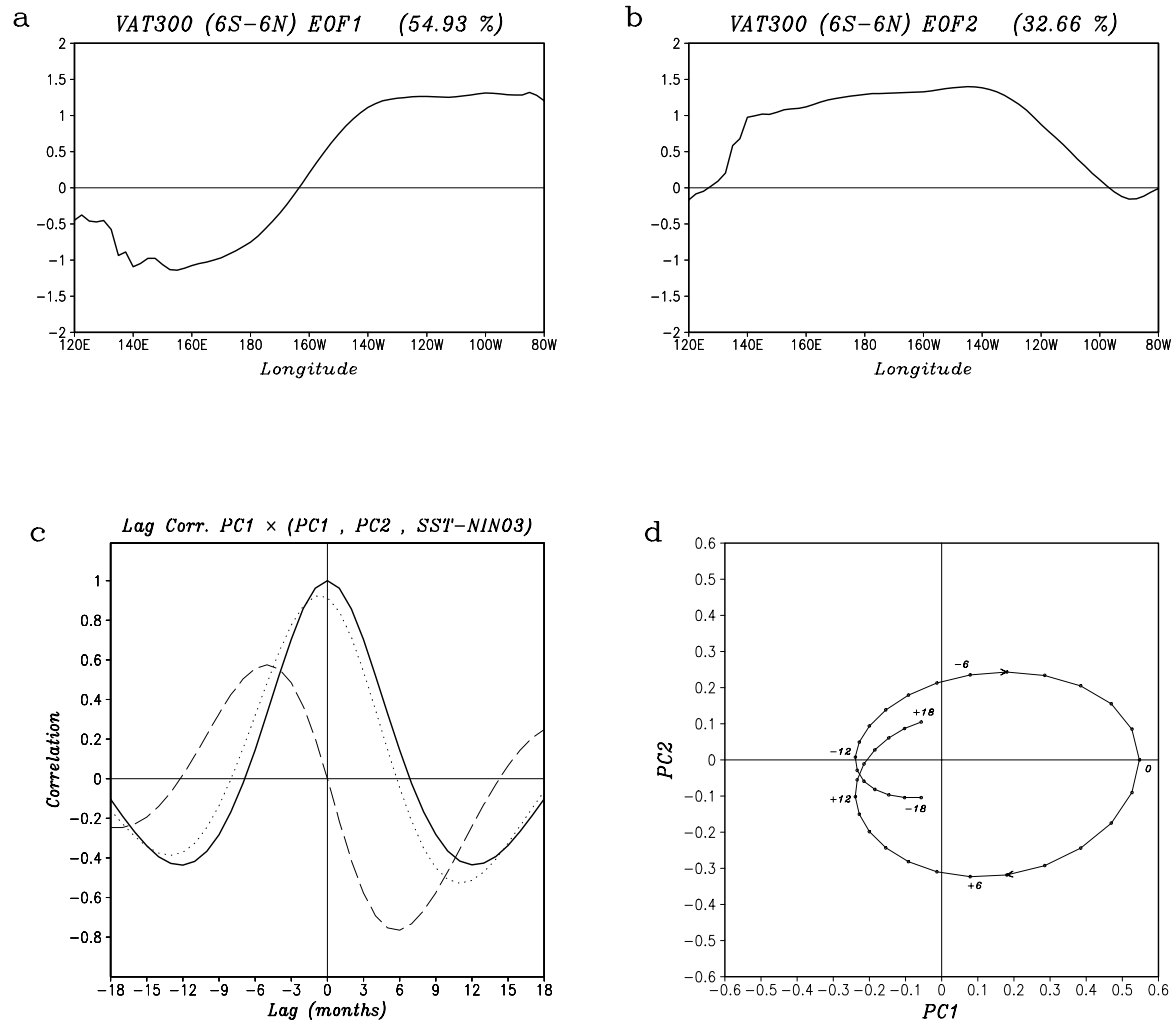

Figure 5-4 Longitudinal distribution of the EOF of the variation of VAT300 along the equator (average of 6°S-6°N) for the (a) first and (b) second modes. (c) Phase relations of the temporal evolution for the first mode principal component (PC1, solid line), second mode (PC2, dashed line) and SST-NINO3 index (dotted line) relative to the PC1 with lagged correlations, and (d) phase trajectory plot for the PC2 versus PC1.

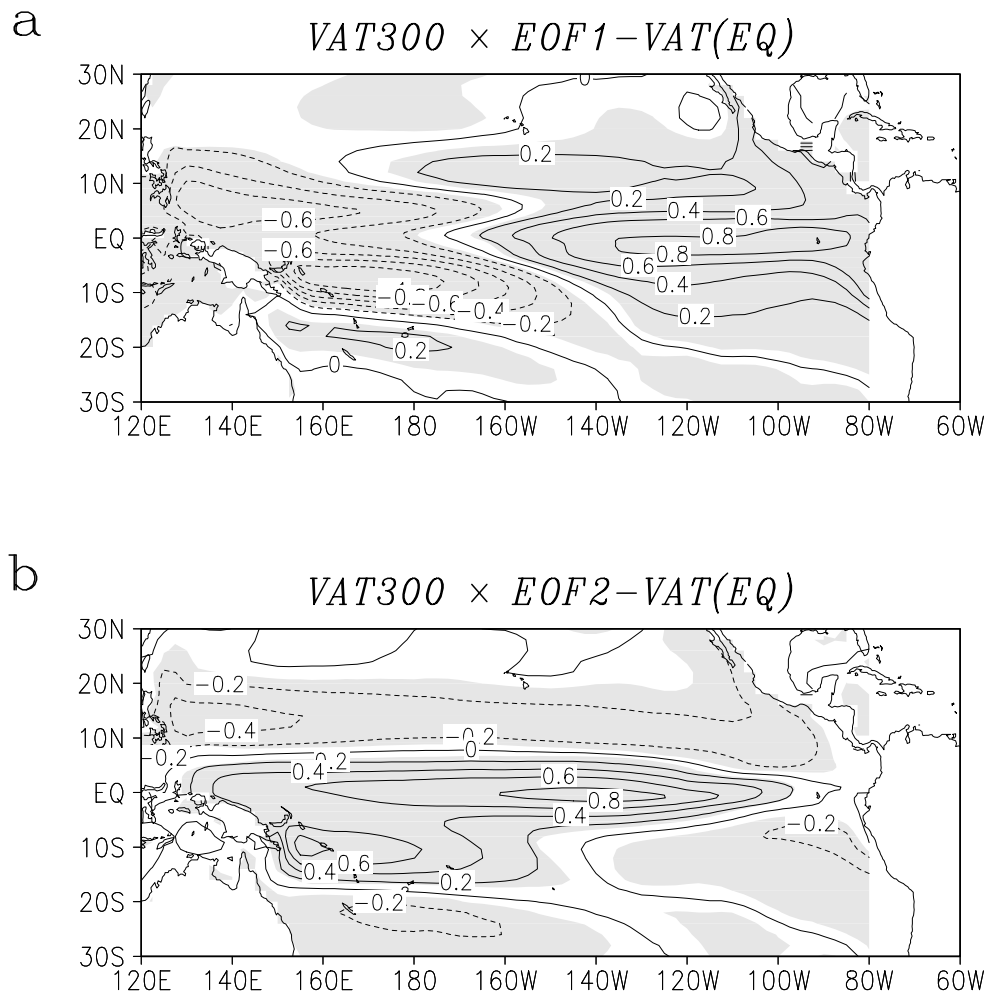

Figure 5-5 Geographical distributions of VAT300 anomaly corresponding to the (a) first mode and (b) second mode of the EOF of the equatorial VAT300, based on linear regressions on the PCs time series. Shading denotes the regions with significance levels higher than 99%.

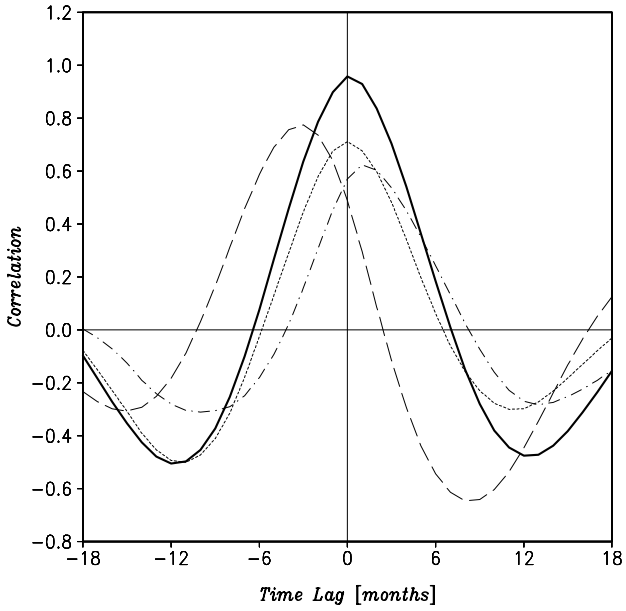

Figure 5-6 Temporal evolutions of the zonally averaged SST (solid line), VAT300 (dashed line) in the equator (average of 6°S-6°N), respectively, and wind stress *curl* (dotted line) and northward heat advection (dash-dotted line) at the 6°N latitude. Values are lagged correlation relative to the SST-NINO3 index.

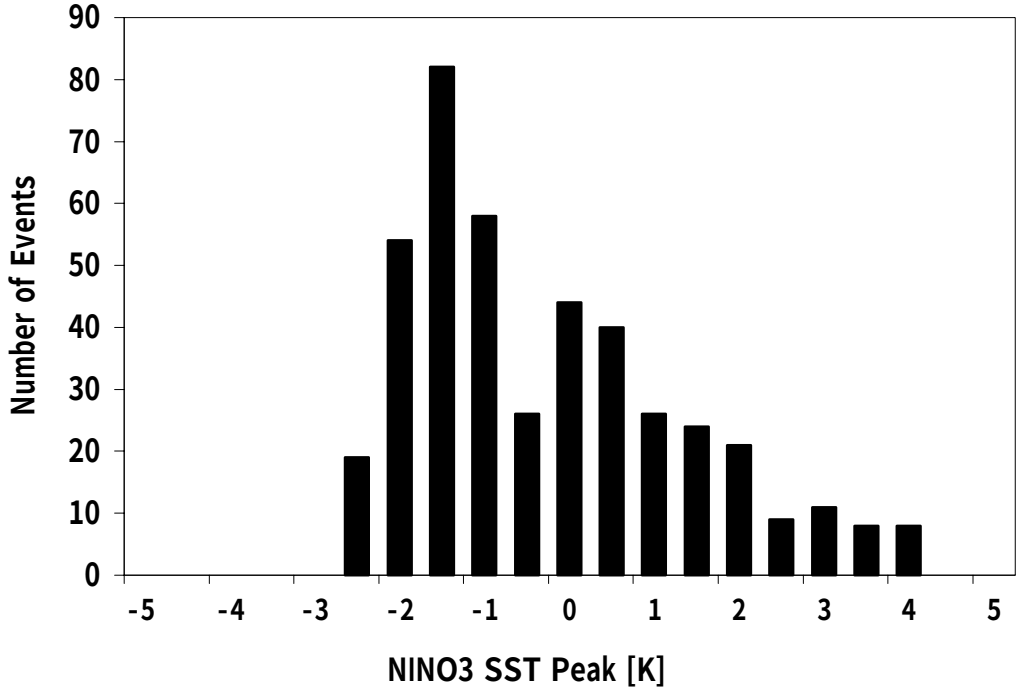

Figure 5-7 Histogram of the distribution of the peak value of SST-NINO3 anomalies for the simulated ENSO events. The peaks are determined by searching for the maximum or minimum in the consecutive 11 months bins in the 400-year model integration.

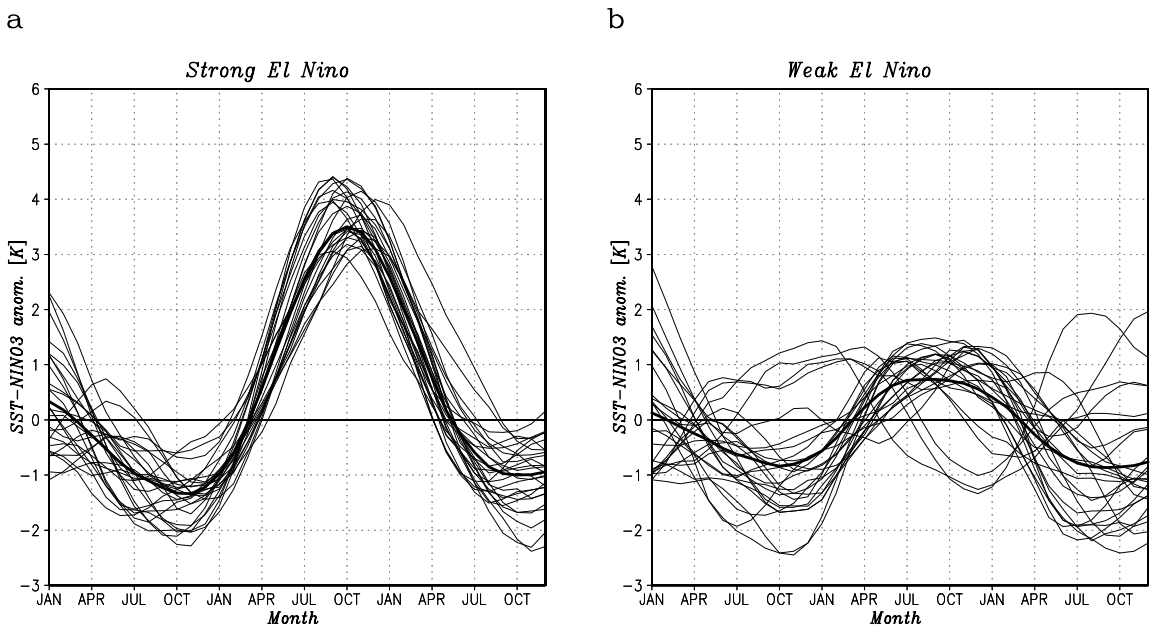

Figure 5-8 Seasonal evolutions of the SST-NINO3 anomalies superimposed for the (a) *strong* warm events and (b) *weak* warm events. Thin curves indicate the evolutions of individual events and thick curves indicate their averages.

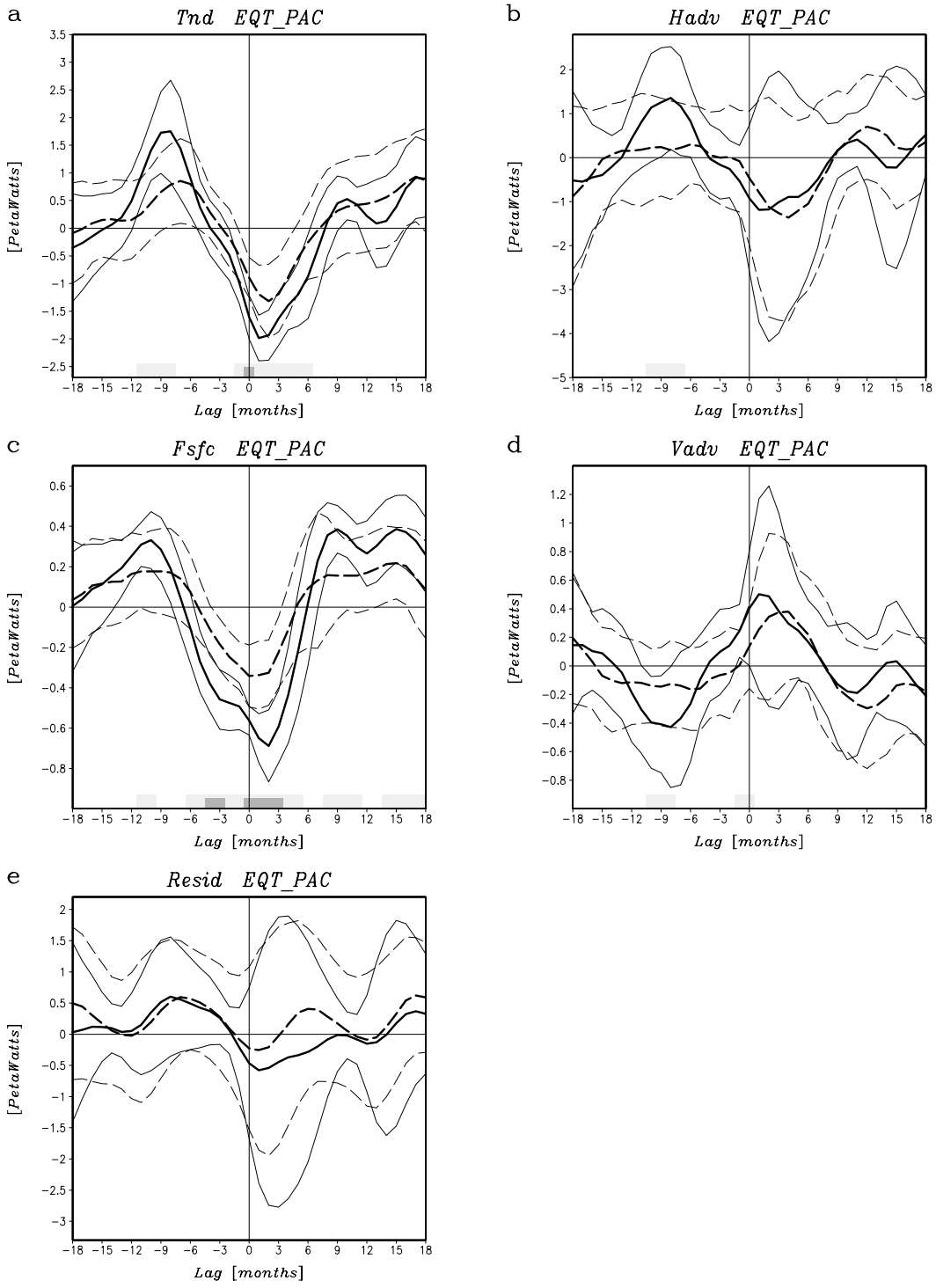

Figure 5-9 Temporal evolutions of zonal-mean (120°E-80°W) anomaly composites compared between the strong events (solid lines) and weak events (dashed lines) for the (a) SST and (b) VAT300 in the equator (6°S-6°N), and (c) wind stress *curl* and (d) northward heat advection at 6°N. Standard deviations among the composites are indicated with thin lines. Differences between the composites with significance levels higher than 70% (light bars) and 90% (dark bars) are indicated on the time axis.

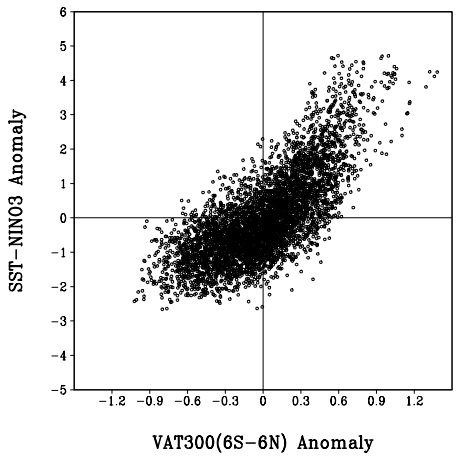

Figure 5-10 Scatter diagram for anomalies of the SST-NINO3 versus the equatorial VAT300 (6°S-6°N). The VAT300 time series is shifted to lag 4 months relative to the SST-NINO3 time series.

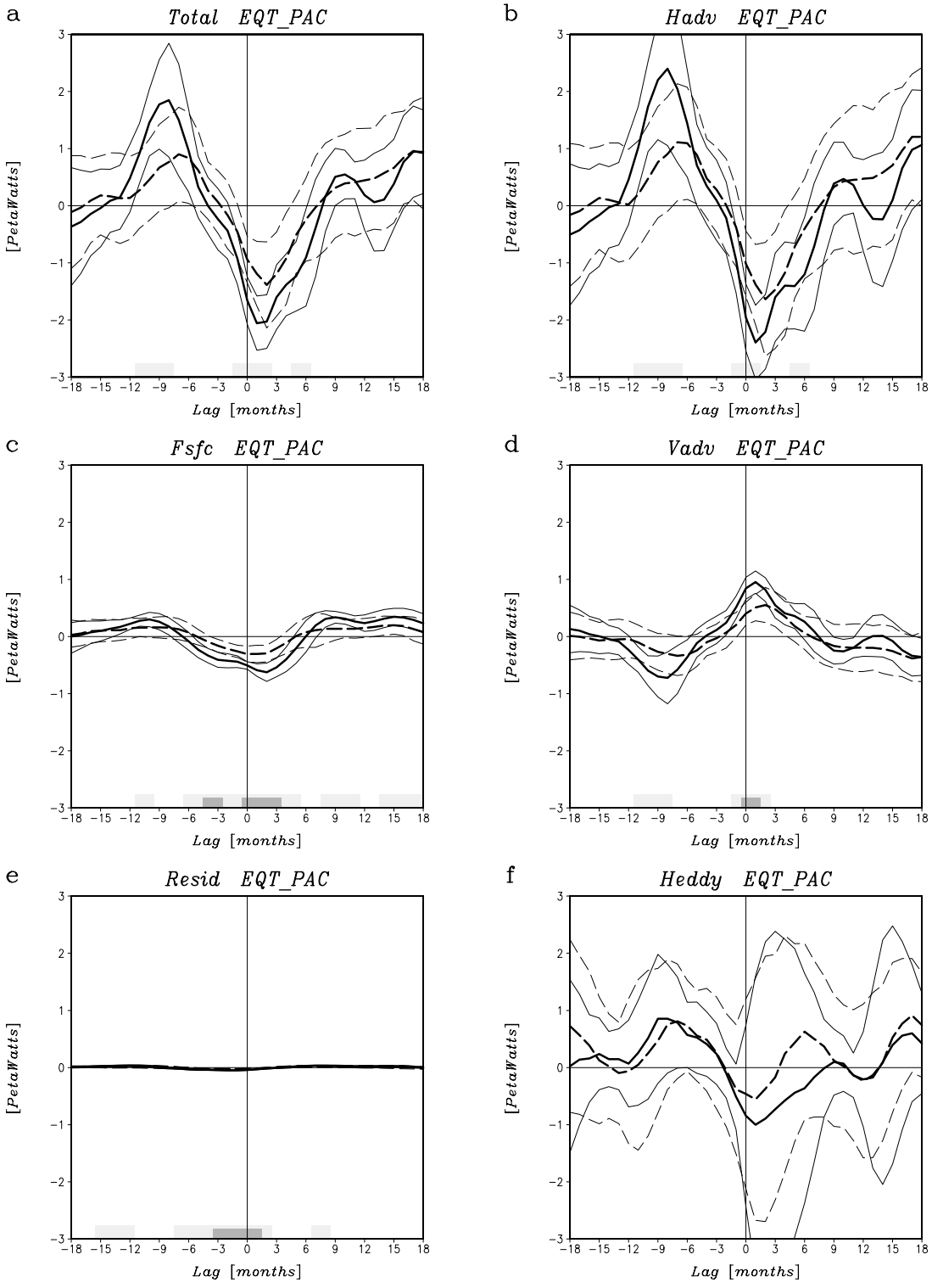

Figure 5-11 Temporal evolutions of anomaly composites of heat-budget terms for the VAT300 of the equatorial (6°S-6°N) Pacific region. Solid (dashed) lines indicate composites for the strong (weak) events. Standard deviations among the composites are indicated with thin lines. Differences between the composites with significance levels higher than 70% (light bars) and 90% (dark bars) are indicated on the time axis.

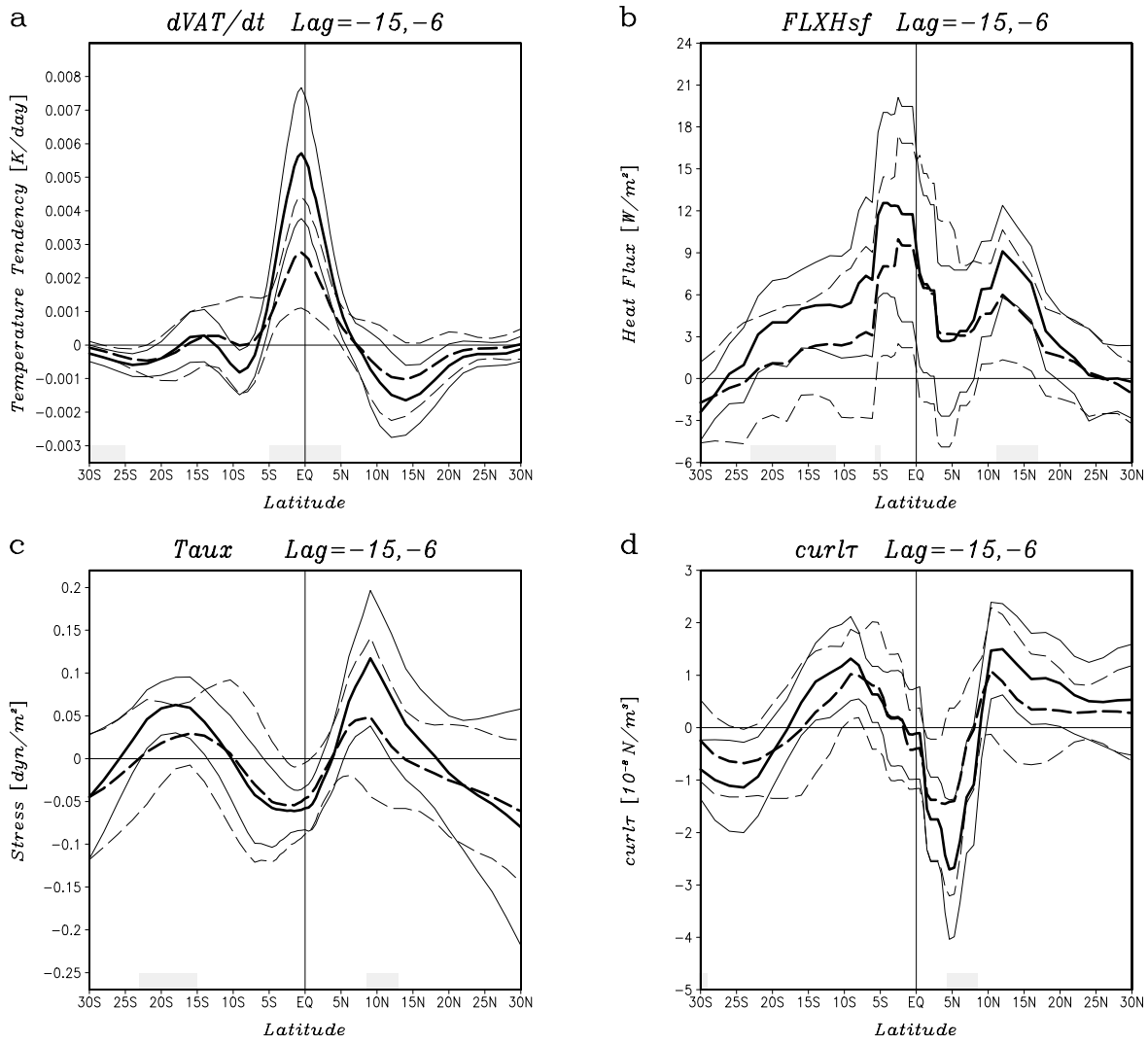

Figure 5-12 Meridional distributions of anomalies zonally averaged over the Pacific region (120°E-80°W) for (a) tendency of VAT300, (b) surface heat flux and (c) zonal wind stress at the equator (6°S-6°N), and (d) wind stress *curl* at the 6°N, in the recharge phase (average for 15 to 6 months before the SST-NINO3 peaks), for the *strong* events composites (solid lines) and *weak* composites (dashed lines). Standard deviations among the composites are indicated with thin lines. Differences between the composites with significance levels higher than 70% (light bars) are indicated on the time axis.

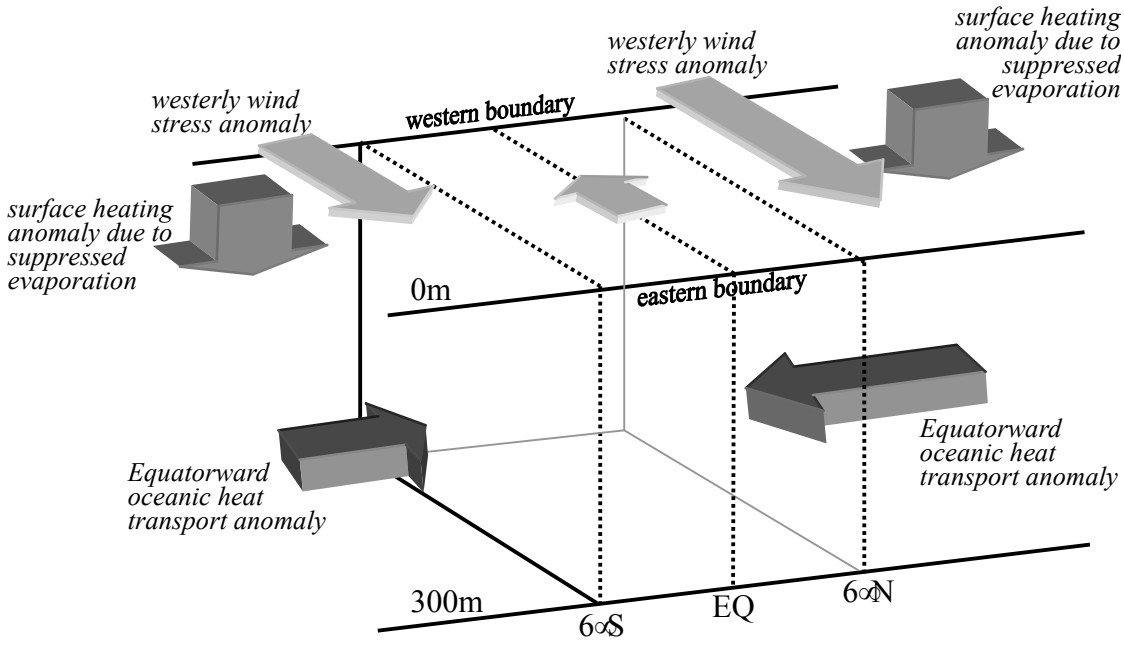

Figure 5-13 Schematic diagram of the energy flow anomalies in the model recharge phase. In the recharge phase, there is an equatorward heat transport anomaly in the upper ocean due to a slow oceanic adjustment, which is partly compensated by an anomalous surface heating (suppressed evaporative cooling) due to the weakened easterly in the subtropics. The equatorward heat transport anomaly at the northern boundary (6°N) dominates the variation of total heat budget of the basin-wide equatorial upper ocean heat content.

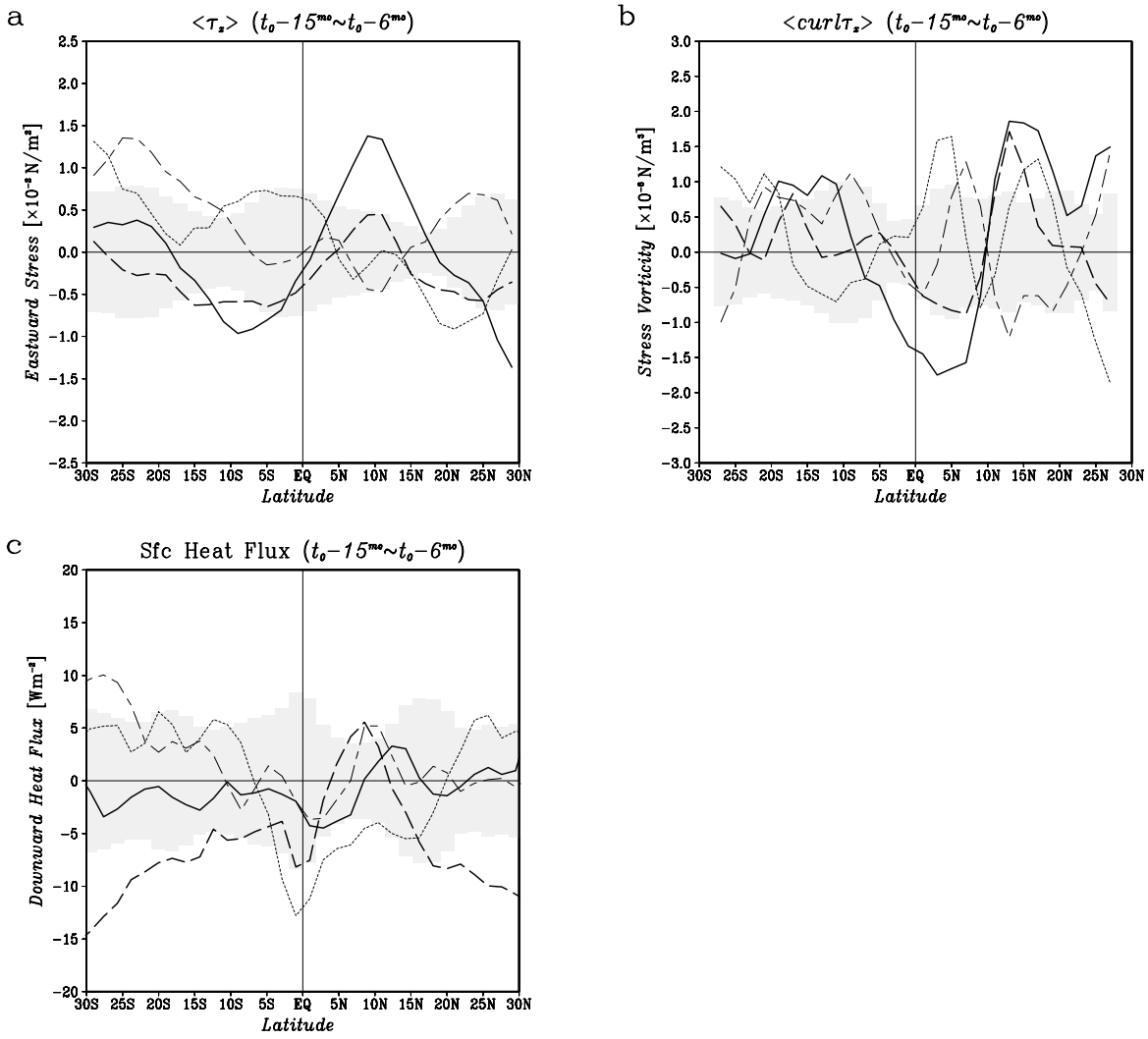

Figure 5-14 Meridional distributions of anomalies zonally averaged over the Pacific region (120°E-80°W) for the observed ’82/83 (solid), ’97/98 (dashed) strong El Niño and ’87 (dotted), ’92 (dash-dotted) weak El Niño. (a) Equatorial (6°S-6°N) zonal wind stress (from FSU), (b) wind stress *curl* at 6°N and (c) surface heat flux (NCEP/NCAR reanalysis) averaged over 6°S-6°N, for the recharge phase (average from 15 to 6 months before the SST-NINO3 peaks). Ranges of each standard deviation are shaded.

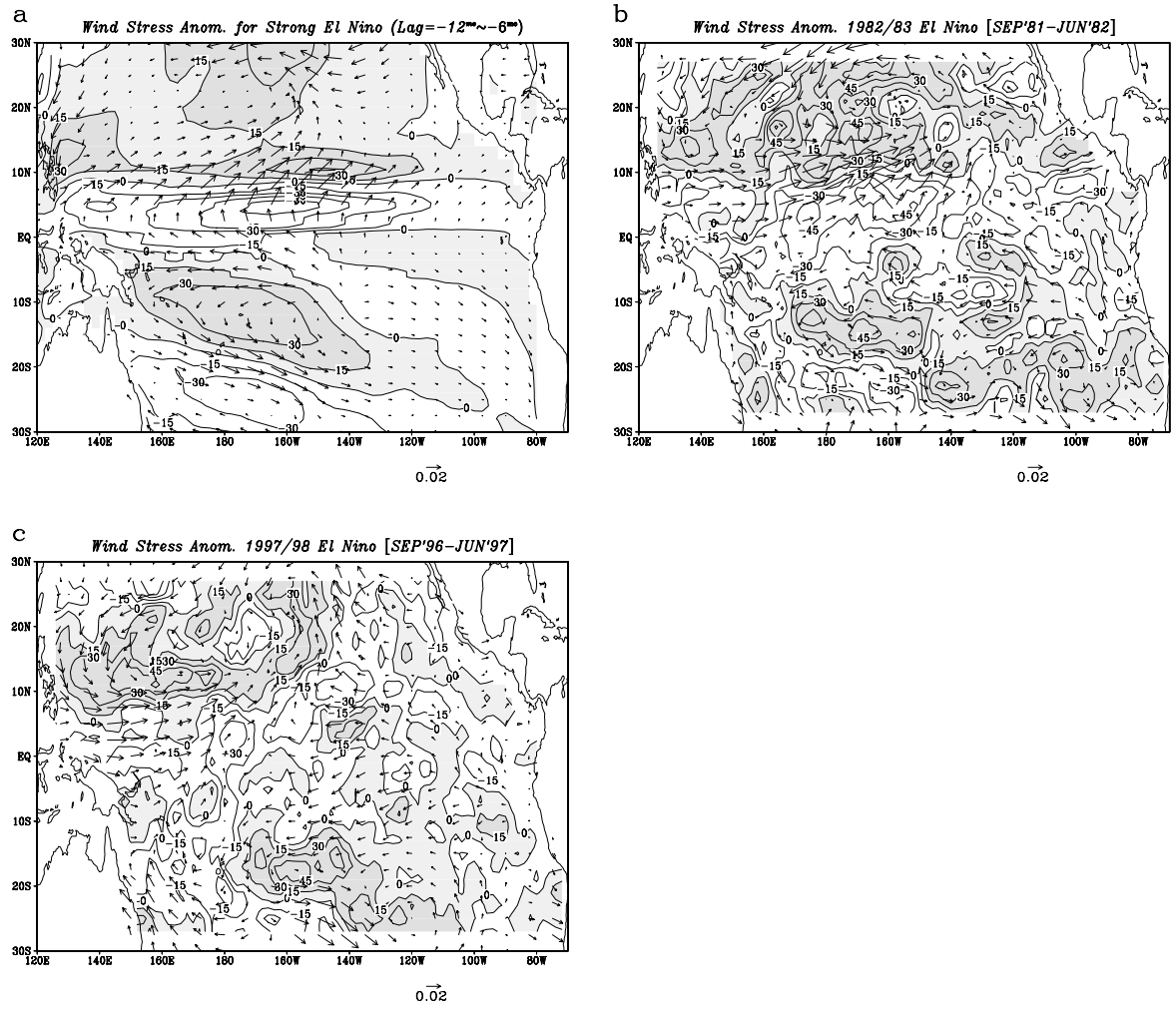

Figure 5-15 Geographical distributions of the wind stress (arrows) and its *curl* component (contours, negative shaded) anomalies in the recharge phase (average for 15 to 6 months before the SST-NINO3 peaks) for the (a) simulated *strong* warm event composite and the observed (b) 1982/83 and (c) 1997/98 El Niño. Units are Nm^{-2} for wind stress and 10^{-9} Nm^{-3} for wind stress *curl*.

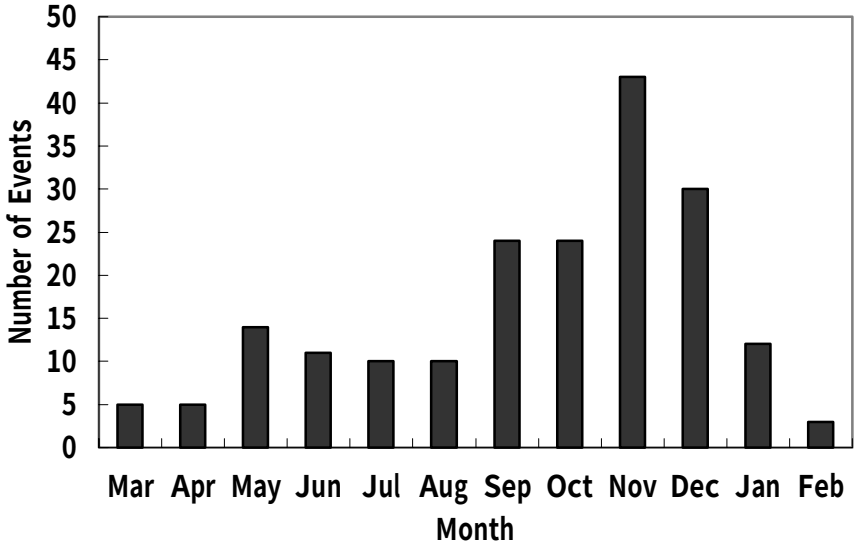

Figure 5-16 Histogram of the distribution of calendar month of the peak phase of SST-NINO3 anomaly for the simulated warm events.

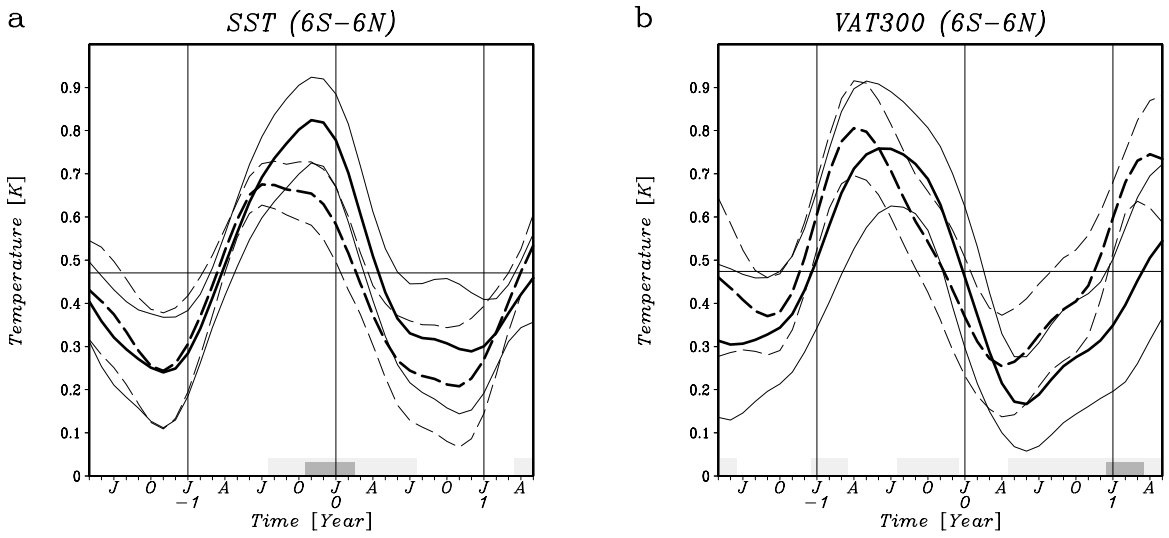

Figure 5-17 Same as Fig. 5-9, except for the normal-peak events (solid lines) and early-peak events (dashed lines) for the (a) SST and (b) VAT300 in the equator (6°S-6°N). The composites are made by aligning with the calendar months.

6 Conclusions

Two versions of the global coupled ocean-atmosphere general circulation models (CGCMs) are developed at Meteorological Research Institute. The first version (MRI-CGCM1) simulates natural climate variability in the Pacific Ocean, which reveals features in various aspects similar to the observation. Spatial and temporal structures of interdecadal variability in the Pacific Ocean are investigated using a set of two experiments with the MRI-CGCM1. The standard experiment with dynamical ocean component shows basin-wide spatial pattern of the principal SST variability similar to the observed one. Both interdecadal and interannual temporal structures of the SST variability agree well between the observation and the model. On the other hand, a slab ocean component coupled to the same atmospheric model fails simulating the observed temporal structure. It is suggested, therefore, that the timescale of the coupled variability is associated with dynamical processes in the ocean.

The model shows interannual variability in the tropical Pacific which has several typical characteristics shared with the observed ENSO. Basin scale feature of the principal SST variation for the ENSO timescale shows negative correlation in the central North Pacific with the tropical SST, and it is similar to that of the observed one. Associated variation of the model atmosphere indicates an intensification of the Aleutian low and a PNA-like teleconnection pattern as a response to the tropical warm SST anomaly. The ENSO timescale variability in the midlatitude ocean consists of the westward propagation of the subsurface temperature signal and the temperature variation within the shallow mixed layer forced by the anomalous atmospheric heat fluxes.

A distinct interdecadal mode of the coupled atmosphere-upper ocean temperature variability is found in the standard experiment of the MRI-CGCM1, with spatio-temporal structure coherent to the SST variability. The mode accompanies an ENSO-like spatial pattern of SST and surface wind, and behaves like a delayed oscillator in ENSO. A wedge shaped anomaly pattern of the upper thermocline temperature is formed in the eastern Pacific, and its northern subtropical signal propagates westward with getting enhanced by a subtropical wind forcing at the central basin. Arrival of the subtropical signal at the western Pacific around 20°N switches anomaly of subsurface temperature in the equatorial region through anomalous oceanic heat transport along the western boundary. Travel time of the trans-Pacific signal in the subtropics appears to be responsible for the timescale of this mode. The MRI-CGCM1 successfully simulated the second mode of SST with a major variation in the midlatitude North Pacific as in the observed SST. In the upper ocean heat

content, we found another distinct mode, which is characterized by a midlatitude-subtropics dipole pattern rotating clockwise around the North Pacific subtropical gyre. However, the associated SST variation of this mode shows a poor correspondence in the dominant interdecadal modes for the observed SST.

The second version (MRI-CGCM2) is developed aiming at improving the defects in the MRI-CGCM1 and achieving higher accuracy and reliability. The MRI-CGCM2 produces irregular El Niños with peak sea surface temperature (SST) anomalies ranging from 1°C to 4°C in the equatorial central-eastern Pacific. In the equatorial Pacific, the temporal phase relationship of the upper ocean heat content (OHC) anomaly relative to SST, and wind stress anomalies can be explained by the "recharge oscillator" mechanism. A difference of the zonal mean OHC anomaly between the equator and the northern subtropics arises before the development of an equatorial SST anomaly. The model also reveals realistic irregularities of ENSO in amplitude, periodicity, and seasonal phase locking. It is implied that a larger ocean heat content anomaly is accumulated on the equator as a precursor of a stronger El Niño. The heat-budget analysis suggests that horizontal advection in the ocean interior is a major contributor to the build-up of the larger OHC anomaly during the recharge phase, which is associated with the zonal-mean wind-*curl* anomaly in the off-equatorial North Pacific. This also implies that the surface heating in the subtropics is a potential contributor through meridional heat transport.

Elucidating the mechanism of interdecadal variability in the Pacific Ocean will require a number of processes which should be proved or verified in future studies. For example, whether the interaction between the subtropical SST and the atmospheric circulation is local interaction or interaction through an atmospheric teleconnection, and to what extent does the midlatitude ocean affect the internal variability of the midlatitude atmospheric circulation? It requires many hierarchical model experiments by use of coupled and uncoupled models. Relationship between the irregularity of ENSO and the interdecadal variability is also a profound theme that should be pursued in the future works. It is considered that there are possible linkages, since ENSO is found to be affected by the variation in the subtropics through midlatitude, where the decadal and interdecadal variabilies with atmosphere-ocean interaction are dominant. Further studies with various approaches, such as conceptual or simplified modeling, GCM experiments, and analyses of the observation will be useful. The observed climate in the past is not only a manifestation of its internal variability, but have been affected by various external forcing such as radiative forcing due to anthropogenic greenhouse gases and aerosols, variation of solar input due to solar activity, and stratospheric aerosol injection due to explosive volcanic activity, and so on. Also in the future works, it is an important theme to study the response

of decadal to interdecadal variability to the external forcings and elucidate origin of the climate change in the past. For the purpose mentioned above, higher accuracy is required for coupled GCMs in simulating the present and past climate variability, which will lead to higher reliability for the prediction of future climate change with the model. We should make continuous improvements of the models.

Acknowledgements

The author is grateful to Dr. Yoshiteru Kitamura of Japan Meteorological Agency, Professor Masahiro Endoh of the University of Tokyo, and Dr. Akira Noda of the Meteorological Research Institute, for their continuing encouragement and guidance. He also would like to thank Dr. Akio Kitoh of the Meteorological Research Institute for his valuable advice and guidance for this dissertation. The insightful comments and suggestions of Professors Fujio Kimura, Hiroshi L. Tanaka and Hiroaki Ueda of the University of Tsukuba and were helpful for clarifying and improving this dissertation. The author also thanks to Drs. Tatsushi Tokioka and Tatsuo Motoi of the Frontier Research System for Global Change for their advices and discussions during the early part of this study. The development of the model used for this study was done under the contributions from Drs. Masato Sugi, Masahiro Hosaka, Kiyotaka Shibata and other staffs of the Climate Research Department and the Oceanographic Research Department of the Meteorological Research Institute. He also thanks to Mr. Shuhei Maeda and colleagues of the Climate Research Department of Meteorological Research Institute for their valuable discussions and comments.

This work was done under the Study on the Prediction of Global Warming and the Study of the Prediction of Regional Climate Changes over Japan due to Global Warming of the Special Program of Japan Meteorological Agency. A part of the computational resources was supported by the Center for Global Environmental Research, National Institute for Environmental Studies.

Appendix

Improved Performance in Reproducing Climate with the MRI-CGCM2

1 Meridional Energy Transport

To evaluate the model's fundamental performance as a climate model, we examined the distribution of the oceanic and atmospheric meridional energy transports. This defines the first order climate system and reflects both dynamic and thermodynamic properties of the oceanic and atmospheric models. Figure A-1 shows the annual mean oceanic and atmospheric northward energy transports implied in a similar manner to Gleckler *et al.* (1995). The oceanic energy transports are implied by meridionally integrating the net energy fluxes (including flux adjustment) at the sea surface. The atmospheric transports are also evaluated from the difference of fluxes between the top of the atmosphere and the surface.

In the MRI-CGCM2, the atmosphere transports approximately 4.3 *PW* (peta watts) northward at 40°N and 5.0 *PW* southward at 40°S, and the ocean transports 1.6 *PW* northward and 1.5 PW southward at lower latitude (around 15°N and 15°S). These distributions of the meridional energy transports are consistent with the estimation based on the observational data (e.g., Trenberth, 1998). In contrast, the MRI-CGCM1 shows unrealistic oceanic transport, where southward transport prevails at all latitudes. This is attributed to the absence of thermohaline circulation in the Atlantic Ocean that would transport a large amount of heat northward.

2 Surface Heat Flux

Horizontal distribution of the simulated surface heat flux for the model and the observation (Da Silva et al., 1994) are shown in Fig. A-2. There are outstanding regions with large negative values (~ –250 Wm^{-2}) along the atmospheric storm tracks in the Pacific and Atlantic in winter. In these regions, the cold atmosphere (cooled over the continents) is getting heat from the warm oceans, transported poleward mainly by the western boundary currents (i.e. the Kuroshio Current and the Gulf Stream), and the further transport of heat poleward by the atmosphere with active storm tracks. These features agree well both qualitatively and quantitatively between model and observation. Relatively large positive regions are seen in summer near the eastern boundary and the subpolar gyre of the Pacific and the Atlantic oceans. In these regions, solar radiation at the sea surface is overestimated in the model due to insufficient representation of low-level clouds such as marine stratus or

stratocumulus, which are common in summer over the cold sea surface.

3 Precipitation

Precipitation is one of the most important elements of the coupled system. It affects the density distribution at the sea surface and associated tropical convective activities force crucial dynamic effects on the tropical ocean circulation through surface wind fields. Figure A-3 shows climatological precipitation for DJF and JJA, for the model and the observation (Xie and Arkin, 1996).

The seasonal variation of precipitation distribution is adequately reproduced. Seasonal variations associated with monsoon rainfall in Asia, Central and South America and Africa are reasonable. The seasonal location and activity of the Inter Tropical Convergence Zone (ITCZ) and the South Pacific Convergence Zone (SPCZ) over the oceans are well simulated. For example, the ITCZ around 10°N in the eastern Pacific is active in JJA and the SPCZ is active in DJF.

In the Asian summer monsoon (JJA), precipitation over the South China Sea and the western Pacific east of the Philippines is less than from observation. In DJF, there is a strong precipitation at 10°N in the western Pacific that is not observed. Globally averaged annual mean precipitation is 2.42 $mm\ day^{-1}$, which is 8% less than the observed value.

4 Sverdrup Flow

Sea surface wind stress is a crucial factor for simulating realistic upper ocean circulation in coupled models. Evaluating Sverdrup flow estimated from surface wind stress is a useful measure for validation of upper ocean circulation. Figure A-4 shows the Sverdrup flow streamfunctions calculated with both the wind stress data for the model and the observation (Hellerman and Rosenstein, 1983).

As a whole, circulation pattern and transport strength for every gyre circulation in each basin are well reproduced, suggesting good performance of the AGCM in reproducing surface wind. It is notable that the simulated Sverdrup transport in the tropics is very close to the observational one because of the use of wind stress adjustment.

The estimated transport associated with the North Pacific subpolar gyre in winter (JFM), at 90 *Sv*, is stronger than the 50 *Sv* observed value. This is associated with the stronger bias of the Aleutian Low. The transport associated with the North Pacific subtropical gyre in winter is close to the observation (80 *Sv*), but its northern branch (eastward flow), which corresponds to the Kuroshio Extension, is displaced northward (see 10 *Sv* contour, 40°N for the model and 35°N for the observation). In summer, the observed 30 *Sv* transport south of Japan is not seen in the model. This is probably related to the northward shift of the Pacific subtropical anticyclone in summer.

5 Meridional Overturning

One of the most serious defects of the former model (MRI-CGCM1) was the absence of the meridional deep overturning in the Atlantic Ocean as shown in Fig. A-5a. After the model integration started, the transport by the deep overturning immediately vanished, and after that, it remained as a small negative value for the entire model integration (Fig. A-5c).

The MRI-CGCM2 reasonably simulates the meridional overturning (Fig. A-5b) of the mixed structure of both shallow and deep cells. The deep overturning cell sinking near 60°N is associated with the NADW. Its mean transport is approximately 17 *Sv*, roughly agreeing with the estimate of 13 Sv by Schmitz and McCartney (1993). Its temporal variation (Fig. A-5d) seems to be a small, decreasing trend of 0.7 Sv per 100 years during the 200-year simulation, except for the first five decades. However, in the extended integration of the control run up to 300 years (not shown), it turns to an increasing trend after 200 years and seems to be a very long-term oscillation. There are interannual to interdecadal fluctuations with amplitudes of 1 to 2 Sv. The deep overturning cell near Antarctica, which is known as the origin of the Antarctic Bottom Water (AABW), is reproduced with 8 *Sv* maximum transport.

6 Sea Ice

Change in sea ice distribution has a large influence on the regional distribution of temperature change in the high latitudes. A small change of sea ice coverage (or compactness) can significantly affect the surface heat fluxes through the ice-albedo feedback. Thickness of sea ice is also an important factor because it influences heat flux at the sea ice surface. Therefore, simulating realistic sea ice is one of the most important factors for the model for studying climate change.

Figure A-6 shows sea ice distribution (compactness and thickness) simulated in the MRI-CGCM2 for March and September, together with the corresponding observation (compactness; NOAA-SIGRID, thickness (only in the NH); Bourk and Garrett, 1987). In the MRI-CGCM1 simulation, the extent of sea ice in the Northern Hemisphere was larger than observed. The Norwegian Sea and Barents Sea were covered with sea ice through all seasons. In reality, no sea ice in the Norwegian Sea (and only a little sea ice in winter in the Barents Sea) is observed, since warm, saline water is injected into these regions by the Norwegian Current, extending from the North Atlantic Current. In the MRI-CGCM2 simulation, the sea ice distribution is improved. In the NH, the extent of simulated sea ice agrees well with that observed in both seasons. The improvements to sea ice distribution in the Norwegian Sea, the Barents Sea and the Labrador Sea are mainly attributed to the improvement to the thermohaline circulation in the North Atlantic. The sea ice thickness is

2 to 4 m in the central Arctic Sea and is thicker in the Western Hemisphere. The thickness is less than 1m in the seasonal sea ice region. These features of the thickness distribution also agree with observation. In particular, the extent of thin (~50 *cm*) seasonal sea ice in the Okhotsk Sea is realistically simulated. In the SH, the winter (September) simulated sea ice corresponds in extent with the observation. However, the summer (March) sea ice extent is too small. A uniform winter sea ice thickness of less than 1 meter is reasonable.

During the 400-year integration, the model simulates stable sea ice without trends for both the NH and SH. The model sea ice displays interannual and interdecadal variability. For the NH sea ice volume, in particular, a large variability on a very long time scale (with a period of 60 years or longer) is notable.

7 Summary and Discussion

In the MRI-CGCM2, climatic drift is substantially absent in the model at least for several hundreds year period with respect to atmosphere, sea ice, SST and the upper ocean. The MRI-CGCM1 showed a relatively large trend in tropical SST and sea ice volume. Such progress was important in the development of the new version for experiments studying long-term climate changes. A long coupled spin-up of the model is essential to stabilize the coupled integration. In addition to an asynchronous coupled spin-up, we used a further, synchronous, coupled spin-up of more than 100 years. The coupled spin-up in the former simulation (Tokioka et al., 1996) was only 30 years long, following separate spin-ups of the OGCM and the AGCM, restoring the observed climatology of SST and sea surface salinity. Careful treatment in the spin-up prior to the model control simulation is very important.

It has been suggested that the meridional overturning in the Atlantic Ocean contributes to the reduced rate of warming in the northern Atlantic associated with global warming (IPCC, 1996). It has been argued in many studies that the variation of the Atlantic overturning is a critical factor in the climate variability of the North Atlantic. Although the MRI-CGCM1 failed in simulating the meridional overturning in the Atlantic Ocean, the MRI-CGCM2 shows a realistic value of 17 *Sv* near 54°N at 1500 *m* depth. The improvement is principally due to the introduction of isopycnal mixing parameterization with smaller lateral diffusivity, from which a strong density gradient around the fronts in the North Atlantic Ocean can be simulated in the model. The strong fronts lead to the strong North Atlantic Current that carries warm saline water to the Nordic Seas, producing a realistic sea ice distribution. This results in deep convections in the sea-ice-free region by strong atmospheric cooling, and consequently feeds a density flux to the North Atlantic Deep Water.

The sea ice distribution is much improved. The improvement of sea ice distribution

in the NH is mainly due to appropriately simulated thermohaline circulation in the North Atlantic and careful tuning of the flux adjustment in the sea ice region.

a

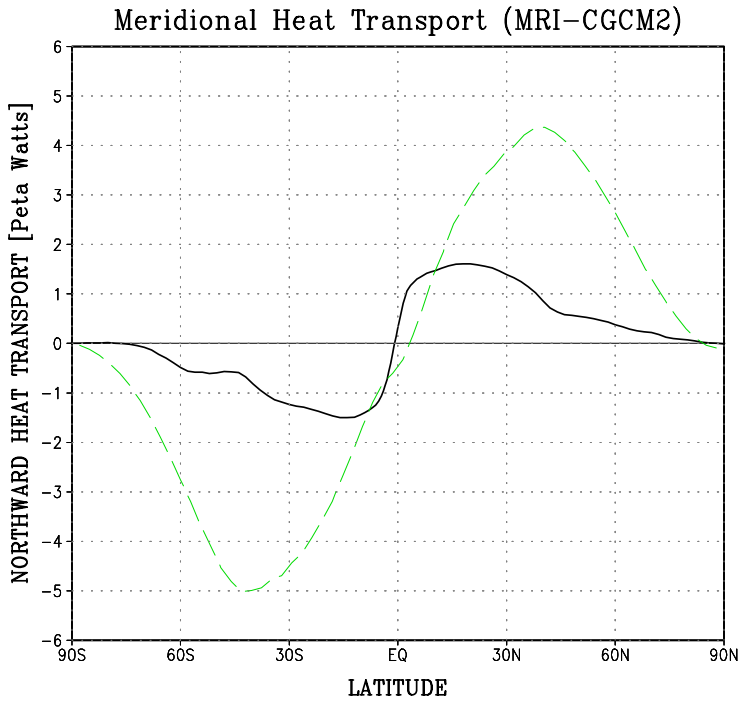

b

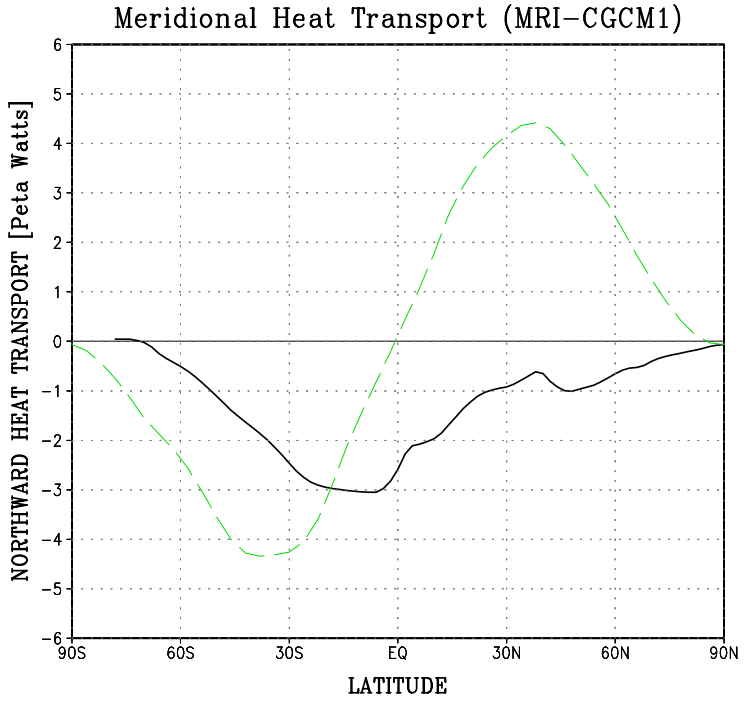

Figure A-1 Annual mean northward energy transports by the ocean (solid) and the atmosphere (dashed) in (a) MRI-CGCM2 and (b) MRI-CGCM1. The atmospheric transports are implied from differences between the net fluxes at the top-of-the-atmosphere and the sea surface (including flux adjustment). Unit is PW.

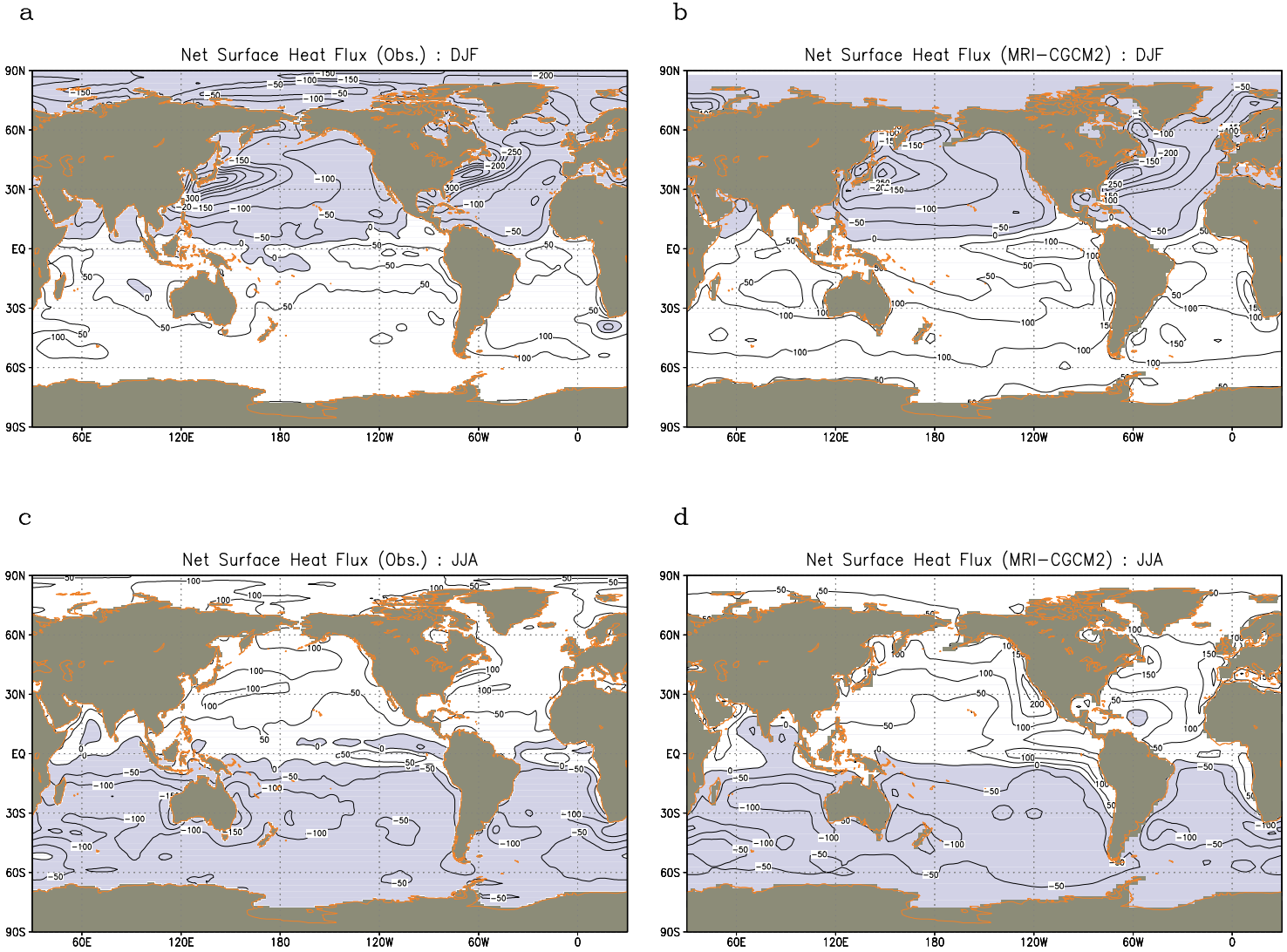

Figure A-2 Geographical distribution of the net surface heat flux for DJF mean (a, observation; b, MRI-CGCM2) and for JJA mean (c, observation; d, MRI-CGCM2). Unit is Wm^{-2}.

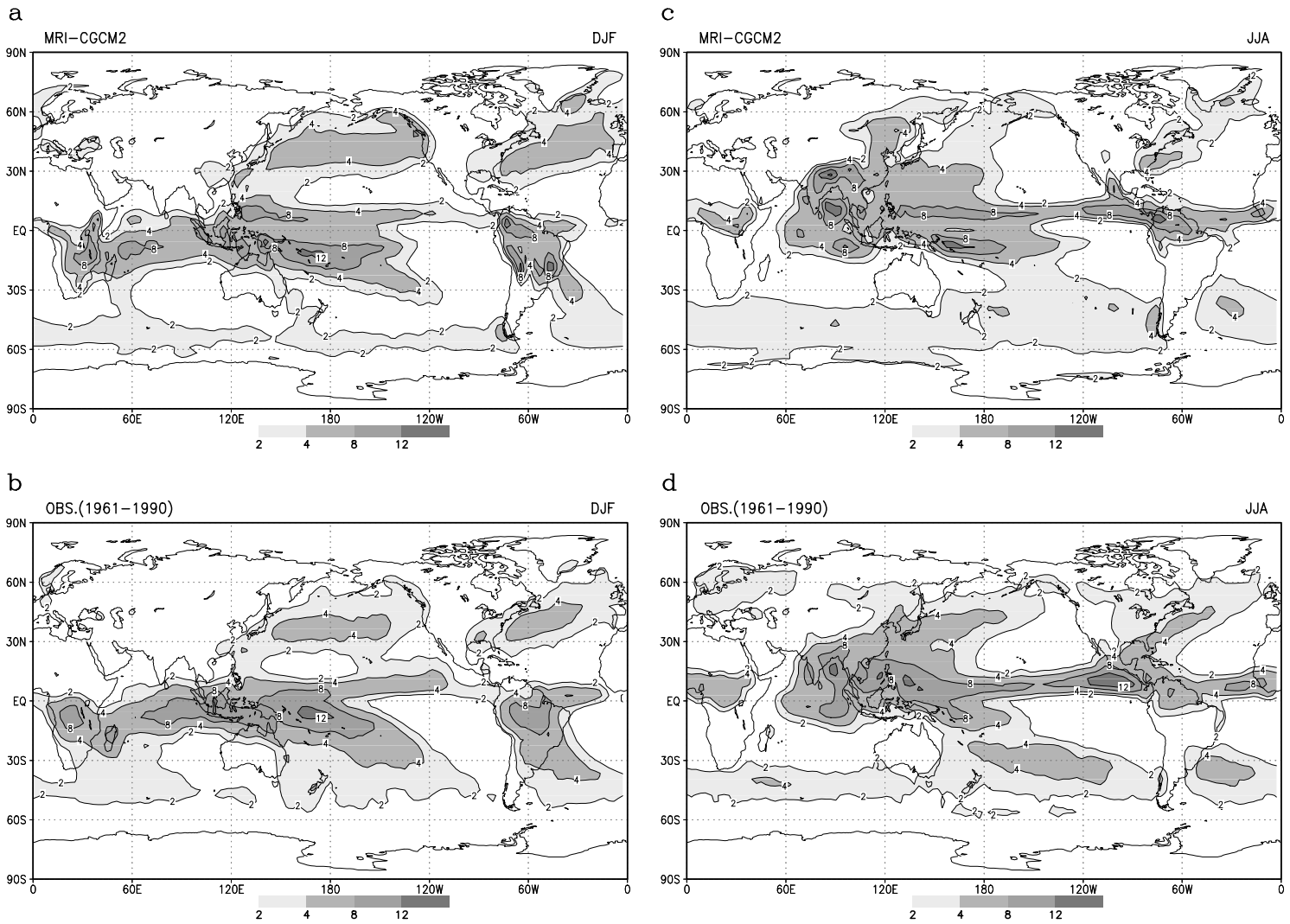

Figure A-3 Geographical distribution of the climatological precipitation for DJF (a, MRI-CGCM2; b, observation) and JJA (c, MRI-CGCM2; d: observation). Contour levels are 2, 4, 8, and 12 mm day^{-1}. The observations are from Xie and Arkin (1996).

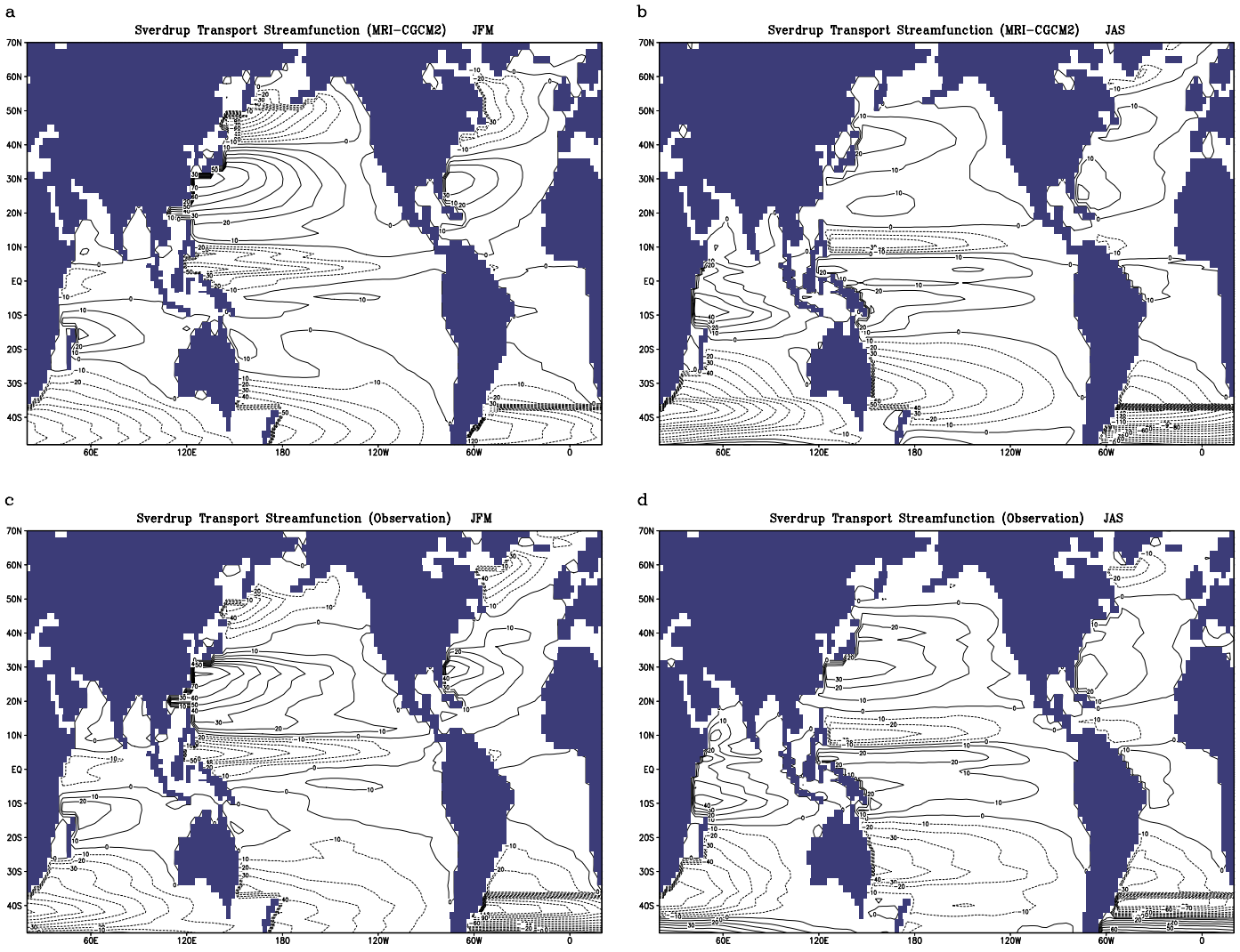

Figure A-4 Sverdrup flow stream functions based on the climatological surface wind stress of the MRI-CGCM2 for (a) JFM mean and (b) JAS mean, and the observation for (c) JFM mean and (d) JAS mean. The observational wind stress is from Hellermann and Rosenstein (1982). Unit is Sv ($10^6 m^3 s^{-1}$).

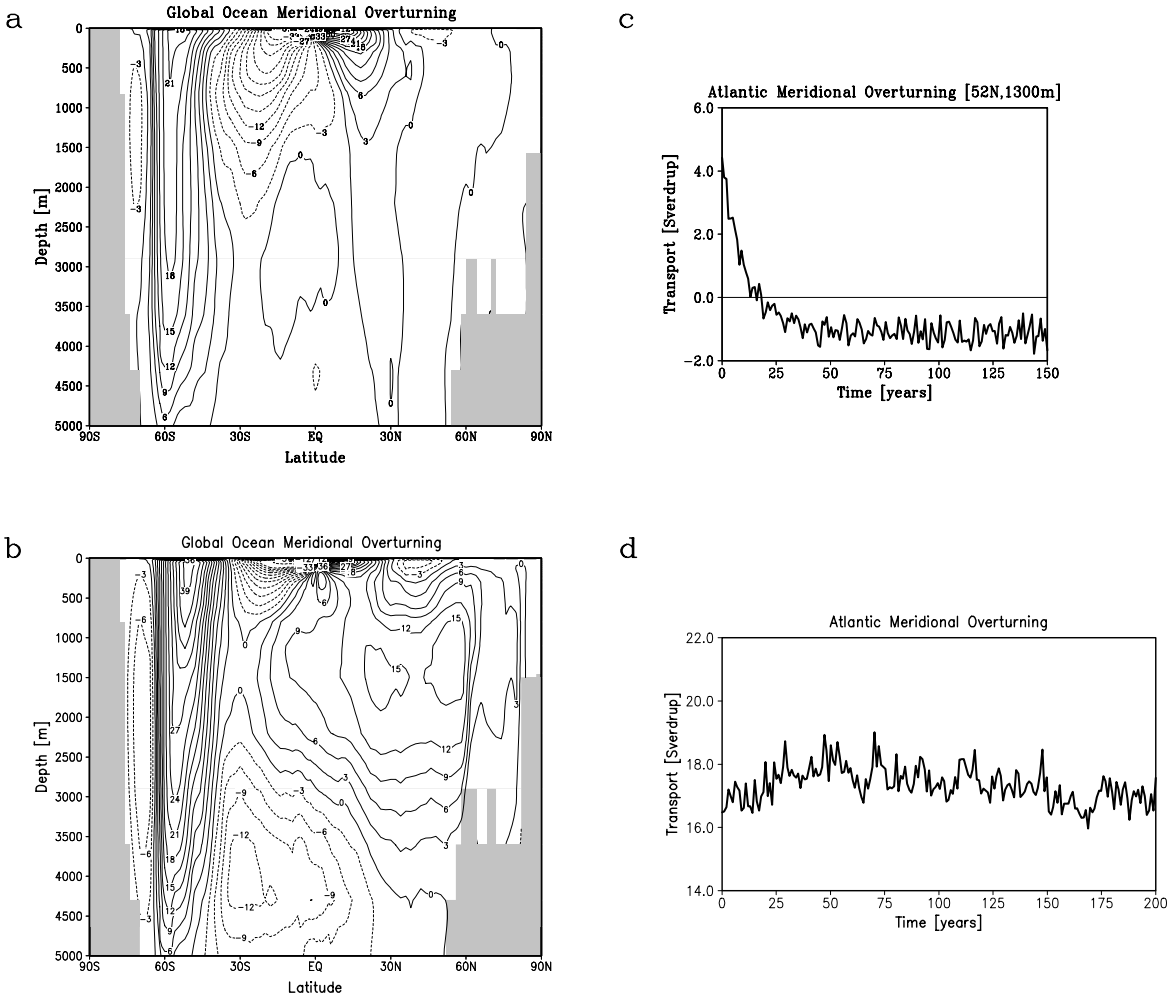

Figure A-5 Annual mean meridional overturning stream functions for the global ocean in (a) MRI-CGCM1 and (b) MRI-CGCM2. The time series of the maximum (annual mean) meridional overturning in the North Atlantic Ocean for (c) MRI-CGCM1 and (d) MRI-CGCM2. Values are in Sv.

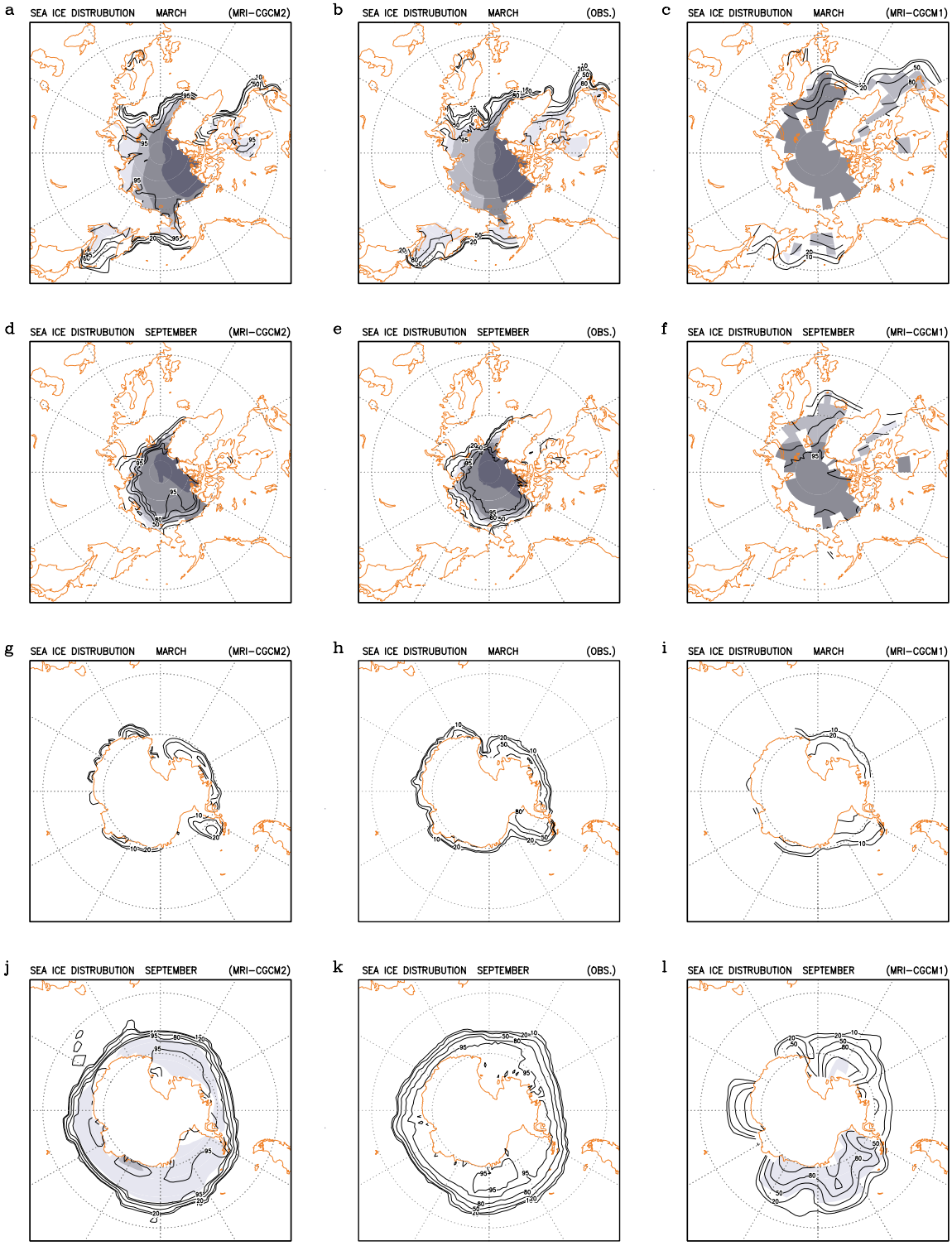

Figure A-6 Geographical distribution of the climatological sea ice compactness (contour, unit: percent) and mean thickness (shading) in the Northern Hemisphere (NH) for March (a, MRI-CGCM2; b, observation; c, MRI-CGCM1) and September (d, MRI-CGCM2; e, observation; f, MRI-CGCM1), and in the Southern Hemisphere (g-l, same as for NH). The observations are from NOAA-SIGRID for compactness, and Bourk and Garrett (1987) for thickness.

References

An, S.-I., and I.-S. Kang, 2000: A further investigation of the recharge oscillator paradigm for ENSO using a simple coupled model with the zonal and eddy separated. *J. Climate*, **13**, 1987-1993.

An, S.-I., and B. Wang, 2000: Interdecadal change of the structure of the ENSO mode and its impact on the ENSO frequency. *J. Climate*, **13**, 2044-2055.

Arakawa, A. and W. H. Schubert, 1974: Interaction of a cumulus cloud ensemble with the large scale environment, Part I. *J. Atmos. Sci.*, **31**, 674-701.

Battisti D. S., and A. C. Hirst, 1989: Interannual variability in the tropical atmosphere/ocean system: Influence of the basic state, ocean geometry and nonlinearity. *J. Atmos. Sci.*, **46**, 1687-1712.

Blanke B., J. D. Neelin, and D. Gutzler, 1997: Estimating the effect of stochastic wind stress forcing on ENSO irregularity. *J. Climate*, **10**, 1473-1487.

Bourk, R. H. and R. P. Garrett, 1987: *Cold Region Sci. Tech.*, **13**, 259-280.

Cane, M. A., and S. E. Zebiak, 1985: A theory for El Niño and the Southern Oscillation. *Science*, **228**, 1084-1087.

Chang, P., B. Wang, T. Li, and L. Ji, 1994: Interactions between the seasonal cycle and the southern oscillation – frequency entrainment and chaos in a coupled ocean-atmosphere model. *Geophys. Res. Lett.*, **21**, 2817-2820.

Chang, P., L. Ji, H. Li, and M. Flügel, 1996: Chaotic dynamics versus stochastic processes in El Niño -Southern Oscillation in coupled ocean-atmosphere models. *Physica D.*, **98**, 301-320.

Chung, C., and S. Nigam, 1999: Asian summer monsoon-ENSO feedback on the Cane-Zebiak model ENSO. *J. Climate*, **12**, 2787-2807.

Collins, M., 2000: The El Niño-Southern Oscillation in the second Hadley Centre coupled model and its response to greenhouse warming. *J. Climate*, **13**, 1299-1312.

Cubasch U, Hasselmann K, Höck H, Maier-Reimer E, Mikolajewicz U, Santer BD, Sausen R, 1992: Time-dependent greenhouse warming computations with a coupled ocean-atmosphere model. Climate Dyn 8: 55-69

Da Silva, A., C. Young, and S. Levitus, 1994: Atlas of Surface Marine Data 1994, Vol. 1: Algorithms and Procedures. NOAA Atlas NESDIS 6-9. U.S. Gov. Printing Office, Wash., D.C., 83 pp.

Deser, C., M. A. Alexander, and M. S. Timlin, 1996: Upper-ocean thermal variations in the North Pacific during 1970-1991, *J. Climate*, 9, 1840-1855.

Deser, C., and M. L. Blackmon, On the relationship between tropical and North Pacific sea surface temperature variations, *J. Climate*, 8, 1677-1680, 1995.

Fedorov, A. V., and S. G. Philander, 2000: Is El Niño changing? *Science*, **288**, 1997-2002.

Flügel, M., and P. Chang, 1999: Stochastically induced climate shift of El Niño-Southern Oscillation. *Geophys. Res. Lett.*, **26**, 2473-2476.

Galanti, E., and E. Tziperman, 2000: ENSO's phase locking to the seasonal cycle in the fast-SST, fast-wave, and mixed-mode regimes. *J. Atmos. Sci.*, **57**, 2936-2950.

Gent, P. R. and J. C. McWilliams, 1990: Isopycnal mixing in ocean circulation models. *J. Phys. Oceanogr.*, **20**, 150-155.

Gleckler, P. J., D. A. Randall, G. Boer, R. Colman, M. Dix, V. Galin, M. Helfand, J. Kiehl, A. Kitoh, W. Lau, X.-Y. Liang, V. Lykossov, B. McAvaney, K. Miyakoda, S. Planton, and W. Stern, 1995: Cloud-radiative effects on implied oceanic energy transports as simulated by atmospheric general circulation models. *Geophys. Res. Lett.*, **22**, 791-794.

Graham, N. E. , 1994: Decadal-scale climate variability in the tropical and North Pacific during the 1970s and 1980s: observations and model results, *Climate Dyn.*, 10, 135-162.

Graham NE, Barnett TP, Wilde R., 1994: On the roles of tropical and midlatitude SSTs in forcing interannual to interdecadal variability in the winter northern hemisphere

circulation. J Climate 7: 1416-1441
Gu, D., and S. G. H. Philander, Interdecadal climate fluctuations that depend on exchanges between the tropics and extratropics, *Science*, 275, 805-807, 1997.
Hannachi, A., D. B. Stephenson, and K. R. Sperber, 2003: Probability-based methods for quantifying nonlinearity in the ENSO. *Climate Dyn.*, **20**, 241-256.
Hellerman, S. and M. Rosenstein, 1983: Normal monthly wind stress over the world's ocean with error estimates. *J. Phys. Oceanogr.*, **13**, 1093-1104.
Horel, J. D., and J. M. Wallace, 1981: Planetary-scale atmospheric phenomena associated with the Southern Oscillation, *Mon. Weather Rev.*, 109, 813-829.
IPCC, 1990: Climate Change, The IPCC Scientific Assessment. eds. Houghton JT, Jenkins GJ, Ephraums JJ. Cambridge University Press, Cambridge New York Port Chester Melbourne Sydney, 365pp
IPCC, 1996: Climate change 1995, The science of climate change. Eds. J. T. Houghton, L. G. Meira Filho, B. A. Callander, N. Harris, A. Kattenberg and K. Maskell. Cambridge Univ. Press, 570pp.
Iwasaki, T., S. Yamada and K. Tada, 1989: A parameterization scheme of orographic gravity wave drag with the different vertical partitioning, part 1: Impact on medium range forecasts. *J. Meteor. Soc. Japan*, **67**, 11-41.
Jiang, N., J. D. Neelin, and M. Ghil, 1995: Quasi-quadrennial and quasi-biennial variability in COADS equatorial Pacific sea surface temperature and winds. *Climate Dyn.*, **12**, 101-112.
Jin, F.-F., 1997: An equatorial recharge paradigm for ENSO, Part I, Conceptual model. *J. Atmos. Sci.*, **54**, 811-829.
Jin, F.-F. , 1997: A theory of interdecadal climate variability of the North Pacific ocean-atmosphere system, *J. Climate*, 10, 1821-1835.
Jin, F.-F., 2001: Low-frequency modes of tropical ocean dynamics. *J. Climate*, **14**, 3874-3881.
Jin, F.-F., J. D. Neelin, and M. Ghil, 1994: El Niño on the devil's staircase, Annual subharmonic steps to chaos. *Science*, **264**, 70-72.
Jones, P. D., 1994: Hemispheric surface air temperature variations: A reanalysis and update to 1993. *J. Climate*, **7**, 1794-1802.
Kalnay, E., M. Kanamitsu, R. Kistler, W. Collins, D. Deaven, L. Gandin, M. Iredell, S. Saha, G. White, J. Woollen, Y. Zhu, A. Leetmaa, R. Reynolds, M. Chelliah, W. Ebisuzaki, W.Higgins, J. Janowiak, K. C. Mo, C. Ropelewski, J. Wang, Roy Jenne, and Dennis Joseph, 1996: The NCEP/NCAR 40-Year Reanalysis Project. *Bull. Amer. Meteor. Soc.* **77**, 437-471.
Kang, I.-S., and S.-I. An, 1998: Kelvin and Rossby wave contributions to the SST oscillation of ENSO. *J. Climate*, **11**, 2461-2469.
Kashiwabara T (1987) On the recent winter cooling in the North Pacific (in Japanese). Tenki 34: 777-781
Kawamura, R. , 1994: A rotated EOF analysis of global sea surface temperature variability with interannual and interdecadal time scales, *J. Phys. Oceanogr.*, 24, 707-715.
Kinter III, J. L., K. Miyakoda, and S. Yang, 2000: Recent change in the connection from the Asian monsoon to ENSO. *J. Climate*, **15**, 1203-1215.
Kirtman, B. P., and P. S. Schopf, 1998: Decadal variability in ENSO predictability and prediction. *J. Climate*, **11**, 2804-2822.
Kitoh, A., T. Motoi, and H. Koide, 1999: SST variability and its mechanism in a coupled atmosphere-mixed layer ocean model, *J. Climate*, 12, 1221-1239.
Kitoh, A., A. Noda, Y. Nikaidou, T. Ose, and T. Tokioka, 1995: AMIP simulations of the MRI GCM., *Pap. Meteor. Geophys.*, 45, 121-148.
Kitoh A, Noda A, Nikaidou Y, Ose T, Tokioka T, 1995: AMIP simulations of the MRI GCM. Pap Meteor Geophys 45: 121-148
Kitoh, A., S. Yukimoto, and A. Noda, 1999: ENSO-monsoon relationship in the MRI

coupled GCM. *J. Meteor. Soc. Japan*, **77**, 1221-1245.
Kitoh, A., S. Yukimoto, A. Noda, and T. Motoi, 1997: Simulated changes in the Asian summer monsoon at times of increased atmospheric CO_2. *J. Meteor. Soc. Japan*, **75**, 1019-1031.
Kleeman, R., and S. B. Power, 1994: Limits to predictability in a coupled ocean-atmosphere model due to atmospheric noise. *Tellus*, **46A**, 529-540.
Knutson, T. R., and S. Manabe, 1998: Model assessment of decadal variability and trends in the tropical Pacific Ocean, *J. Climate*, 11,2273-2296.
Krishnamurthy, V., and B. N. Goswami, 2000: Indian monsoon – ENSO relationship on interdecadal timescale. *J. Climate*, **13**, 579-595.
Lacis, A. A. and J. E. Hansen, 1974: A parameterization for the absorption of solar radiation in the Earth's atmosphere. *J. Atmos. Sci.*, **31**, 118-133.
Latif, M., and T. P. Barnett, 1994: Causes of decadal climate variability over the North Pacific and North America, *Science*, 266, 634-637.
Latif, M., and T. P. Barnett, 1996: Decadal climate variability over the North Pacific and North America: Dynamics and predictability, *J. Climate*, 9, 2407-2423.
Latif M, Sterl A, Maier-Reimer E, Junge MM, 1993: Climate variability in a coupled GCM. Part I: The tropical Pacific. J Climate 6: 5-21
Lau N-C, Philander SGH and Nath MJ, 1992: Simulation of ENSO-like phenomena with a low-resolution coupled GCM of the global ocean and atmosphere. J Climate 5: 284-307
Lau, N.-C., and M. J. Nath, 1994: A modeling study of the relative roles of tropical and extratropical SST anomalies in the variability of the global atmosphere-ocean system, *J. Climate*, 7, 1184-1207.
Legler, D. M., I. M. Navon, and J. J. O'Brien, 1989: Objective analysis of pseudostress over the Indian Ocean using a direct-minimization approach. *Mon. Wea. Rev.*, **117**,709-720.
Levitus S, 1982: Climatological Atlas of the World Oceans, NOAA Prof. Pap. 13, U.S. Government Printing Office, Washington, D.C.
Levitus, S. and T. P. Boyer, 1994: World Ocean Atlas, Volume 4: Temperature, NOAA Atlas NESDIS 4, 129 pp.
Levitus, S., R. Burgett, and T. P. Boyer, 1994: World Ocean Atlas, Volume 3: Salinity, NOAA Atlas NESDIS 3, 111 pp.
Li, T., 1997: Phase transition of the El Nino-Southern Oscillation: A stationary SST mode. *J. Atmos. Sci.*, **54**, 2872-2887.
Liu, Z. , 1999: Planetary wave modes in the thermocline: non-Doppler-shift mode, advective mode and Green mode, *Quart. J. Royal Meteor. Soc.*, 125, 1315.
Liu, Z. , 1999: Forced planetary wave response in a thermocline gyre, *J. Phys. Oceanogr.*, 29, 1036-1055.
Manabe S, Stouffer RJ, Spelman MJ, Bryan K, 1991: Transient responses of a coupled ocean-atmosphere model to gradual changes of atmospheric CO2. Part I : Annual mean response. J Climate 4: 785-818
Meehl GA, 1990: Seasonal cycle forcing of El Niño-Southern Oscillation in a global coupled ocean-atmosphere GCM. J Climate 3: 72-98
Meinen, C. S., and M. J. McPhaden, 2000: Observations of warm water volume changes in the equatorial Pacific and their relationship to El Niño and La Niña. *J. Climate*, **15**, 3551-3559.
Mellor, G. L. and P. A. Durbin, 1975: The structure and dynamics of the ocean surface mixed layer. *J. Phys. Oceanogr.*, **5**, 718-728.
Mellor, G. L. and L. Kantha, 1989: An ice-ocean coupled model. *J. Geophys. Res.*, **94**, 10937-10954.
Mellor, G. L. and T. Yamada, 1974: A hierarchy of turbulence closure models for planetary boundary layers. *J. Atmos. Sci.*, **31**, 1791-1806.
Mellor, G. L. and T. Yamada, 1982: Development of a turbulence closure model for

geophysical fluid problems. *Rev. Geophys. Space Phys.*, **20**, 851-875.
Miller AJ, 1992: Large-scale ocean-atmosphere interactions in a simplified coupled model of the midlatitude wintertime circulation. J Atmos Sci 49: 273-286
Miller, A. J., D. R. Cayan, T. P. Barnett, N. E. Graham, J. M. Oberhuber, 1994: Interdecadal variability of the Pacific Ocean: model response to observed heat flux and wind stress anomalies, *Climate Dyn.*, 9, 287-302.
Miller AJ, Daniel RC, Barnett TP, Graham NE, Oberhuber JM, 1994: Interdecadal variability of the Pacific Ocean: model response to observed heat flux and wind stress anomalies. Clim Dyn 9: 287-302
Mitchell, T. P., and J. M. Wallace, 1996: ENSO seasonality: 1950-78 versus 1979-92. *J. Climate*, **9**, 3149-3161.
Munnich, M., M. A. Cane, and S. E. Zebiak, 1991: A study of self-excited oscillations of the tropical ocean-atmosphere system. *J. Atmos. Sci.*, **48**, 1238-1248.
Nagai T, Tokioka T, Endoh M, Kitamura Y, 1992: El Niño-Southern Oscillation simulated in an MRI atmosphere-ocean coupled general circulation model. J Climate 5: 1202-1233
Neelin JD, 1991: The slow sea surface temperature mode and the fast-wave limit: Analytic theory for tropical interannual oscillations and experiments in a hybrid coupled model. J Atmos Sci 484: 584-606
Neelin, J. D., D. S. Battisti, A. C. Hirst, F.-F. Jin, Y. Wakata, T. Yamagata, and S. E. Zebiak, 1998: ENSO theory. *J. Geophys. Res.*, **103**, 14,261-14,290.
Neelin, F.-F. Jin, and H.-H. Syu, 2000: Variations in ENSO phase locking. *J. Climate*, **13**, 2570-2590.
Nitta, T., and S. Yamada, 1989: Recent warming of tropical sea surface temperature and its relationship to the northern hemisphere circulation, *J. Meteor. Soc. Japan*, 67, 375-383.
Noda, A., K. Yoshimatsu, A. Kitoh and H. Koide, 1999a: Relationship between natural variability and CO_2-induced warming pattern: MRI coupled atmosphere/mixed-layer ocean (slab) GCM experiment. 10th Symposium on Global Change Studies, 10-15 January 1999, Dallas, Texas., pp.355-358, American Meteorological Society, Boston. Mass.
Noda, A., K. Yoshimatsu, S. Yukimoto, K. Yamaguchi, and S. Yamaki, 1999b: Relationship between natural variability and CO_2-induced warming pattern: MRI AOGCM atmosphere/mixed-layer ocean (slab) GCM experiment. 10th Symposium on Global Change Studies, 10-15 January 1999, Dallas, Texas, pp.359-362, American Meteorological Society, Boston. Mass.
Oort A. H., and J. J. Yienger, 1996: Observed interannual variability in the Hadley circulation and its connection to ENSO. *J. Climate*, **9**, 2751-2767.
Palmer, T. N., G. N. Shutts and R. Swinbank, 1986: Alleviation of a systematic westerly bias in general circulation and numerical weather prediction models through an orographic gravity wave drag parameterization. *Quart. J. Roy. Meteor. Soc.*, **112**, 1001-1039.
Parker, D. E., P. D. Jones, C. K. Folland, and A. Bevan, Interdecadal changes of surface temperature since the late nineteenth century, *J. Geophys. Res.*, 99, 14373-14399. 1994.
Penland, C., and P. D. Sardeshmukh, 1995: The optimal growth of tropical sea surface temperature anomalies. *J. Climate*, **8**, 1999-2024.
Penland, C., M. Flügel, and P. Chang, 2000: Identification of dynamical regimes in an intermediate coupled ocean-atmosphere model. *J Climate*, **13**, 2105-2115.
Perovich, D. K., G. A. Maykut and T. C. Grenfell, 1986: Optical properties of ice and snow in the polar oceans, I. Observations. *Proc. SPIE Int. Soc. Opt. Eng.*, **637**, 232-241.
Philander SGH, Pacanowski RC, Lau NC, Nath MJ, 1992: Simulation of ENSO with a global atmospheric GCM coupled to a high-resolution, tropical Pacific Ocean GCM. J Climate 5: 308-329

Philander SGH, Yamagata T, Pacanowski RC, 1984: Unstable air-sea interactions in the tropics. J Atmos Sci 41: 604-613

Randall D, 1976: The interaction of the planetary boundary layer with large-scale circulations. Ph. D. dissertation, The University of California, Los Angels, 247pp

Randall, D. and D.-M. Pan, 1993: Implementation of the Arakawa-Schubert cumulus parameterization with a prognostic closure. Meteorological Monograph/The representation of cumulus convection in numerical models, 46, 145-150.

Rasmusson, E. M., and T. H. Carpenter, 1982: Variations in tropical sea surface temperature and surface wind fields associated with the Southern Oscillation/El Niño. *Mon. Wea. Rev.*, **110**, 354-384.

Rayner, N. A., Horton, E. B., Parker, D. E., Folland, C. K. and Hackett, R. B. 1996: Version 2.2 of the Global Sea-Ice and Sea Surface Temperature data set, 1903-1994. Climate Research Technical Note 74.

Read, J. F. and R. T. Pollard, 1993: Structure and transport of the Antarctic circumpolar current and Agulhas return current at 40°E. *J. Geophys. Res.*, **98**, 12281-12295.

Robinson, D. A., K. F. Dewey and R. R. Heim, Jr., 1993: Global snow cover monitoring: An update. *Bull. Amer. Meteor. Soc.*, **74**, 1689-1696.

Saravanan, R. and J. C. McWilliams, Stochasticity and spatial resonance in interdecadal climate fluctuations, *J. Climate*, 10, 2299-2320, 1997.

Sato, N., P. J. Sellers, D. A. Randall, E. K. Schneider, J. Shukla, J. L. Kinter, Y.-Y. Hou and E. Albertazzi, 1989: Effects of implementing the simple biosphere model in a general circulation model. *J. Atmos. Sci.*, **46**, 2757-2782.

Schmitz, W. J. Jr. and M. S. McCartney, 1993: On the north Atlantic circulation. *Rev. Geophys.*, **31**, 29-49.

Schopf, P. S., and M. J. Suarez, 1988: Vacillations in a coupled atmosphere-ocean model. *J. Atmos. Sci.*, **45**, 549-566.

Schneider, N., A. J. Miller, M. A. Alexander, and C. Deser, 1999: Subduction of decadal North Pacific temperature anomalies: Observations and dynamics, J. *Phys. Oceanogr.*, 29, 1056-1070.

Sellers, P. J., Y. Mintz, Y. C. Sud and A. Dalcher, 1986: A simple biosphere model (SiB) for use within general circulation models. *J. Atmos. Sci.*, **43**, 505-531.

Shibata, K. and T. Aoki, 1989: An infrared radiative scheme for the numerical models of weather and climate. *J. Geophys. Res.*, **94**, 14923-14943.

Shibata, K. and A. Uchiyama, 1992: Accuracy of the delta-four-stream approximation in inhomogeneous scattering atmospheres. *J. Meteor. Soc. Japan*, **70**, 1097-1109.

Shibata, K., H. Yoshimura, M. Ohizumi, M. Hosaka and M. Sugi, 1999: A simulation of troposphere, stratosphere and mesosphere with an MRI/JMA98 GCM. *Pap. Meteor. Geophys.*, **50**, 15-53.

Shukla, J., and D. A. Paolino, 1983: The Southern Oscillation and long-range forecasting of the summer monsoon rainfall over India. *Mon. Wea. Rev.*, **111**, 1830-1837.

Stockdale T, Anderson D, Davey M, Delecluse P, Kattenberg A, Kitamura Y, Latif M, Yamagata T, 1993: Intercomparison of tropical ocean GCMs. TOGA Numerical Experimentation Group, WMO/TD-No.545.

Suarez, M. J., and P. S. Schopf, 1988: A delayed oscillator for ENSO, *J. Atmos. Sci.*, 45, 3283-3287.

Thompson, D. W. J. and J. M. Wallace, 1998: The Arctic oscillation signature in the wintertime geopotential height and temperature fields. *Geophys. Res. Lett.*, **25**, 1297-1300.

Tokioka T, Yamazaki K, Yagai I, Kitoh A, 1984: A description of the Meteorological Research Institute atmospheric general circulation model (MRI·GCM-I). Tech Report No. 13 MRI, 249pp.

Tokioka T, Kitoh A, Nakagawa S, 1993: Interactions between lower atmosphere and the ocean realized in a coupled atmosphere-ocean general circulation model.

Extended Abstracts of International WCRP Symposium - Clouds and Ocean in Climate -. 28 September - 2 October 1992, Nagoya, 1.5-1.8

Tokioka, T., A. Noda, A. Kitoh, Y. Nikaidou, S. Nakagawa, T. Motoi, S. Yukimoto, and K. Takata, 1995: A Transient CO_2 Experiment with the MRI CGCM -- Quick Report ---, *J. Meteor. Soc. Japan.*, 73, 817-826.

Tokioka T., A. Noda, A. Kitoh, Y. Nikaidou, S. Nakagawa, T. Motoi, S. Yukimoto and K. Takata, 1996: A transient CO2 experiment with the MRI CGCM – Annual mean response. CGER's supercomputer monograph report, 2, Center for Global Environmental Research, National Institute for Environmental Studies, Environmental Agency of Japan.

Tokioka, T., K. Yamazaki, A. Kitoh and T. Ose, 1988: The equatorial 30-60 day oscillation and the Arakawa-Schubert penetrative cumulus parameterization. *J. Meteor. Soc. Japan*, **66**, 883-901.

Torrence, C., and P. J. Webster, 1999: Interdecadal changes in the ENSO – monsoon system. *J. Climate*, **12**, 2679-2690.

Trenberth, K. E. , 1990: Recent observed interdecadal climate changes in the Northern Hemisphere, *Bull. Amer. Meteor. Soc.*, 71, 988-993.

Trenberth, K. E., 1997: The definition of El Niño. *Bull. Amer. Met. Soc.*, **78**, 2771-2777.

Trenberth, K. E., 1998: The heat budget of the atmosphere and ocean. Proceedings of the First WCRP International Conference on Reanalysis, WMO/TD-No. 876, 17-20.

Trenberth, K. E. and J. W. Hurrell, 1994: Decadal atmosphere-ocean variations in the Pacific, *Climate Dyn.*, 9, 303-319.

Tziperman, E., L. Stone, M. A. Cane, and H. Jarosh, 1994: El Niño chaos: Overlapping of resonances between the seasonal cycle and the Pacific Ocean-atmosphere oscillator. *Science*, **264**, 72-74.

Tziperman, E., M. A. Cane, and S. E. Zebiak, 1995: Irregularity and locking to the seasonal cycle in an ENSO prediction model as explained by the quasi-periodicity route to chaos. *J. Atmos. Sci.*, **52**, 293-306

Tziperman, E., M. A. Cane, S. E. Zebiak, Y. Xue, and B. Blumenthal, 1998: Locking of El Niño's peak time to the end of the calendar year in the delayed oscillator picture of ENSO. *J. Climate*, **11**, 2191-2199.

Venrick, E. L., J. A. McGowan, D. A. Cayan, and T. L. Hayward, 1987: Climate and chlorophyll a: long-term trends in the central North Pacific Ocean, *Science*, 239, 70-72.

Wang, W.-C., X.-Z. Ling, M. P. Dudek, D. Pollard and S. L. Thompson, 1995: Atmospheric ozone as a climate gas. *Atmos. Res.*, **37**, 247-256.

Watanabe T, and K. Mizuno, 1995: Interdecadal variation of the subsurface temperature in the Pacific Ocean. Preprint of International Workshop on Numerical Prediction of Oceanic Variations, March 1995, JMA, Tokyo,223pp

Weisberg, R. H., and C. Wang, 1997: A western Pacific oscillator paradigm for the El Niño-Southern Oscillation. *Geophys. Res. Lett.*, **24**, 779-782.

Xie, S.-P., 1995: Interaction between the annual and interannual variations in the equatorial Pacific. *J. Phys. Oceanogr.*, **25**, 1930-1941.

Xie, P. and P. A. Arkin, 1996: Analyses of global monthly precipitation using gauge observations, satellite estimates and numerical model predictions. *J. Climate*, **9**, 4840-4858.

Yagai I, Yamazaki K, 1988: Effect of the internal gravity wave drag on the 12-layer MRI GCM January simulation. Report No. 12 of the Proceedings of the WGNE Workshop on Systematic Errors in Models of the Atmosphere, 19-23 September 1988, Working Group on Numerical Experimentation, Toronto, 8pp

Yamagata T, Masumoto Y, 1992: Interdecadal natural climate variability in the Western Pacific and its implication in global warming. J Meteor Soc Japan 70: 167-175

Yu, J.-Y., and C. R. Mechoso, 2001: A coupled atmosphere-ocean GCM study of the ENSO cycle. *J. Climate*, **15**, 2329-2350.

Yukimoto, S., M. Endoh, Y. Kitamura, A. Kitoh, T. Motoi, A. Noda, and T. Tokioka, Interannual and interdecadal variabilities in the Pacific in an MRI coupled GCM., *Climate Dyn.*, 12, 667-683, 1996.

Yukimoto, S. M. Endoh, Y. Kitamura, A. Kitoh, T. Motoi, and A. Noda, 2000: ENSO-like interdecadal variability in the Pacific Ocean as simulated in a coupled general circulation model. *J. Geophys. Res.*, **105**, 13,945-13,963.

Yukimoto, S., A., Noda, A. Kitoh, M. Sugi, Y. Kitamura, M. Hosaka, K. Shibata, S. Maeda, and T. Uchiyama, 2001: The New Meteorological Research Institute Coupled GCM (MRI-CGCM2) — Model climate and variability —. *Pap. in Meteor. and Geophys.*, **51**, 47-88.

Zebiak, S. E., 1989: Oceanic heat content variability and El Niño cycles. *J. Phys. Oceanogr.* **19**, 475-486.

Zebiak, S. E., and M. A. Cane, 1987: A model El Niño-Southern Oscillation. *Mon. Wea. Rev.*, **115**, 2262-2278.

Zhang, R.-H., and S. Levitus, Structure and cycle of decadal variability of upper-ocean temperature in the North Pacific, *J. Climate*, 10, 710-727, 1997.

Zhang, Y., J. M. Wallace, and D. S. Battisti, 1997: ENSO-like interdecadal variability: 1900-93, *J. Climate*, 10, 1004-1020.